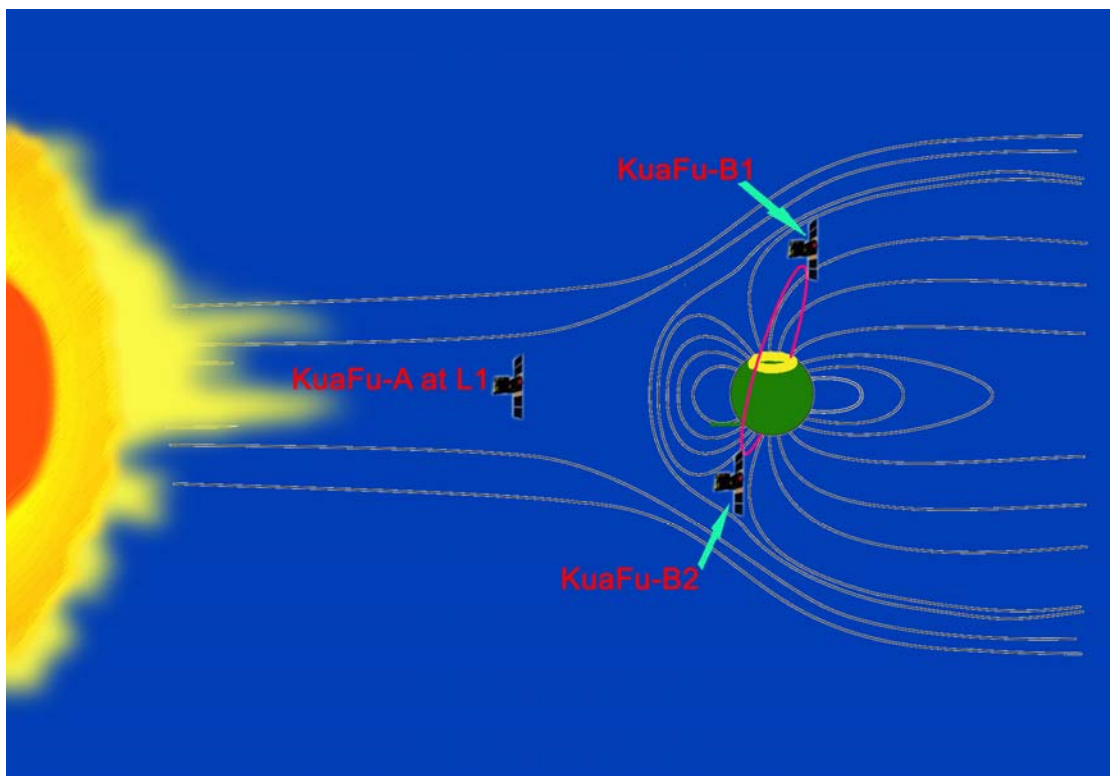


“KuaFu” mission - Space Weather Explorer

Assessment Study Report

Part A: Science Objective and Payload



July 6, 2005

(Updated: Aug. 19, 2005)

FOREWORD

The KuaFu space weather explorer concept was proposed by Chuanyi Tu at the Space Weather Group meeting of the National Natural Science Foundation of China (NSFC) held on January 24, 2003. In October 2004, the KuaFu pre-study project was approved by NSFC as a Key Project. On December 9, 2004, the first international meeting of the KuaFu pre-study team was held in Frankfurt, Germany. At that time, the Canadian Ravens project was merged with KuaFu. The second international meeting of the KuaFu pre-study team and the first international symposium on the KuaFu project were held in Beijing from May 19 to 24, 2005. This assessment report presented here was prepared for submission to the Chinese Space Agency, for approval as a pre-engineering study project and finally as an engineering project for building the proposed satellites and preparing the required launch and ground systems. This report will also be used by KuaFu international team members to solicit the necessary support from their respective funding agencies.

KuaFu assessment pre-study team members

General concept development group

Chuan-Yi Tu	Peking University, China (KuaFu Team Coordinator)
Rainer Schwenn	Max Planck Institute for Solar System Research, Germany (KuaFu-A Team Coordinator)
Eric Donovan	University of Calgary, Canada (KuaFu-B Team Coordinator)
Jing-Song Wang	Peking University, China (KuaFu-B Team Coordinator)
Li-Dong Xia	University of Science and Technology of China (KuaFu-A Team Coordinator)
Yong-Wei Zhang	DFH Satellite Co. LTD, China (Chief Engineer)
Eckart Marsch	Max Planck Institute for Solar System Research, Germany
Zuo Xiao	Peking University, China
Feng-Si Wei	Chinese Academy of Sciences, China

KuaFu-A scientific payload group

Jean-Louis Bougeret	Centre National de la Recherche Scientifique, France
Chris Carr	Imperial College London, United Kingdom
Wei-Qun Gan	Chinese Academy of Sciences, China
Karl-Heinz Glassmeier	Technical University Braunschweig, Germany
Philippe Lamy	Laboratoire d'Astrophysique de Marseille, France
Pierre Rochus	University of Liege, Belgium
Udo Schühle	Max Planck Institute for Solar System Research, Germany
Rainer Schwenn	Max Planck Institute for Solar System Research, Germany
Shi-Jin Wang	Chinese Academy of Sciences, China
Robert Wimmer-Schweingruber	Kiel University, Germany

KuaFu-B scientific payload group

Hong-Fei Chen	Peking University, China
Eric Donovan	University of Calgary, Canada
Malcolm Dunlop	Rutherford Appleton Laboratory, United Kingdom
Andrew Fazakerley	University College London, United Kingdom
Claude Jamar	University of Liege, Belgium
Mark Lester	Leicester University, United Kingdom
Susan McKenna-Lawlor	National University of Ireland, Ireland
Jian Wu	China Research Institute of Radiowave Propagation, China
Tielong Zhang	Austrian Academy of Sciences, Austria

Engineering Group

Shi-Geng Yuan	DFH Satellite Co. Ltd, China
Wei Wang	DFH Satellite Co. Ltd, China
Sheng-Li Liu	DFH Satellite Co. Ltd, China

Contributors

J.-L. Boit	Laboratoire d'Astrophysique de Marseille, France
J. Chang	Chinese Academy of Sciences, China
J.M. Defise	University of Liege, Belgium
S.-Y. Fu	Peking University, China
J.F. Hochedez	Observatoire Royal de Belgique, Belgium
G. Rousset	Laboratoire d'Astrophysique de Marseille, France
T. S. Trondsen	University of Calgary, Canada
Sebastien Vives	Laboratoire d'Astrophysique de Marseille
L. Xie	Peking University, China
H.-G. Yang	Polar Research Institute of China, China
D.-H. Zhang	Peking University, China

Foreword

Table of Contents

1. Executive Summary	6
1.1 KuaFu-A	7
1.2 KuaFu-B	9
2. Scientific Goals	11
2.1. Space weather science objectives	11
2.1.1. Modern hi-tech society demands	11
2.1.2. KuaFu mission: exploring continuously the complete chain of actions/reactions from the solar atmosphere to geo-space	13
2.1.3. Space weather forecasting	15
2.1.4. Space weather alarm (early warning)	16
2.1.5. Space weather real-time report (now-cast)	17
2.2. New solar science objectives	17
2.2.1. New observations and new science	17
2.2.2. The origin, precursor, evolution and propagation of CMEs	20
2.3. New geo-space science objectives	23
2.3.1. New observations and new science	23
2.3.2. Processes of the global mass and energy transfer and global effects of magnetospheric reconnections	28
2.4. References	30
3. Mission objective	37
3.1. Remote sensing observations on KuaFu-A	37
3.1.1. HI Lyman- α observations of the solar disk from KuaFu-A	37
3.1.2. Coronal EUV observations of the solar disk from KuaFu-A	38
3.1.3. HI Lyman- α observations of CME from 1.1 to 2.5 R_{\odot} from KuaFu-A	39
3.1.4. White light observations of CME from 2.5 to 15 R_{\odot} from KuaFu-A	40
3.1.5. CME-shock related radio and plasma wave measurements from KuaFu-A	41
3.1.6. Hard X-ray/Gamma-ray observation from KuaFu-A	42
3.2. In situ observations on KuaFu-A	43
3.2.1. ICME in situ observation	43
3.2.2. Solar energetic particles observation	44
3.3. Global imaging on KuaFu B1+B2	44
3.3.1. Electron and proton aurora continuous imaging	44
3.3.2. Conjugate aurora activity imaging	48
3.3.3. Ring current remote sensing	49
3.4. In situ observations on KuaFu B1+B2	53
3.4.1. Magnetic field observation	54
3.4.2. Energetic particles events observation	54
3.5. Radio science experiments on KuaFu B1+B2	57
3.5.1. Ionosphere disturbance observation	58
3.5.2. Radio Wave Scintillation Measurements	58
3.5.3. Tropospheric Observations from near Perigee	59
3.5.4. High Resolution Orbit Determination	60

4. Scientific Payload	61
4.1. Scientific payload on KuaFu-A.....	61
4.1.1. Extreme/Far UV Disk Imager Package (EDI).....	61
4.1.2. White Light Coronagraph (Ku-Cor).....	68
4.1.3. Lyman- α Coronagraph (Ly-Cor)	74
4.1.4. KuaFu radio and plasma wave instrument (FengBo).....	81
4.1.5. Solar Wind Instruments Package (SWIP)	85
4.1.6. Solar Energetic Particle Sensor (SEPS)	87
4.1.7. Hard X-Ray and Gamma-ray Spectrometer (HXGR).....	91
4.2. Scientific payload on KuaFu-B.....	92
4.2.1. Far Ultraviolet aurora monitoring cameras (UVAMC)	92
4.2.2. Far Ultraviolet Spectro-Imager (FUVSI)	99
4.2.3. Wide Field FUV Auroral Imager (WFAI)	101
4.2.4. Neutral Atom Imager on KuaFu (NAIK)	103
4.2.5. Fluxgate Magnetometer (FGM)	106
4.2.6. Medium Energy Charged Particle Experiment (IES/IPS)	107
4.2.7. High energy charged particle experiment (HECPE)	109
4.2.8. Tri-Band beacon (TBB)	111
5. KuaFu-B Orbits	113
6. Spacecraft initial design.....	118
6.1. KuaFu-A spacecraft	118
6.1.1. KuaFu-A spacecraft design requirements and constraints	118
6.1.2. KuaFu-A spacecraft baseline design	119
6.1.3. KuaFu-A spacecraft propulsion and hydrazine budget	122
6.1.4. KuaFu-A spacecraft major parameters and specifications	123
6.2. KuaFu-B spacecraft	124
6.2.1. KuaFu-B spacecraft design requirements and constraints	124
6.2.2. KuaFu-B spacecraft baseline design	125
6.2.3. KuaFu-B spacecraft major parameters and specifications	126
List of Acronyms	129

1. Executive Summary

KuaFu is an “L1 + Polar” triple satellite project, and an essential element of the ILWS mission lineup. KuaFu is composed of three spacecraft: KuaFu-A will be located at the L1 libration point between Sun and Earth, and be instrumented to continuously observe the solar disk in the chromospheric Lyman-alpha and coronal extreme ultraviolet emission, to register Coronal Mass Ejections (CMEs) in white-light and Lyman-alpha radiation, and to measure *in-situ* radio waves, the local solar wind plasma and magnetic field, solar energetic particles, as well as the hard X-ray and Gamma-ray spectrum. KuaFu-B1 and KuaFu-B2 are a satellite pair in an Earth polar orbit chosen to allow continuous (24 hours per day) observation of the northern hemisphere auroral oval and the ring current, as well as systematic conjugate auroral observations.. KuaFu B will also carry a limited suite of *in situ* instruments including a fluxgate magnetometer and high- and charged particle detectors.

The KuaFu mission may start at the next solar activity maximum (launch by 2012), with an initial mission lifetime of two to three years that would hopefully be extended post-launch. KuaFu data will be used for the scientific study of the phenomena that comprise *space weather*, and for forecasting purposes. The overall mission design, instrument complement, and incorporation of recent technologies will target fundamental new science, advance our understanding of the physical processes underlying space weather, and raise the standard of end-to-end observation of the Sun-Earth system.

The mission objectives of KuaFu in space weather science are aimed to continuously observe the complete chain of disturbances from the solar atmosphere to geo-space. KuaFu will look at important inputs (the Sun) and outputs (the aurora, ring current, Central Plasma Sheet (CPS), and ionosphere) of the Sun-geospace-Earth system in a systematic way.

- Solar source of the disturbances: solar flares, CMEs, energetic particles,
- Transport of disturbances: interplanetary clouds, radio waves, shock waves, solar energetic particles,
- Geo-effectiveness: auroral activities, sub-storms, magnetic storms.

Fig 1.1 summarizes the KuaFu observations of the Sun-to-Earth chain of actions, reactions, and geospace interactions. The top panel gives the scientific instruments on board KuaFu, the middle panel lists the phenomena to be observed by KuaFu, and the bottom panel explains the scientific objectives of KuaFu.

KuaFu will provide an excellent complement to the forthcoming scientific ILWS solar (i.e., SDO, Solar Orbiter, and Sentinels) and geospace (i.e., SWARM, THEMIS, and the RBSPs and ITSPs, and MMS) missions.

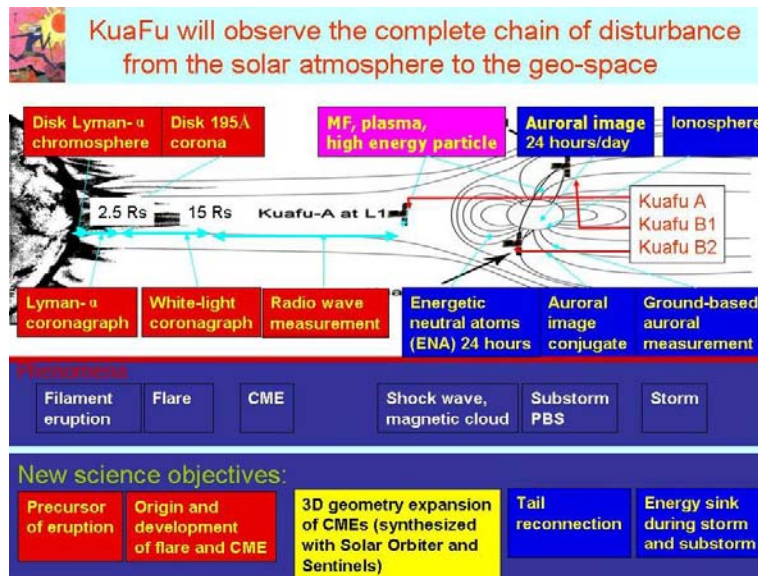


Fig. 1.1 KuaFu will observe the complete chain of disturbance from the solar atmosphere to geo-space

1.1 KuaFu-A

KuaFu-A will be located at the L1 libration point and allow continuous survey of activities on the solar disk and its surroundings as well as *in-situ* observations of the interplanetary medium upstream of the Earth.

KuaFu-A will

- survey for the first time the solar disk with both Lyman-alpha and 19.5 nm EUV imagers to observe the spatio-temporal evolution of activity in the solar chromosphere and corona, such as filament eruptions, optical flares and post eruptive effects;
- survey for the first time disturbances continuously from their origin on the disk to the distant corona, with a Lyman-alpha coronagraph (1.1 to 2.5 R_{\odot}) and a white light coronagraph (out to 15 R_{\odot}), in order to identify the initial sources of CMEs and the acceleration profiles of CMEs;
- observe Type II/III radio bursts caused by accelerated electrons on their way from a flare/CME site out into space, and as far as the Earth's orbit;
- observe *in-situ* the solar wind variability: stream structures, co-rotating interaction regions, Alfvénic fluctuations, shock waves, magnetic clouds, etc.;
- measure the fluxes of solar energetic particles accelerated at flare sites and at shock fronts.

The goals of the KuaFu-A mission, as pointed out above, motivated our choice of instruments for the scientific payload:

- EUV/FUV disk imager (EDI), including a Lyman-alpha disk imager
- Coronal Dynamics Imager (CDI), including a Lyman-alpha coronagraph
- Radio Burst Instrument (RBI)
- Solar Wind Instrument Package (SWIP)
- Solar Energetic Particle Sensor (SEPS)
- Hard X-Ray and Gamma-ray Spectrometer (HXGR)

Table 1.1 Payload Summary of KuaFu-A

Instrument	Mass (kg)	Power (W)	Data rate (kbps)
EDI	25	20	100
CDI	35+20*	35+38*	100
RBI	12	10	4
SWIP	6	6	4
SEPS	8	10	1
HXGR	3	5	1
Total	89+20*	86+38*	210

* Note that the resources of CDI have been estimated assuming two independent instruments. Integrating the 2 coronagraphs in one box and sharing the electronics should result in substantial resources (in particular mass). Note that the integration could be further pursued by merging the coronagraphs and the disk imagers.

KuaFu-A will pursue some new solar science objectives:

- Studies of the mechanisms of how the mass is supplied to CMEs, to the solar wind, and from the chromosphere to the corona?
- Studies the precursors of CMEs, the relation between flares and CMEs, and the mechanisms of CME acceleration and mass loss from the corona;
- Studies of dynamic features in the lower solar atmosphere, such as the network, spicules, cold loops, quiescent and eruptive filaments.

The KuaFu-A spacecraft must be a 3-axis stabilized platform. It should be stationed in a circular orbit around the L1 point. Continuous telemetry is highly desirable. On board data storage and subsequent downloading can also be envisaged, provided a “beacon mode” allows continuous transmission of selected data that are essential for real-time space weather survey.

1.2 KuaFu-B

KuaFu-B will consist of two satellites (B1 & B2) on identical polar elliptical orbits with an inclination of ~ 90 degrees, and relatively phased on that orbit so that when one is at apogee the other is at perigee. KuaFu-B will provide the first-ever continuous global hemispheric auroral imaging, and the only auroral imaging and high-altitude polar in situ observations currently planned for a key period during ILWS.

KuaFu-B will provide

- Systematic observation of the geo-effectiveness (storm/substorm and other consequences) of solar disturbances;
- First-ever 24 hour per day 7 day per week (24×7) global auroral electron (FUV) and proton (Doppler shifted Lyman-alpha) imaging;
- First systematic program of conjugate auroral observations;
- First global auroral imaging program carried out in conjunction with the operation of networks of higher-resolution ground-based imagers in Scandinavia, North America, and Antarctica;
- First-ever 24×7 ENA imaging of the ring current ion population.

With these observational capabilities, KuaFu-B will play an essential role in the overall KuaFu program of geospace science and space-weather exploration. This component of the mission will quantify energy and mass transport in the inner magnetosphere and energy deposition in the ionosphere and thermosphere, thus studying the geospace consequences of the varying solar inputs which will be studied by KuaFu-A. As well, KuaFu-B will address exciting stand-alone science questions related to MI-coupling, mass and energy transport in the CPS and inner magnetosphere, multi-scale processes in geo-space plasmas, and natural complexity.

To accomplish its objectives, KuaFu-B1 and B2 will fly with the following instrument complement:

Table 1.2 Payload Summary of KuaFu-B

Instrument	Mass (kg)	Power (W)	Data rate (bps)
UVAMC	21	11	< 0.5 M
FUVSI	20	4.4	
WFAI	1.5	10	
FGM	3	4.25	3 k
HECPE	3	4	500
IES/IPS	5.6	4.5	5 k
NAIK	4	4	5 k
TBB	3.5	1	TBC

Plasma	TBC	TBC	TBC
Total	~60	~50	~0.5 M

- twin-camera FUV imager for LBL-L and S observations (UVAMC);
- FUV Imaging Spectrograph (FUVSI) for global proton auroral imaging;
- wide field of view FUV imager for nearly global perigee imaging (WFAI);
- ENA imager for ring current observations (NAIK);
- fluxgate magnetometer for *in situ* **B**-field observations (FGM);
- low-energy charged particle experiment (PEACE type, TBC);
- high-energy charged particle experiment (HECPE);
- medium-energy charged particle experiment (IES/IPS);
- tri-band radio beacon (TBB).

The need for global observations in geospace studies has been well established (see Williams, 1990 and 1992, and Donovan et al., 2005, and references therein). KuaFu-B will pursue new geo-space science objectives. Examples include the following:

- exploration of the consequences of solar variability on geospace, leading to understanding of the role of the CPS in supplying mass to the ring current, the mid-latitude IT storm, and other processes;
- new and exciting studies of magnetosphere – ionosphere - thermosphere (MIT) coupling, elucidating the role of reconnection in poleward boundary intensifications (PBIs) and how auroral type (Alfvenic vs static) relates to MI coupling in dynamic geospace processes such as substorms;
- quantitative assessment of the geo-effectiveness of physical processes such as the substorm, reconnection, and boundary-layer dynamics in the flow of energy and mass to and within geospace;
- understanding how important complexity, emergent behavior, and global interactions are in the systems-level behavior of geospace.

2. Scientific Goals

2.1. Space weather science objectives

2.1.1. Modern hi-tech society demands

Space Weather is defined as conditions on the Sun and in the solar wind, magnetosphere, ionosphere and thermosphere that can influence the performance and reliability of space-borne and ground-based technological systems and can endanger human life or health. Our modern hi-tech society is increasingly vulnerable to disturbances from outside our Earth system, in particular to those initiated by eruption events on the Sun. The economic consequences are enormous (see, e.g., Siscoe, 2000). For this and other reasons, space weather and its prediction are receiving significant attention, not only from scientists, but also from the general public (see, for example, “The Sun – Living With The Stormy Star” in National Geographic, July 2004). In the next decades, the International Living With a Star (ILWS) program will stimulate, strengthen, and coordinate space research with the overarching objective of understanding the governing processes of the connected Sun-Earth System as an integrated entity and will stimulate and strengthen the study of the Sun-Earth connected system and the effects which influence life and society on Earth.

For illustration, Table 2.1 is a list of some of the effects of the “Bastille Day” events in July 2000 on several Earth-orbiting satellites. A total of 7 satellites suffered severe impacts, one of which was lost.

Table 2.1 The “Bastille Day” event: its effects on satellites

14-16 July 2000: proton event and geomagnetic storm, $A_p^* = 192$, $\min D_{st} = -300$ nT
➤ ASCA (Advanced Satellite for Cosmology and Astrophysics) – lost attitude fix, resulting in solar array misalignment and power loss; satellite probably lost
➤ GOES-8 & -10 – SEM Electron sensor problems
➤ ACE (Advanced Composition Explorer) – Temporary solar wind and other sensor problems
➤ WIND – Permanent (25%) loss of primary transmitter power and temporary loss of Sun and star sensors
➤ SOHO (also YOHKOH & TRACE) – High energy protons obscure solar imagery
➤ GEO and LEO Satellites – S/C orientation problems during solar proton event
➤ GEO Satellite lost ~0.1 amp output from solar arrays

Figure 2.1 exhibits a clear relation between the solar activity and satellite anomalies. This result may be understood as the satellites are influenced by the space storms mostly happened during the solar maximum years. Figure 2.2 shows the dramatically increasing number of space weather “customers” during the last 60 years

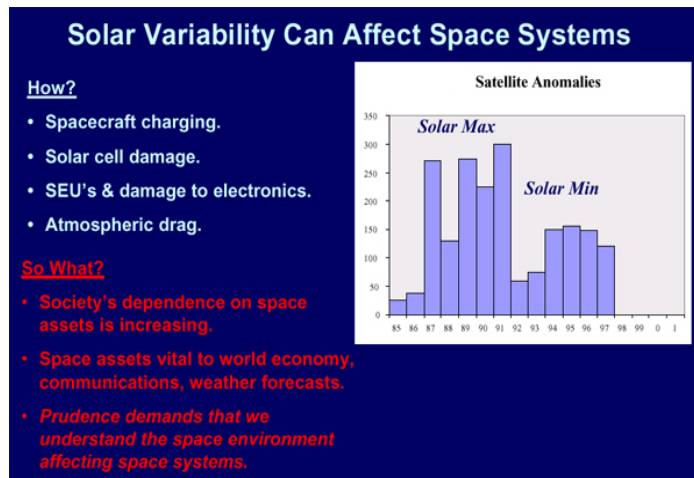


Fig. 2.1 Solar activity and satellite anomalies (from ILWS web site)

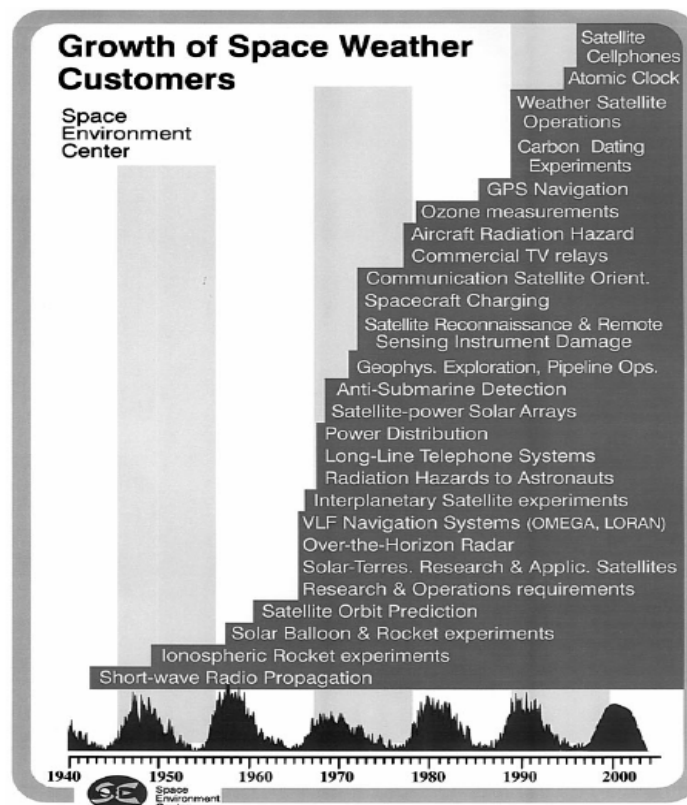


Fig. 2.2 Growth rate of space weather “customers” (according to NASA and NOAA)

This growing demand requires simultaneous, long-term, synoptic observations of the primary sources (i.e. the Sun, solar EUV, the solar wind, etc.), and the sinks (i.e., the ring current, radiation belts, plasmasphere, ionosphere, and thermosphere) inside Earth’s atmosphere in which the energy received from the Sun is deposited. In addition, specific space missions are needed to carry out *in-situ* observations essential for the exploration of the specific physical processes. On the one hand, ILWS targets the understanding of specific physical processes such as magnetic reconnection. On the other, replacing empirical understanding of the coupling processes based on statistical study of long-term-observation data with sound physical understanding will have the natural consequence of increasing our ability to predict space weather phenomena.

At present, the only space weather stations in service are – apart from the GOES-satellites operated by NOAA – primarily scientific missions that turned out to produce excellent data for space weather application purposes: SOHO, ACE, and Wind stationed near the L1 point. Since these spacecraft are now well past their nominal lifetimes, it is of utmost importance for space weather study to provide continuation of such capabilities. At present, during the ILWS timeframe, there is not a single global auroral imaging mission planned. Geospace missions such as SWARM, the ITSPs and RBSPs, ePoP, THEMIS, and others will be carrying out new and exciting in-situ observations aimed at advancing our understanding of how energy makes its way from the Sun through geospace to the Earth; however from a space weather and systems-level science perspective, we will be arguably at our lowest capability in decades for quantifying the source of that energy and the global response of the two crucially important sinks, namely the ionosphere and thermosphere.

2.1.2. KuaFu mission: exploring continuously the complete chain of actions/reactions from the solar atmosphere to geo-space

The proposed “Space Weather Explorer Mission”, here simply called the “KuaFu Mission”, is perfectly suited to meet the present needs of space weather and related science. The name is drawn from an ancient Chinese myth, in which KuaFu was said to insist on running to catch up with the Sun’s movement. The KuaFu mission is an “L1 + Polar” triple satellite project composed of three spacecraft: KuaFu-A, KuaFu-B1 and KuaFu-B2. Fig. 2.3 illustrates the geometric configuration of the three satellites. The KuaFu mission is designed to observe the complete chain of disturbances from the solar atmosphere to geospace, including solar flares, CMEs, interplanetary clouds, shock waves, and their geo-effects, such as magnetospheric substorms and magnetic storms, and auroral activities in general. The KuaFu mission will look at important inputs (the Sun) and outputs (the aurora and ring current) from the Sun-geospace-Earth system in a systematic way. The instruments will also make use of new technologies aimed at facilitating work on new fundamental science targets.

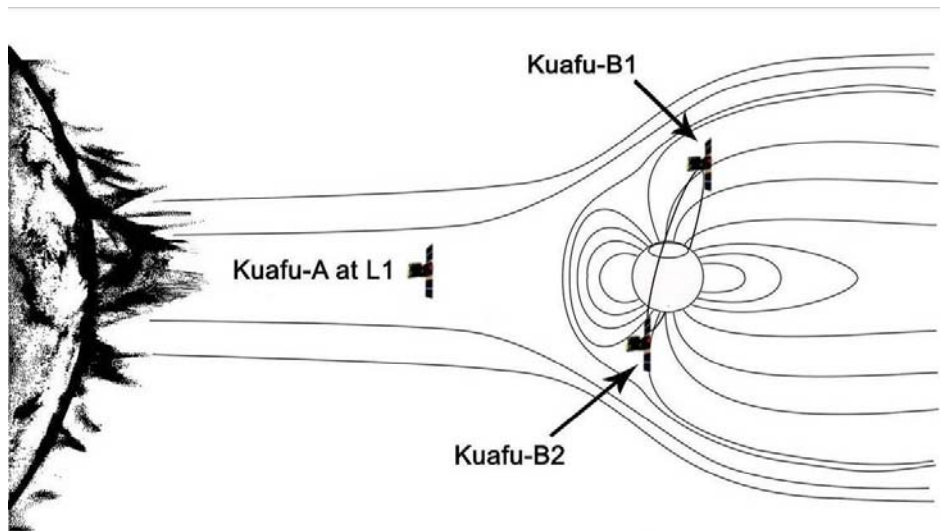


Fig. 2.3: Heuristic illustration of the proposed three spacecraft of the KuaFu mission

KuaFu-A will be located at the L1 point. Its instruments will continuously observe solar EUV emissions and white light CMEs, and measure radio waves, the local plasma and magnetic field properties, as well as solar energetic particle fluxes. KuaFu-B1 and B2 will have polar orbits appropriate for 24 hour per day, seven day per week (“24X7”) observations of the northern polar, auroral, and mid-latitude ionosphere, the ring current, and polar high *altitude in situ* magnetic field and charged particle fluxes.

Fig. 2.4 gives an overview of the kinds of observations KuaFu will make to explore the chain of solar-terrestrial disturbance. The figure shows the source of the Bastille-day storm (the solar flare and CME, interplanetary magnetic cloud, and southward magnetic component and magnetic storm). The right frame shows the resulting aurora activities.

The mission may start at the next solar maximum (launch by 2012) with a nominal lifetime of two to three years. The data obtained by this mission will be used for the scientific study of physical processes at the heart of space weather, and will be used for space weather exploration and forecasting purposes. Most KuaFu instruments will make use of heritage technology and the mission will utilize reliable data transmission.

KuaFu will provide essential space weather services by observing the Sun and the geo-space, and provide integral observations for fundamental science under the ILWS umbrella. Moreover, KuaFu will complement the ILWS program with a unique suite of instruments, specifically selected for the purpose of studying the Sun-Earth connection in ways that no past, existing or planned ILWS missions has. The three KuaFu spacecraft will provide an excellent complement to the forthcoming scientific ILWS solar (i.e., STEREO, SOLAR-B, SDO, Sentinels, Solar Orbiter) and geospace (i.e., SWARM, THEMIS, and the RBSPs and ITSPs) missions.

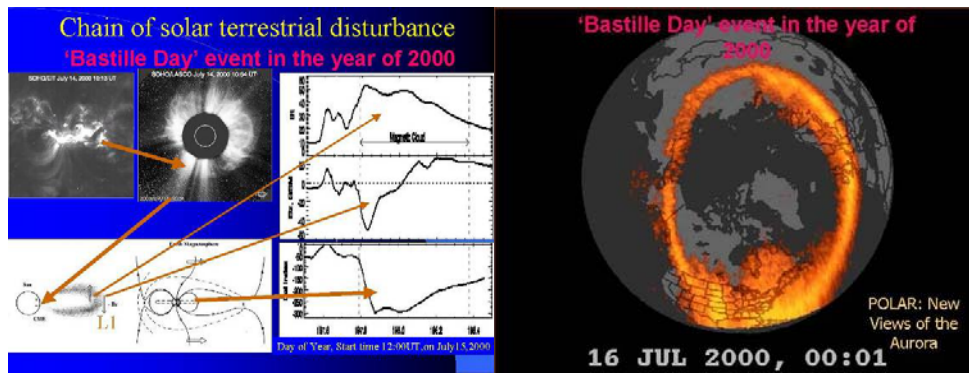


Fig. 2.4 Left: the “Bastille Day” event in the year of 2000 and its geo-effects; Right: An extended auroral oval caused by the event observed by the POLAR satellite

2.1.3. Space weather forecasting

Since space weather phenomena are powered by the Sun, solar observations play a key role for analyzing and forecasting space weather (Webb et al., 2001). The latest generation of space-based instruments has allowed major advances in understanding the processes involved near the Sun, in interplanetary space, and in the near-Earth environment (see Figure 2.4). Unfortunately, the precision in space weather forecasting is still poor. From a practical standpoint, solar energetic transients, i.e., flares and coronal mass ejections (CMEs) occur rather spontaneously, as we have not yet identified unique signatures that would indicate an imminent explosion and its probable onset time, location, and strength. Solar energetic particles, accelerated to near-relativistic energies during major solar storms, arrive at the Earth's orbit within minutes and may, among other things, severely endanger astronauts on the way to Moon or Mars. The underlying physics of many of these processes is not sufficiently understood, and further fundamental research is badly needed.

Even once a notable outbreak has been observed, it is still hard to predict whether the ejected gas clouds will reach the Earth at all, at which time and what their effects will be. It is of crucial importance to determine the direction in which an eruption is originally pointed, since only one out of ten CME events hits the Earth. Space-based coronagraphs keep providing spectacular views of erupting gas clouds but show only their projections on the plane of the sky and cannot be used to infer the CME direction and speed of propagation. CMEs pointed along the Earth-Sun line appear as “halos” around the occulter disk in a coronagraph field of view (Howard et al., 1982). The top left picture on the left column of Fig. 2.4 shows an example of halo-CME. Complementary disk observations are required for deciding whether a halo-CME is pointed towards to or away from the Earth.

The value of such coordinated observations has been demonstrated repeatedly since the set of modern solar telescopes on the Solar and Heliospheric Observatory (SOHO) spacecraft went into operation in early 1996 (Domingo et al., 1995). The disk

images taken by the EUV Imaging Telescope (EIT) at a sufficiently high time cadence allow almost continuous detection of flare explosions and filament eruptions (Delaboudinière et al., 1998). Simultaneously, the instruments of the Large Angle and Spectrometric Coronagraph (LASCO) observe the corona above the solar limb in a range from 1.1 R_{\odot} from Sun center out to 32 R_{\odot} and observe any CME in great detail (Brueckner et al., 1995). Of course, the optimum tool for forecasting the arrival of mass ejecta and magnetic clouds at Earth would be a continuous coronagraphic survey of the whole Sun-Earth line from a distant viewpoint, as is planned for STEREO (<http://STEREO.gsfc.nasa.gov/index.shtml>). However, such ideal constellations can last only a few years (Sheeley et al., 1985). Any long-lasting space weather surveillance mission should be stationed at the L1 Lagrange point around 1.5 million kilometers upstream of the Earth, like SOHO and ACE. Recently it was shown on the basis of LASCO data that even with CME observations made on the Sun-Earth line proxy data can be derived that allow us to infer the propagation time to 1 AU with reasonable reliability (Schwenn et al., 2001, 2005). That is encouraging for the operational space weather relevance of KuaFu with its L1 location, planned set of coronagraphic and disk observing instruments, and modern radio wave detector with which it is possible to trace ejected clouds during their travel from Sun to Earth (Reiner et al., 1998).

2.1.4. Space weather alarm (early warning)

A second objective of the KuaFu-A spacecraft located at the L1 point is to sample the properties of the solar wind well before it hits the Earth's magnetosphere. The geo-effectiveness of a disturbance in the solar wind depends crucially on plasma density and speed and particularly on the orientation of the interplanetary magnetic field (IMF). Particularly when the IMF has a strong southward component (i.e., opposite to the Earth's field at the magnetopause subsolar point) magnetic reconnection will occur leading to enhanced energy input into geospace and (other conditions permitting) eventually trigger a major geomagnetic storm with all its consequences (see, e.g., Tsurutani and Gonzalez, 1997). The most dramatic southward swings of the IMF occur usually in the compressed plasma that is piled up by interplanetary shock waves launched by major CMEs, and in the so-called “magnetic clouds” often imbedded in the ejecta (Burlaga et al., 1981, Wei et al., 2003). From arrival at L1 to the onset of a geomagnetic storm there is usually a time delay of one to several hours. Thus, an early warning from KuaFu-A may allow taking precautionary measures. After all, the payload of KuaFu-A must contain a complete set of particle and field instruments that deliver their data to the Earth continuously and in real time. This set must also include instruments for detecting solar energetic particles.

The data to be collected by KuaFu-A will serve as continuous input to computer models which are used for forecasting the resulting phenomena in the magnetosphere-ionosphere system, in the atmosphere, and at the Earth's surface (Linker et al., 2003). However, in practice such calculations, taking into account all relevant physical processes, are still much slower than the processes themselves, and thus are not

suitable for forecasting purposes. Therefore, an important ingredient for the success of the KuaFu-A mission will be the development of new computer techniques that may, e.g., utilize artificial intelligence, neural networks, and grid computation.

2.1.5. Space weather real-time report (now-cast)

At the other end of the Sun-to-Earth chain, KuaFu-B data would have a profound impact on our ability to “nowcast” space weather, and on our ability to test the robustness of global circulation and electrodynamic models by providing end-end quantitative observations of the sequence of physical events that comprise magnetic storms.

Along this line, KuaFu-B optical data would be used for data assimilation into empirical (e.g., AMIE) and physical (e.g., BATS-R-US) global models (see eg., Winglee et al., 2002; Song, 1999). The objective of the former would be to provide global conductance which, together with convection measurements from SuperDARN and global magnetometer networks, allow for a global specification of the field-aligned currents (Sofko et al., 1995; Sofko, personal communication, 2005). The objective of the latter is to provide a boundary condition to better increase the accuracy of model output (see also Kabin et. al., 2004).

Finally, KuaFu-B integrated imaging provides a natural way to test our modeling capabilities in geospace science. Global models now being modified to include inner magnetospheric physics (ring current, RB, and Region II physics), pressure balance, and more, but cannot really be verified against long time series of global observations in the truest sense (see eg., De Zeeuw et al., 2004). KuaFu-B now provides this possibility. We can assess how well these models do in reproducing the important longer-duration space weather events such as storms.

The source/sink exploration by KuaFu enables quantitative assessment of geo-effectiveness that is otherwise impossible. Thus KuaFu (A and B) will advance our understanding of the physics of space weather, and hence advance our understanding of what is necessary to and possible in terms of prediction.

2.2. New solar science objectives

2.2.1. New observations and new science

KuaFu-A serves two basic purposes: the continuous surveillance of the Sun and heliosphere, and the support of fundamental research in order to better understand the solar processes and basic space-plasma physics underlying space weather. The novel instruments on KuaFu-A provide the appropriate measurements.

The scientific payload on KuaFu-A at L1 includes

- EUV/FUV disk imager (EDI), including a Lyman- α disk imager
- Coronal Dynamics Imager (CDI), including a Lyman- α coronagraph
- Radio Burst Instrument (RBI)
- Solar Wind Instrument Package (SWIP)
- Solar Energetic Particle Sensor (SEPS)
- Hard X-Ray and Gamma-ray Spectrometer (HXGR)

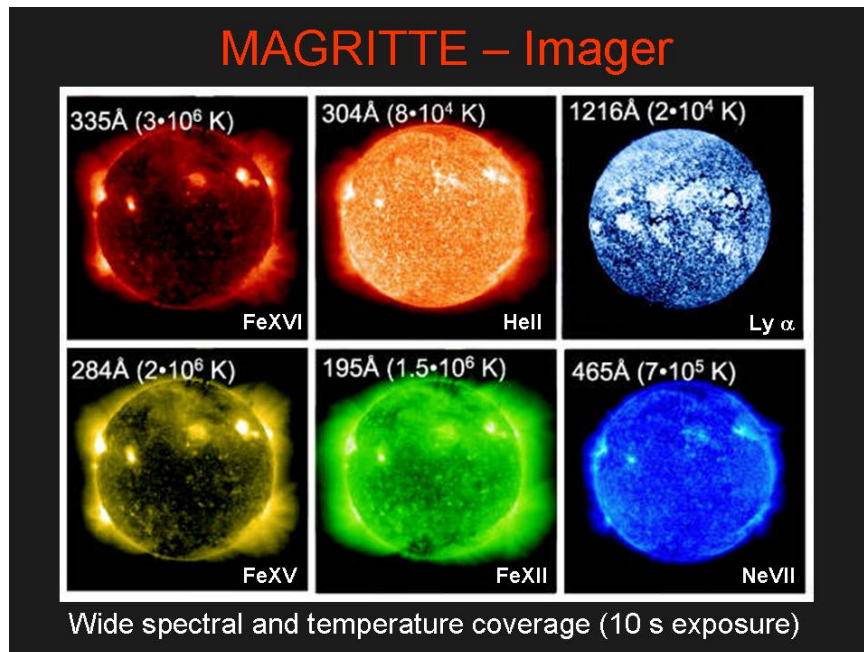


Fig. 2.5 The MAGRITTE-imager shows the solar disk image in Lyman- α , which can be used to track processes in the lowest part of the solar atmosphere

The new observations of KuaFu-A are long time-period Lyman- α disk imaging and lower corona imaging. Figure 2.5 shows images of the solar disk from various emission lines, representing plasmas at different formation temperatures. KuaFu-A will have an imager in 19.5 nm and 121.6 nm. The image at 19.5 nm represents the corona at 1.5 million degrees, while the image with the Lyman-alpha line describes plasma with very low temperature (2×10^4 K).

The instruments on KuaFu-A will allow for the first time to perform

- continuous imaging of the source regions of solar eruptive events in both FUV and EUV lines,
- studies of dynamic features in the lower solar atmosphere, such as the network, spicules, cold loops, quiescent and eruptive filaments.

The related new science may be described as the following three aspects:

(1) Chromospheric evaporation (ablation) driven by flares

The Lyman- α imager (EDI) on KuaFu-A will perform studies of the physical mechanisms of mass supply to flaring loops. There are a lot of interesting questions that EDI might answer:

- Are there observational signatures for thermal conduction fronts driving upflows?
- Is impulsive heating a tracer for reconnection in flares?
- How important is chromospheric condensation for coronal mass loss?
- What do dynamic radio spectra reveal about chromospheric/coronal evaporation?
- Which role do flaring loops play for the transient slow solar wind?
- What are the mechanisms of flare-induced heating of the chromosphere and transition region?

(2) Explosive events, jets, spicules, macrospicules

The Lyman- α imager (EDI) on KuaFu-A will allow us to study the characteristics of EUV spicules. There are still a lot of unanswered questions:

- Are macro-spicules just giant spicules or something different?
- Are spicules in different regions (CH, QS, AR) all alike?
- Are they produced by waves forming shocks or by magnetic reconnection?
- Are they connected with explosive events (bi-directional jets) or blinkers?
- What is the link between spicules and the origin of the solar wind?
- What are the mechanisms of mass supply to the corona?

(3) Fast and slow solar wind, sporadic eruptions, CMEs

The EDI and CDI instruments on KuaFu-A will permit us to study the characteristics of eruptive prominences (EPs) and CMEs. There are still a lot of unanswered questions:

- What are the links between emerging magnetic flux, EPs and CMEs?
- What is the geometry of a CME? (synergy between Solar Orbiter and KuaFu)
- What forces accelerate CMEs (thermal versus magnetic pressure/stress)?
- What are the solar magnetic preconditions indicative for a CME?
- Can one, only from solar observations, predict the geo-effectiveness of a CME?
- What are the mechanisms of eruptive mass loss from the corona?

Continuous imaging of the source regions of solar eruptive events in Lyman-alpha and 19.5 nm line will help answering the following basic questions:

- How is the mass supplied from the chromosphere to the corona?
- How is the mass supplied to the solar wind?
- How is the mass supplied to CMEs?

2.2.2. The origin, precursor, evolution and propagation of CMEs

Space weather forecasting is still in its infancy. It crucially relies on predicting fast and transient plasma processes in the solar atmosphere, which as their consequences affect the Earth's environment and the entire heliosphere. The Sun is a magnetically active and highly dynamic star. We have to admit that predicting even the most dramatic energetic solar transients such as flares and coronal mass ejections is still beyond our capabilities. Several possible precursors of CMEs have reported: flare, filament eruption, blast wave, and coronal dimming (see Fig. 2.6). A new general science task, but a particularly relevant one for KuaFu-A, is to identify on the Sun the unique signatures indicating eruptive magnetic activity and associated outbursts of radiation and particles, and moreover to determine most precisely the onset time, location, and strength of such activity.

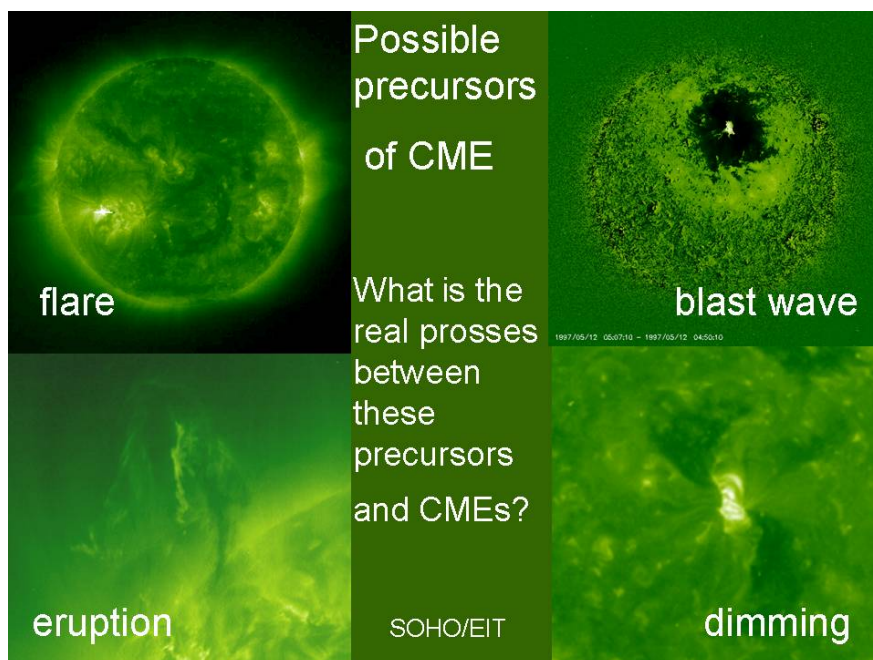


Fig. 2.6 Possible precursors of a CME on the solar disk

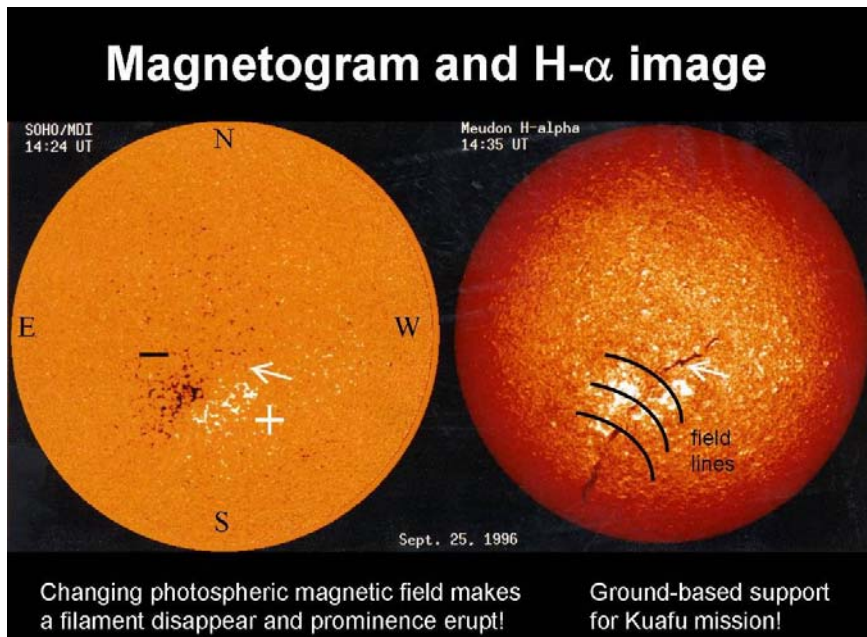


Fig. 2.7 Ground-based H- α observations can be used to support the KuaFu mission

This applies especially to CMEs which were recently shown by Tripathi et al. (2004) to be closely related with bi-polar active regions (AR), concerning, e.g., their intrinsic magnetic helicity, source location on the Sun, and frequency distribution over the solar cycle. Fig. 2.7 shows a chromospheric filament on a bi-polar active region. The basic ultraviolet radiation characteristics of eruptive arcades should be carefully observed, as they can be used as tracers of the plasma dynamics in the CME source regions. To recognize exploding ARs, or prominences that are prone to instability, and subsequently the post-eruptive arcades is an important new objective for KuaFu-A. Since quiescent prominences are comparatively dense and cool magnetic structures, they prominently radiate in vacuum ultraviolet (VUV) lines, like the conspicuous Lyman-alpha emission line of hydrogen at 121.6 nm, but have in this line never been routinely imaged from space at high spatial (one arcsec, or below) and temporal (1-10 s) resolution. Measuring directly the upward speed of possible eruptive prominences through the Doppler-effect requires spectroscopic capabilities. Of course, these statements equally apply to ARs. The three-dimensional configurations of CMEs in the corona and heliosphere were shown by Cremades and Bothmer (2004) to be direct consequences of the dynamic nature of the magnetized solar atmosphere. Structured CMEs appear to arise in a self-similar manner from AR loops systems overlying regions of opposite magnetic polarity, and their topology (and thus white-light appearance) largely depends on the heliographic location, inclination and extent of their source regions on the Sun.

In order to provide better insight into these complex phenomena, KuaFu-A will be equipped with a multi-task EUV instrument (EDI) that allows taking images at high

cadence at the bright Lyman- α line for plasma diagnostics purposes as well as spectral radiance measurements of the source regions of CMEs and other locations of solar magnetic activity. Ground-based magnetogram measurements are needed.

Continuous tracking CMEs from their disk source out to $15 R_{\odot}$ (using the Lyman- α disk imager up to $1.1 R_{\odot}$, the Lyman-alpha coronagraph from 1.1 to $2.5 R_{\odot}$, and the white light coronagraph from 2.5 to $15 R_{\odot}$, will help us to answer the following basic questions:

- What are the precursors of CMEs?
- What is the relation between flares and CMEs?
- How are the CMEs accelerated?
- How is the mass lost from the corona?

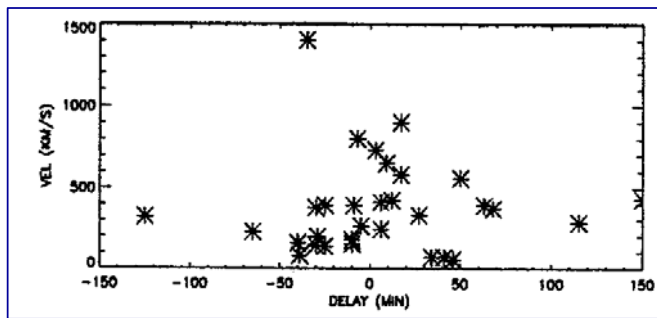


Fig. 2.8 The time separation between flares and correlated CMEs

Fig. 2.8 shows the time separation between flares and correlated CMEs. One sees that there is no unique law for the time separation. Since no continuous observation is made from the flare to the CME one can not understand the underlying physical processes, which control the time separation. KuaFu will solve this problem.

Fig. 2.9 shows the evolution of a balloon type CME. One can track this event only from outside $1.1 R_{\odot}$. It is hard to tell when this event really started. KuaFu may track CME events from its origin on the disk to $15 R_{\odot}$. The data may be used to clarify the relation between the flares and CMEs and answer the question how the CMEs are accelerated.

In combination, the complementary instruments of KuaFu, Solar Orbiter and Sentinels will offer unique perspectives and new vantage points for global solar and heliospheric research. Specifically, these missions will together enable us to study the three-dimensional evolution and morphology of CMEs in an unprecedented way. The Solar Orbiter mission (Marsch et al., 2002) with a launch planned in 2013 and the Sentinels mission presently being planned by NASA for launch in about the same time frame. Solar Orbiter will, while being in a close orbit around the Sun on the far side and eastern and western sides of the Sun, and even outside of the ecliptic plane, together with KuaFu-A allow us to do novel, simultaneous multi-point observations of the solar

disk and off-limb corona.

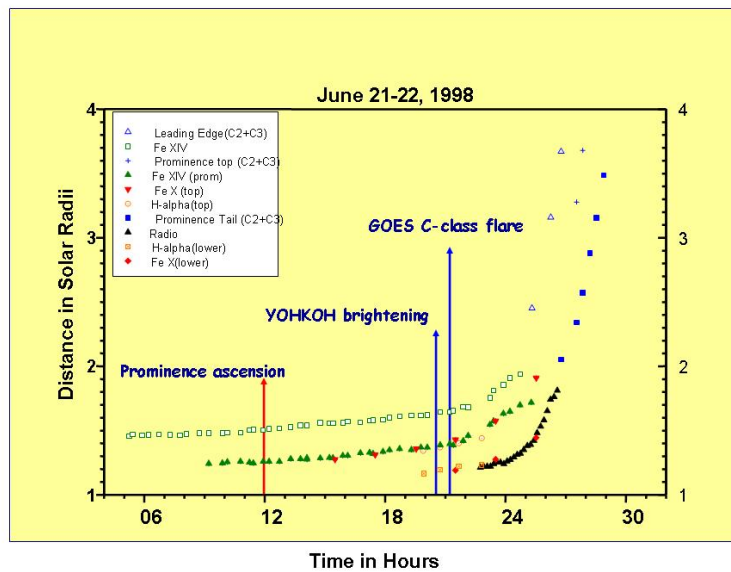


Fig. 2.9 The initiation of a balloon type CME

2.3. New geo-space science objectives

2.3.1. New observations and new science

The KuaFu-B is a satellite pair (KuaFu B1 & B2) would be launched into identical elliptical orbits with apogees initially over the northern polar region. The satellites would be co-rotating and relatively-phased along those orbits so that when one is at apogee the other is at perigee. This orbital arrangement provides the possibility of continuous global aurora and ring current imaging, and an excellent platform for high-latitude and high-altitude *in situ* observations. KuaFu-B will quantify how energy derived from the solar wind powers the magnetospheric and ionospheric current systems and convection, leading to the aurora, enhanced ionization, and Joule heating. KuaFu-B thus completes the KuaFu mission objective of studying the geospace response to varying solar inputs.

At the time of its proposed launch (by 2012), KuaFu-B1 & B2 would be the only geospace satellites on high altitude geospace orbits. System level science in the spirit of ILWS will not be possible without simultaneous observations in all key geospace regions (ref. Fig. 2.10). Thus, KuaFu-B provides an exciting opportunity to fly *in situ* instruments that will greatly increase the scientific payoff of the mission, and make true system level science a reality.

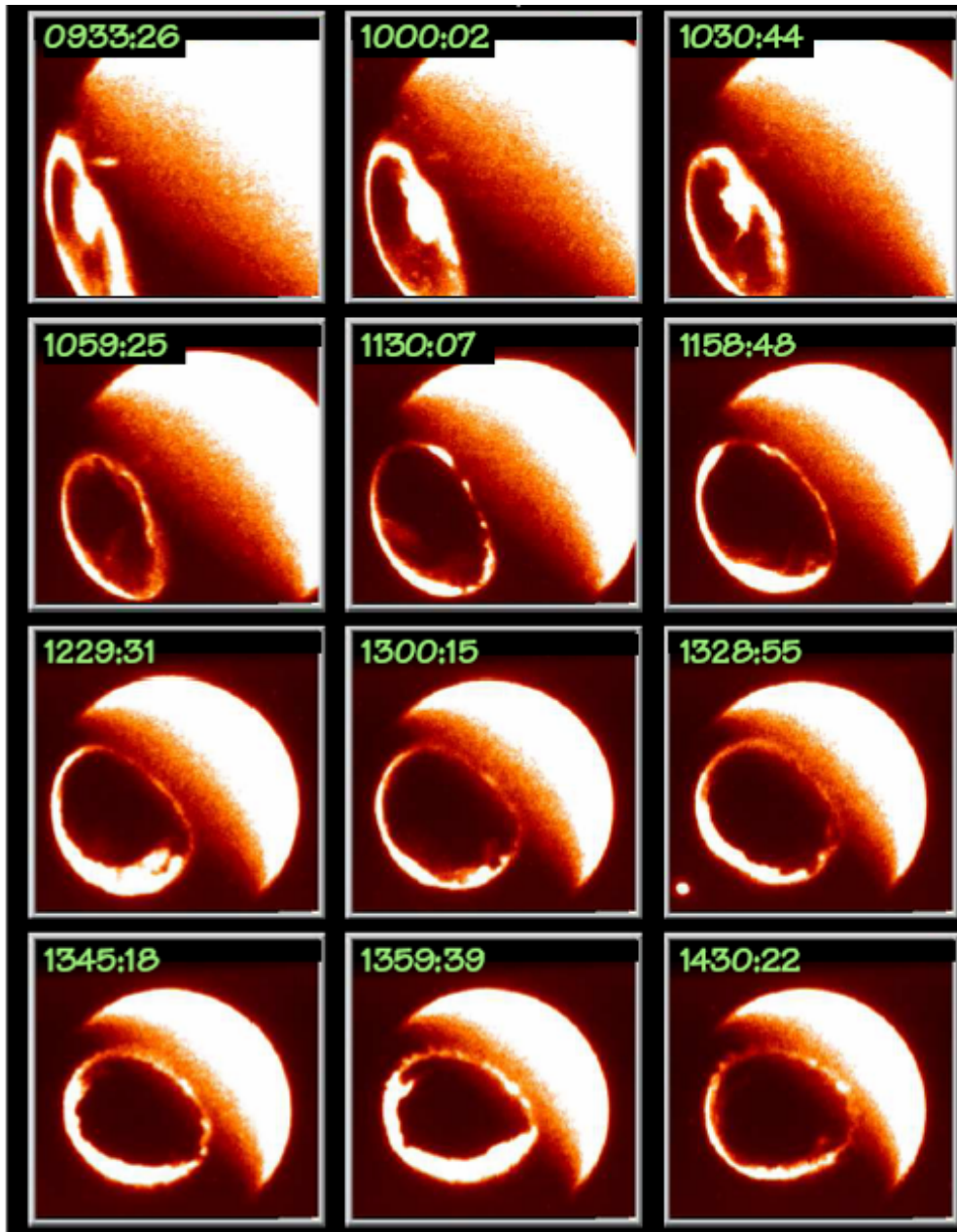


Fig. 2.10: IMAGE/FUV WIC images of the global FUV auroral distribution from a particularly active night. Note the unusually large cusp features in the first three images, the activity at the poleward border throughout, and the giant undulations that appear later on the equatorward edge of the post noon oval. UVAMC on KuaFu will follow such dynamic geospace processes in the global electron and proton aurora, and the ring current via ENA imaging from NAIK. Figure courtesy of Mike Henderson.

The observations of KuaFu-B will fall into three categories:

(1) Global remote sensing of the auroral distribution and ring currents. It is the primary drivers of the orbits and technical specifications of the satellites:

- Far ultraviolet aurora cameras for LBH-long and short bands;
- Far ultraviolet spectro-imager for proton aurora;
- Wide field of view FUV aurora imager for perigee aurora;
- Energetic Neutral Atom imager.

(2) Opportunistic *in situ* observations of key field and plasma properties:

- Fluxgate magnetometer;
- Simultaneous in- and outboard radiation environment observations;
- Energetic electron and proton imagers.

(3) Radio science experiments to support space-weather relevant ionospheric and tropospheric studies:

- Radio beacon for ionosphere and troposphere observation.

With these observations, KuaFu-B will realize the

- (1) first ever 24×7 global auroral and ENA imaging;
- (2) first systematic conjugate imaging experiment;
- (3) first simultaneous imaging across all relevant spatial scales (global to 10 km from the satellites and >10 km to <100 m from the complementary ground observations;
- (4) best out-of-band rejection yet achieved in LBH band.

The KuaFu-B observations that would facilitate such new exciting science are, in order, as follows:

- (1) long duration quantitative observations of the auroral electron and proton distribution as well as the ring current will span complete magnetic storms and other geospace processes. This will facilitate exploration of the response of geospace to varying solar and solar wind inputs, bringing closure to such questions as the role of the substorm in the storm, the role of the CPS in providing matter to the ring current, and elucidating geospace energy pathways that lead to, for example the mid-latitude IT storms;
- (2) systematic conjugate imaging and quantitative observations of auroral electron characteristic energy and energy flux will support new and exciting studies of magnetosphere – ionosphere - thermosphere (MIT) coupling. For example, conjugate electron auroral observations of Pole-ward Boundary Intensifications (PBIs) will determine whether PBIs are a direct consequence of reconnection or some lower altitude process. For another, global time evolving maps of energy and

energy flux of precipitating electrons will allow us to determine how auroral type (Alfvenic vs static) relates to MI coupling in dynamic geospace processes such as substorms.

- (3) With our observations of the auroral electron and proton energy flux during storms and simultaneous solar and solar wind observations from KuaFu-A we will be able to quantitatively assess the geo-effectiveness of geospace processes. Without KuaFu’s source/sink approach this would not be possible. Taken together with direct *in situ* observations of processes in the geospace system by missions such as THEMIS (2007-) and MMS (2011-), KuaFu A & B observations will allow us to determine the relative importance of physical processes such as the substorm, reconnection, and boundary-layer dynamics in the flow of energy and mass to and within geospace;. The integrated and continuous remote sensing observations of the aurora and ring current from KuaFu-B, the solar and solar wind observations from KuaFu-A, and data from other *in situ* missions will allow us to test geospace modeling capabilities and will motivate physics-based improvements of global models;
- (4) It is quickly becoming apparent in space physics that in order to understand the behavior of the complex coupled system we refer to as geospace, we need to take both a system-level approach, and to explore the implications of natural complexity in geospace science. Clearly, global interactions are important at the systems-level. As well, geospace dynamics, such as substorms, may well be examples of what complexity theorists call emergent behavior. KuaFu-B will, in combination with ground-based instruments, provide a quantum leap forward in our ability to simultaneously observe across all relevant space and time scales, and to explore geospace with complexity, interaction, and systems-level science

The natural synergy of KuaFu B with other missions would be powerful. KuaFu-B imaging would complement all ground-based and equatorial satellite programs (see Figure 2.11-12). For example, together with THEMIS in its upstream capability or SWISE, KuaFu-B could directly address questions such as “are all substorms triggered?” KuaFu-B would enhance the role of European and Asian ground-based magnetometry and other observations in missions such as THEMIS and the RBSPs. Global optical observations from KuaFu-B, taken together with global convection measurements from SuperDARN/PolarDARN, would allow us to infer conductivities and electric fields, and the global distribution of field-aligned currents [see Figure 2.12]. KuaFu-B imaging would provide global optical observations that would provide context for incoherent scatter radar measurements from Svalbard, Tromso, Resolute Bay, Millstone Hill, and Poker Flat [see Figure 2.12]. KuaFu-B will provide context for and new science based on coordination with essentially every component of the ILWS program, including programs which are of strategic importance to China (such as SuperDARN, MERIDIAN, and EISCAT).

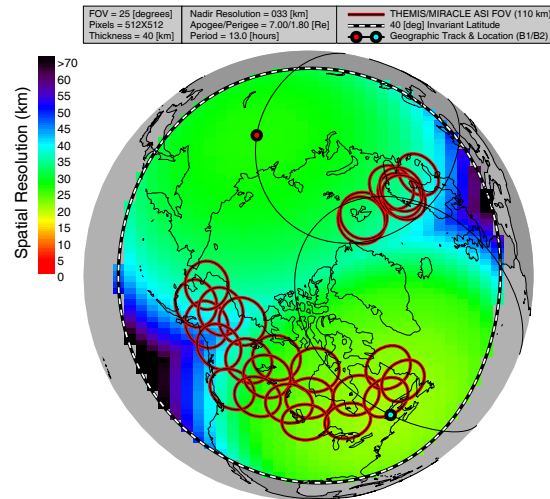


Fig 2.11: The spatial resolution for locations poleward of 40 degrees invariant latitude afforded by the FUV electron auroral imagers on the two KuaFu-B satellites. Note the ground-tracks and ground locations of the KuaFu-B satellites. This is for one time during the orbit; however such global scale spatial resolution would be sustained for over 2 years. Also plotted for comparison are the fields of view of the current MIRACLE array and the planned (and funded) THEMIS array.

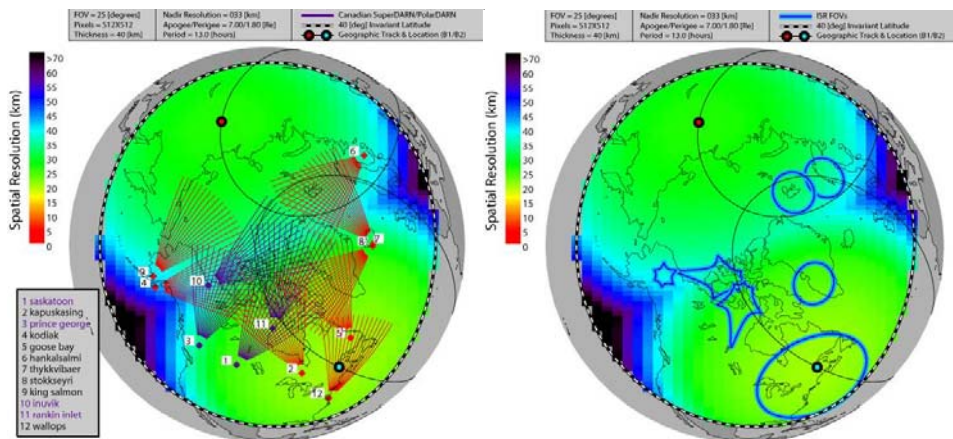


Fig 2.12: KuaFu B imaging would also complement all ground-based programs. Left: KuaFu-B optical data would provide an important complement for global convection maps from the SuperDARN HF-radar array. The spatial resolution of the global images would be comparable to or better than the spatial resolution of SuperDARN convection measurements under normal operating modes (two planned PolarDARN radars (10 and 11) would fill in the gap in coverage over the polar cap that has plagued SuperDARN to date); Right: KuaFu-B optical data would provide important context for measurements from incoherent scatter radars (ISRs) in the north polar region.

2.3.2. Processes of the global mass and energy transfer and global effects of magnetospheric reconnections

The scientific objectives that drive the requirements and subsequent instrument payloads are all related to mass and energy transport in the magnetosphere, energy deposition in the ionosphere-thermosphere (IT) system on global scales, and the origin of structure in geospace plasmas. KuaFu-A and -B are strategically placed and instrumented to provide observations bracketing the geospace system, thus quantifying energy sources and their effects on various geospace sinks, such as the IT-system, ring current, plasmasphere, and ion and electron CPS. All of these complementary ILWS missions are either equatorial magnetospheric probes (MMS, THEMIS, RBSPs, ORBITALS, etc), or are top-side ionospheric probes such as SWARM.

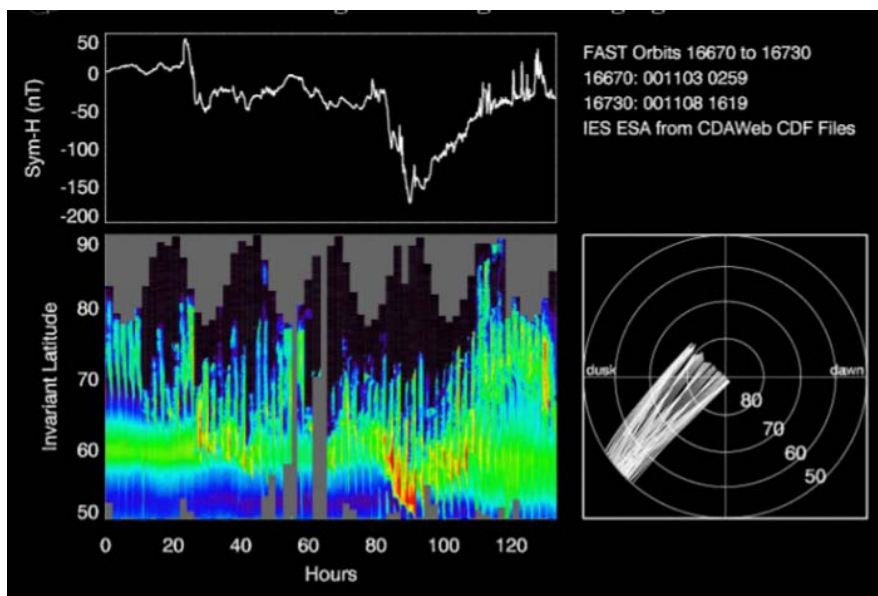


Fig 2.13: 14 days of *in situ* ion data from the FAST ESA ion instrument (see lower left panel) FAST ion ESA energy spectra for 130 hours bracketing two geomagnetic storms (see Sym-H top left). The data is from successive passes of the evening sector auroral oval (see footpoints bottom right). The lower left panel shows successive electron spectra for evening sector orbits that span an active period during which there are several large geomagnetic storms. During these events, the equatorward boundary of the ion CPS undergoes significant movement in latitude. More important, that motion carries the ion plasma sheet deep into the inner magnetosphere, across the outer radiation belts. Studying the two-dimensional spatio-temporal evolution of the ion and electron CPS is a primary technical objective of KuaFu.

The interactions between the ion and electron CPS, the ring current, and the ionosphere/thermosphere in storms and substorms are only understood in part. This is

an overarching theme in geospace that encompasses many problems and commands significant attention from researchers around the world. The fact that advances in quantitative and physical understanding of these interactions are central and relevant themes in space physics is demonstrated by, for example, the topics of various recent and ongoing “GEM Campaigns” which include “Inner Magnetosphere and Storms”, “Global Interactions”, and “Magnetosphere-Ionosphere Coupling” (see the GEM website at <http://www-ssc.igpp.ucla.edu/gem/Welcome.html>). Specific examples of related problems include: How important is precipitation in the thermospheric energy budget? How important is precipitation and Joule heating in modifying the mid-latitude ionosphere? What is the role of substorms in storms? How does the CPS feed plasma into the ring current? Are sawtooth events substorms? There are many more. Moreover, these interactions take place over days or even weeks, and “system level” understanding of geospace phenomena, which is the overarching objective of the ILWS geospace program, will never be possible without global end-end observations that span long-duration geospace phenomena such as magnetic storms. KuaFu-B will provide a set of integrated auroral (electron and proton) and ring current observations that span long duration geophysical events.

Due to the nature of the source of diffuse aurora, we assume its inter-hemispheric conjugacy, but it certainly has not been established (see eg., Ashour-Abdalla and Thorne, 1978). We do not understand how conductivity affects MI coupling. By examining, for example, the consequences of differential conductivity at opposite ends of flux tubes one could assess the role of conductivity in some dynamic processes such as expansive phase onset (see eg., Sato et al., 1998). How does reconnection occur during northward IMF? By examining F-region patches in both polar caps simultaneously one could assess this important question. As well, reconnection at the distant neutral line may be the ultimate source of poleward boundary intensifications (de la Beaujardier, 1991; Lam, M., 2005). Evidence of conjugacy of PBIs would shed light on the possible role of reconnection in CPS dynamics. In fact, our collective understanding of conjugate discrete auroral phenomena are based on such limited data that any systematic observational program aimed at conjugacy would undoubtedly lead to new discoveries as well as answering the above questions. KuaFu-B will provide the first-ever systematic conjugate auroral imaging. Although the conjugate imaging will only be available for ~40 minute periods during every orbit half-period (ie., twice per orbit), this will still provide numerous conjugate observations of substorm onset, storm sudden commencement, and snapshots through all phases of the magnetic storm.

The aurora exhibits spatial structure on scales ranging from global down to tens of meters or less (Maggs and Davis, 1968), and temporal scales ranging from sub-second flicker (see Kunitake and Oguti, 1984) to multi-day storms. Some of these responses are a direct manifestation of changes in the solar wind driver (i.e., sudden impulses – see Zhou and Tsuritani, 2001), large-scale instabilities in the magnetosphere (i.e., substorms), and physical processes that are local to the lower altitudes such as the Alfvén resonator (see eg., Lysak, 1991). Energy is extracted from the solar wind, drives global convection and the magnetospheric current system, and ultimately leads to a

cascade of energy down to smaller and smaller spatial scales. We now understand that there are repeatable structures in the magnetospheric plasma, an excellent example of which is the mesoscale arc (Knudsen et al., 2001). We do not have a clear picture as to how this structure arises, nor do we understand how it influences, for example, MI-coupling (this question is raised repeatedly in the literature including in Semeter and Doe, 2002). Furthermore, the geospace system is a readily accessible environment in which structure arises naturally and repeatedly, most likely as a consequence of “interactions” as the term is used in the emerging field of natural complexity. Thus, multi-scale processes in geospace provide us with the opportunity to explore complexity in nature, something that is growingly recognized as of fundamental importance across many scientific disciplines (see the webpage for the British Antarctic Survey “Natural Complexity” project at http://www.antarctica.ac.uk/BAS_Science/programmes2005-2010/natural_complexity as well as recent work involving the aurora such as that by Uritsky et al., 2002) KuaFu-B will provide global observations of the electron aurora with spatial resolution on the order of 30 km. While this is better than has been previously obtained, it does not allow for simultaneous observations across all relevant spatial scales. However, KuaFu-B will operate simultaneously with mesoscale arrays of All-Sky Imagers and, on occasion, with telescopic imagers with very high spatial resolution. The combined capabilities will provide overlapping views ranging from global scales down to tens of meters.

Dynamic magnetospheric processes such as substorms, sporadic reconnection, and sudden impulses create dramatic changes in the auroral distribution on local and global scales. We do not presently know, however, if there is any signature of mid-tail reconnection in substorms, how the nature of the discrete aurora changes in the substorm expansive and recovery phases (i.e., Alfvénic versus electrostatic/inverted V), or whether transient brightening of the aurora near the polar cap boundary signify transient reconnection at the distant neutral line. In practice, inverted-V aurora are powered by large-scale convection and the Alfvénic aurora are thought to be a response to field-line reconfiguration. As well, the precipitating electrons in inverted-V aurora are usually more energetic (above 1keV) than those involved in Alfvénic aurora (typically 1keV or less). KuaFu-B will provide the first-ever global time-evolving maps of the characteristic energy and energy flux of the electron aurora, global time-evolving maps of the proton aurora, and the first systematic conjugate auroral imaging. KuaFu-B will provide a data set ideally tailored to explore how auroral acceleration mechanism relates to and even feeds back to magnetospheric dynamics.

2.4. References

1. Alexeev I.I., Energy flux in the Earth's magnetosphere: Storm – Substorm relationship, Space Sci. Rev., 107 (1-2), 141-148, 2003.
2. Ashour-Abdalla, M., and R. Thorne, Toward a unified view of diffuse auroral

- precipitation, *J. Geophys. Res.*, 83, 4755, 1978.
3. Brandt, P. C., Ohtani, S., Mitchell, D.G., Fok, M.C., Roelof, E.C. and Demajistre, R., Global ENA observations of the storm mainphase ring current: implications for skewed electric fields in the inner magnetosphere, *Geophys. Res. Lett.*, 03-18, 2002.
 4. Brandt, P.C., Goldstein, J., Anderson, B.J. and Immel, T.J., Global dynamics of MI-coupling in the inner magnetosphere: Relation between the ring current field-aligned currents, auroral conductance and electric field, www.cosis.net/Abstracts/. IAGA2005-A-01284 2005
 5. Brueckner, G.E., Howard, R.A., Koomen, M.J., Korendyke, C.M., Michels, D.J., Moses, J.D., Socker, D.G., Dere, K.P., Lamy, P.L., Llebaria, A., Bout, M.V., Schwenn, R., Simnett, G.M., Bedford, D.K., and Eyles, C.J.: The large angle and spectroscopic coronagraph (LASCO), *Solar Phys.*, 162, 357-402, 1995.
 6. Burlaga, L.F., Sittler, E., Mariani, F., and Schwenn, R., Magnetic loop behind an interplanetary shock: Voyager, Helios, and IMP 8 observations, *J. Geophys. Res.*, 86, 6673-6684, 1981.
 7. Cremades, H., and Bothmer, V., On the three-dimensional configuration of coronal mass ejections, *Astron. Astrophys.*, 422, 307-322, 2004.
 8. de la Beujardier, Sondrestrom radar measurements of the reconnection electric field, *J. Geophys. Res.*, 96(A8), 13907-13912, 1991.
 9. De Zeeuw, D., et al., Coupling of a global MHD code and an inner magnetospheric model: Initial results, *J. Geophys. Res.*, 109, doi:10.1029/ 2003JAA010366, 2004.
 10. Declcourt, D.C., Particle acceleration by inductive electric fields in the inner magnetosphere, *J. Atms. Solar-Terr. Phys.* 64, 551-559. 2002.
 11. Delaboudinière, J.-P., Artzner, G.E., Brunaud, J., Gabriel, A.H., Hochedez, J.F., Millier, F., Song, X.Y., Au, B., Dere, K.P., Howard, R.A., Kreplin, R., Michels, D.J., Moses, J.D., Defise, J.M., Jamar, C., Rochus, P., Chauvineau, J.P., Marioge, J.P., Catura, R.C., Lemen, J.R., Shing, L., Stern, R.A., Gurman, J.B., Neupert, W.M., Maucherat, M., Clette, F., Cugnon, P., and van Dessel, E.L., EIT: Extreme-Ultraviolet imaging Telescope for the SOHO Mission, *Solar Physics*, 162, 291-312, 1995.
 12. Demajistre, R., Roelof, E.C., C:son Brandt, P. and Mitchell, D.G., Retrieval of global magnetospheric ion distributions from high energy neutral atom (ENA) measurements made by the IMAGE/HENA instrument, *J. Geophys. Res.* 109, A04214, doi:10.1029/2003JA010322, 2004.
 13. Domingo, V., Fleck, B., and Poland, A., The SOHO Mission: an overview, *Solar Phys.* 162, 1-37, 1995.
 14. Donovan, E., et al., Global auroral imaging during ILWS, submitted to *Adv. Space*

Sciences, 2005.

15. Donovan, E., Jackel, B., Voronkov, I., Sotirelis, T., Creutzberg, F., and Nicholson, N., Ground-based optical determination of the b2i boundary: A basis for an optical MT-index, *J. Geophys. Res.*, 108(A9), doi: 10.1029/2001JA009198, 2003a.
16. Ebihara, Y., Fok, M.-C., Wolf, R.A., Immel, T.J. and Moore, T.E., Influence of ionosphere conductivity on the ring current, *J. Geophys. Res.*, 109, A12209, doi:10.1029/2004JA010523, 2004.
17. Elsen, R. K., Winglee, R. M., Spann, J. F., Germany, G. A., Brittnacher, M., Parks, G., The auroral oval boundaries on January 10, 1997: A comparison of global magnetospheric simulations with UVI images, *Geophys. Res. Lett.*, 25 (14), 2585-2588, 1998.
18. Frey, H., Mende, S. B., Carlson, C. W., Gérard, J.-C., Hubert, B., Spann, J., Gladstone, R., Immel, T. J., The electron and proton aurora as seen by IMAGE-FUV and FAST, *Geophys. Res. Lett.*, 28(6), 1135-1139, 2001.
19. Germany, G. A., Torr, M. R., Torr, D. G., and Richards, P. G., Use of FUV auroral emissions as diagnostic indicators *J. Geophys. Res.*, 99, 383, 1994.
20. Gold, R.E., Krimigis, S.M., Hawkins, R.E., et al., Electron, Proton, and Alpha Monitor on the advanced composition explorer spacecraft, *Space Sci. Rev.*, 86 (1-4), 541-562, 1998.
21. Goldstein, J., Burch, J.L., Sandel, B.R., Mende, S.B., Brandt, P. C'son, and Hairston, M.R., Coupled response of the inner magnetosphere and ionosphere on 17 April 2002, *J. Geophys. Res.*, 110, A03205, doi:10.1029/ 2004JA 010712, 2005.
22. Henderson, M. G., Reeves, G. D., Spence, H. E., Sheldon, R. B., Jorgensen, A. M., Blake, J. B., Fennell, J. F., First energetic neutral atom images from Polar, *Geophys. Res. Lett.*, 24(10), 1167-1170, 1997.
23. Henderson, M., Reeves, G., and Murphree, J., Are north-south structures an ionospheric manifestation of bursty bulk flows?, *Geophys. Res. Lett.*, 25, 3737, 1998.
24. Hovestadt, D. and Scholer, M., Radiation belt produced energetic hydrogen in interplanetary space, *J. Geophys. Res.*, 81, 5039- 5042, 1976.
25. Hovstadt, D., Hilchenbach, M., Burgi, A., Klecker, B., Laeverenz, P., Scholer, M., Grunwaldt, H., Axford, W.-I., Livi, S., Marsch, E., Wilken, B., Winterhoff, H.P., Ipavich, F.M., Bedini, P., Coplan, M.A., Galvin, A.B., Gloeckler, G., Bochsler, P., Balsiger, H., Fischer, J., Geiss, J., Kallenbach, R., Wurz, P., Reiche, K.-U., Gliem, F., Judge, D.L., Ogawa, H.S., Hsieh, K.C., Mobius, E., Lee, M.A., Managadze G.G., Verigin, M.I. and Neugebauer, M., CELIAS - Charge Element and Isotope Analysis System for SOHO, *Solar Phys.* 162, 441-481, 1995.
26. Hovstadt, D., Hausler, B. and Scholer, M., Observation of energetic particles at very

- low altitudes near the geomagnetic equator, *Phys. Rev. Lett.*, 28, 1340 - 1344, 1972.
27. Howard, R.A., Michels, D.J., Sheeley Jr., N.R., and Koomen, M.J., The observation of a coronal transient directed at earth, *Astrophys. J.*, 263, L101-L104, 1982.
 28. Jorgensen, A. M., Spence, H. E., Henderson, M. G., Reeves, G. D., Sugiura, M., Kamei, T., Global energetic neutral atom (ENA) measurements and their association with the Dst index, *Geophys. Res. Lett.*, 24, 3173-3176, 1997.
 29. Kabin, K., et al., Open-closed field line boundary position: A parametric study using an MHD model, *J. Geophys. Res.*, 109, doi:10.1029/2003JA010168, 2004.
 30. Knudsen et al., Width and structure of mesoscale optical auroral arcs, *Geophys. Res. Lett.*, 28(4), 705, 2001.
 31. Kozyra, Janet U. and Lemohn, Michael, W., Ring current energy input and decay, *Space Sci. Rev.* 109, 105-131, 2003 (reprinted in *Magnetospheric Imaging, The Image Prime Mission*, Ed. Burch, J.L. (Kluwer Acad. Publ.) 2003.
 32. Kunitake, M., and T. Oguti, Spatio-temporal characteristics of flickering spots in flickering aurora, *J. Geomagn. Geoelectr.*, 36, 121, 1984.
 33. Lam, M., et al., On-going far-tail bursty and patchy nightside magnetic reconnection during late substorm growth phase, in preparation for submission to *J. Geophys. Res.*, 2005.
 34. Linker, J.A., Mikic, Z., Riley, P., Lionello, R., and Odstreil, D., Models of coronal mass ejections: a review with a look to the future, in *Solar Wind Ten*, Proceedings of the Tenth International Solar Wind Conference, M. Velli, R. Bruno, F. Malara (eds.), American Institute of Physics, Vol. 679, 703 - 710, 2003.
 35. Lysak, R. L., Feedback instability of the ionospheric resonant cavity, *J. Geophys. Res.*, 96(A2), 1553, 1991.
 36. Maggs, J. E., and T. N. Davis, Measurements of the thicknesses of auroral structures, *Planet. Space Sci.*, 16, 205, 1968.
 37. Marsch, E., Antonucci, E., Bochsler, P., Bougeret, J.-L., Fleck, B., Harrison, R., Langevin, Y., Marsden, R., Pace, O., Schwenn, R., and Vial, J.-C., Solar Orbiter, A High-Resolution Mission to the Sun and Inner Heliosphere, *Adv. Space Res.*, 29, 2027, 2002.
 38. McEntire, R.W. and Mitchell, D.G., Instrumentation for global magnetospheric imaging of energetic neutral atoms, in *Solar System Plasma Physics*, Eds. Waite, Jr., J.H., Burch, J.L and Moore, T.E., *Geophys. Monograph* 54, 69-80, 1989.
 39. McKenna-Lawlor, Susan., Balaz, Jan., Strharvsky, Igor., Barabash, Stas., Johnsson, Klas., Lu Li., Cao Jin Bin., Shen Chao., Qingang Zong., Roelof, Edmond C., C:son Brandt, Pontus., Kudela, Karel., Fu, Suiyan. and Dandouras, Iannis., An overview

- of the scientific objectives and technical configuration of the Neutral Atom Detector Unit NUADU on the Chinese Double Star Mission, *Planet. Space Sci.* 53, 335-348, 2005 .
40. Mende, S. B., et al., Far-Ultraviolet Imaging from the IMAGE Spacecraft. 3. Spectral imaging of Lyman-alpha and OI 135.6 nm, *Space Science Reviews*, IMAGE special issue, 91, 287-318, January, 2000.
 41. Mitchell, D.G., C:son Brandt, P., Roelof, E.C., Hamilton, D.C., Retterer, K.C., and Mende, S., Global imaging from IMAGE/HENA, *Space Sci. Rev.* 109, 63-75, 2003.
 42. Mitchell, D.G., Jaskulek, S.E., Schlemm, C.H., Keath, E.P., Thompson, R.B., Tossman, B.E., Boldt, J.D., Hayes, J.R., Andrews, G.B., Paschalidis, N., Hamilton, D.C., Lundgren, R.A., Tums, E.O., Wilson, P. I, Voss, H.D., Prentice, D., Hsieh, K.C., Curtis, C.C. and Powell, F.R., High energy neutral atom HENA imager for the IMAGE mission, *Space Sci. Rev.*, 91, 67-112, 2000.
 43. Pollock, C.J., Asamura, K., Baldanado, J., Bailey, M.M., Barker, P., Burch, J.L. Corpela, E.J., Cravens, J., Dirks, G., Fok, M.-C., Funsten, H.O., Grande, M., Gruntman, M., Hanley, J., Jahn, J.-M., Jenkins, M., Lampton, M., Marckwordt, M., McComas, D.J., Mukai, T., Penegor, G., Pope, S., Ritzau, S., Schattenburg, M.L., Scime, E., Skoug, R., Spurgeon, W., Stecklein, T., Storms, S., Urdiales, C., Valek, P., Van Beek, J.T.M., Weidner, S.E., Wuest, M., Young, M.K. and Zinsmeyer, C., Medium Energy Neutral Atom (MENA) imager for the IMAGE Mission, *Space Sci. Rev.*, 91, 113-154, 2000.
 44. Reiner, M.J., Kaiser, M.L., Fainberg, J., and Stone, R.G., A new method for studying remote type II radio emissions from coronal mass ejection-driven shocks, *J. Geophys. Res.*, 103, 29,651-29,664, 1998.
 45. Roelof, E.C., C:son Brandt, P. and Mitchell, D.G., Determination of currents and diamagnetic effects from global plasma pressure distributions obtained by IMAGE/HENA, *Adv. Space Res.*, 33 (5), 747-751, 2004.
 46. Rostoker, G. and Fälthammar, C.-G., Relationship between changes in the interplanetary magnetic field and variations in the magnetic field at the Earth's surface, *J. Geophys. Res.*, 72, 5853-5863, 1967.
 47. Sandel, B.R., King, R.A., Forrester, W.T., Gallagher, D.L., Broadfoot, A.L., and Curtis, C.C., Initial results from the IMAGE Extreme Ultraviolet Imager, *Geophys. Res. Lett.*, 28(8), 1439-1442, 2001.
 48. Sato, N., et al., Conjugacy of isolated auroral arcs and nonconjugate auroral breakups, *J. Geophys. Res.*, 103(A6), 11641, 1998.
 49. Schwenn, R., Dal Lago, A., Gonzalez, W.D., Huttunen, E., St.Cyr, O.C., Plunkett, S.P., A tool for improved space weather predictions: the CME expansion speed, *EOS Trans. AGU*, 82, 47, Fall Meet. Suppl. Abstract 2001AGUFMSH12A0739S,

2001.

50. Schwenn, R., A. Dal Lago, E. Huttunen, and W. D. Gonzalez, The association of coronal mass ejections with their effects near the Earth, *Ann. Geophys.*, 23, 1033~1059, 2005.
51. Semeter, J., and R. Doe, On the proper interpretation of ionospheric conductance estimated through satellite photometry, *J. Geophys. Res.*, 107(A8), doi:10.1029/2001JA009101, 2002.
52. Sheeley Jr., N.R., Howard, R.A., Michels, D.J., Koomen, M.J., Schwenn, R., Mühlhäußer, K.-H., and Rosenbauer, H., Coronal Mass Ejections and Interplanetary Shocks, *J. Geophys. Res.*, 90, 163-175, 1985.
53. Siscoe, G., The space-weather enterprise: past, present, and future, *J. Atmos. Solar-Terr. Phys.*, 62, 1223-1232, 2000.
54. Sofko, G., et al., Direct determination of large-scale magnetospheric field-aligned currents with SuperDARN, *Geophys. Res. Lett.*, 22(15), 2041, 1995.
55. Song, P., et al., A numerical simulation of solar-wind – magnetosphere interaction for northward interplanetary magnetic field, *J. Geophys. Res.*, 104(A12), 28361, 1999.
56. Spjeldvik, W.N. and Rothwell, P.L., The Radiation Belts, in *Handbook of Geophysics and the Space Environment*, Chapter 5 (Publ. Airforce Geophys. Lab. USA), 1985.
57. Sugiura, M. and Kammei, T. Equatorial Dst Index, 1957-1986, *IAGA Bulletin* 40, ISGI, Saint Maur –des-Fosses, France, 1991.
58. Tripathi, D., Bothmer, V., and H. Cremades, The basic characteristics of EUV post-eruptive arcades and their role as tracers of coronal mass ejection source regions, *Astron. Astrophys.*, 422, 337-349, 2004.
59. Tsurutani, B.T., Gonzalez, W.D., The interplanetary causes of magnetic storms: a review; in *Geophysical Monograph*, N. Crooker; J.A. Joselyn, J. Feynman, (eds.), pp. 77-89, American Geophysical Union, Washington, USA, 1997.
60. Tsyganenko, N. A., Singer, H. J. and Kasper, J.C., Storm-time distortion of the inner magnetosphere: How severe can it get?, *J. Geophys. Res.*, 108, SMP 18-1 to SMP 18-15, 2003.
61. Uritsky, V. et al., Scale-free statistics of spatio-temporal auroral emissions as depicted by POLAR UVI images: Dynamic magnetosphere is an avalanching system, *J. Geophys. Res.*, 107(A12), doi:10.1029/2001JA000281, 2002.
62. Vegard, L. Emission spectra of night sky and aurora, *Reports of the Gassiot Committee*, Vol. 84 (Publ. Phys. Soc. of London), 1948.
63. Vegard, L. Hydrogen showers in the auroral region, *Nature*, 144, 1089-1090,

1939.

64. Webb, D.F., Crooker, N.U., Plunkett, S.P., and St.Cyr, O.C., The solar sources of geoeffective structures, Space Weather, *Geophysical Monograph*, 125, 123-141, 2001.
65. Wei, F., Liu, R., Fan, Q., and Feng, X., Identification of the magnetic cloud boundary layers, J. Geophys. Res., 108, NO.A6, 1263, doi: 10.1029/2002JA009511, 2003.
66. Wilken, B., Axford, W.I., Daglis, I., Daly, P., Guttler, W., Ip, W.-H., Korth, A., Kremser, G., Livi, S., Vasyliunas, V.M., Woch, J., Baker, D., Belian, R.D., Blake, B.B., Fennell, J.F., Lyons, I.R., Borg, H., Fritz, T.A., Gliem, F., Rathje, R., Grande, M., Hall, D., Kecskemety, K., McKenna-Lawlor, S., Mursula, K. Tanskanen, P., Pu, Z., Sandahl, I., Sarris, E.T., Scholer, M., Schulz, M., Sorass, P. and Ullalund, S., RAPID, The Imaging Energetic Particle Spectrometer on Cluster, Space Sci. Rev. 79, 399-473, 1997.
67. Williams, D.J., Roelof, E.C., and Mitchell, D.G., Global Magnetospheric Imaging, Rev. Geophys., 30(3), 183-208, 1992.
68. Williams, D.J., Why we need global observations, in *Magnetospheric Physics* (Hultqvist and Fälthammar), Plenum Press, New York, 1990.
69. Wing, S., and Newell, P.T., Central plasma sheet ion properties as inferred from ionospheric observations, J. Geophys. Res., 103, A4, 6785-6800, 1998.
70. Winglee R. M., et al., Global impact of ionospheric outflows on the dynamics of the magnetosphere and cross-polar cap potential, J. Geophys. Res., 107(A9), doi:10.1029/2001JA000214, 2002.
71. Zhou, X., and B. Tsuritani, Interplanetary shock triggering of nightside geomagnetic activity: Substorms, pseudobreakups, and quiescent events, J. Geophys. Res., 106(A9), 18957, 2001.
72. Zou, H., et al., A comparison between detections of energetic electron by ZY1/CBMC and SZ2/XD, Chinese Journal of Geophysics, 47(4), 644-651, 2004.

3. Mission objective

3.1. Remote sensing observations on KuaFu-A

3.1.1. HI Lyman- α observations of the solar disk from KuaFu-A

The solar irradiance at the Lyman- α wavelength has been recorded since 1977, and has been monitored continuously by the UARS satellite for several years since 1991. However, the brightest emission line of the solar spectrum has never been observed continuously with an imaging instrument capable of resolving features of different radiance on the solar disk. Fragmented observations were produced by rocket instruments (e.g., TRC, SwRI/LASP MXUVI), and by TRACE with a limited FOV and low spectral purity due to a large continuum contribution (Handy, 1999). The FUV telescope on KuaFu-A will provide high resolution and continuous Lyman- α images. This data set will offer crucial information to space weather forecasting. It will indeed provide images of the chromosphere and lower transition region, containing the dense filaments or prominences that are prone to eruption and may dash towards Earth. This observation is very complementary to the low corona observed in Fe XII. The EUV emission is known to be always associated with Lyman- α emission. Both types of emission trace the magnetic network. The precise evaluation of the mass content and topological configuration of an erupting solar flux tube is of paramount importance for forecasting space weather and understanding its solar causes.

Imaging of the Sun in Lyman- α at high resolution over extended period of time will greatly improve solar irradiance models. By determining the emission measure of features on the solar disk and following their dynamic evolution, proxies for the Lyman- α irradiance can be built. Reconstruction of a long-term Lyman- α irradiance timeline was in the past hindered by the lack of such reference data. These images are expected from KuaFu-A, and will allow for a better accounting of the observed Lyman- α irradiance variability. Since the Lyman- α irradiance is causal for the ozone changes and formation of the ionospheric D-region in the Earth's atmosphere, a better understanding of its variation will also be important for geophysics, atmospheric science, climate research, and aeronomy. The imaging feature will also provide the irradiance in all solid angles of the heliosphere, which is a vital input to studies of planetary atmospheres. Moreover, the L1 Lagrange point avoids the perturbation of solar measurements by the geocorona.

3.1.2. Coronal EUV observations of the solar disk from KuaFu-A

The EUV imager will produce quasi-monochromatic images of the solar emission line of iron at 19.5 nm. The precursor of this type of instrument, EIT on board the Solar and Heliospheric Observatory (SOHO), is still in operation after almost 10 years. Although it was not ‘solar weather’ dedicated originally, it has deeply influenced and transformed the field, especially thanks to its “CME watch” mode.

Due to a wide temperature response window, which is centered at the 1.5 MK line of Fe XII but includes the hot Fe XXIV emission line formed above 10 MK, the 19.5 nm images provide information on various coronal conditions. Coronal holes (the sources of the high-speed solar wind), active regions (potential sites of solar flares) and filaments (potential eruption sites) are clearly recognized in these images. Note that the same solar features are well observed with band passes centered at 17.1 or 17.5 nm, sampling other iron lines. The band pass selection is suggested to be kept open at this stage, since it has no direct incidence impact on the instrument design, apart from the multilayer coatings themselves.

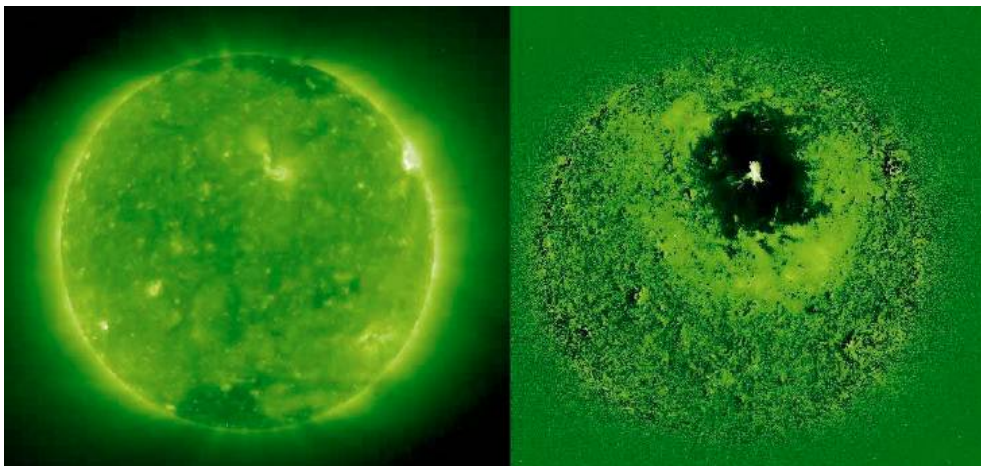


Fig. 3.1 An EIT image in the Fe XII band pass (19.5 nm) taken on 1997/05/12, just prior to a coronal mass ejection (left). On the right, a processed image showing clearly the EIT wave. This event was the earliest warning of the halo CME that would hit the Earth magnetosphere and produce an intense magnetic storm (peak Dst < -100) two days and 22 hours later.

The temporal dimension brings even more important inputs to space weather forecasters. Accurate observations require high-cadence series of EUV images to grasp the relevant solar activity. These sequences give access to more subtle disturbances such as EIT waves (faint global waves propagating across the solar disc from the eruption site), coronal EUV dimming regions (transient coronal evacuation from where the CME material has lifted off), and filament instabilities (a type of filament flickering that

serves as a CME precursor). The accurate identification of the coronal mass ejections gives a 3-day warning before the CMEs hit the Earth magnetosphere and cause geomagnetic storms. More importantly, it correlates with the swifter arrival at Earth of dangerous relativistic particles accelerated by a CME-driven possible shock.

In the future, solar EUV images are expected to also provide the boundary conditions needed to constrain MHD extrapolations. This is the prerequisite to interfacing the sets of observational data with the results obtained from the numerical codes, which subsequently model the physics in the heliosphere. Such a combined effort will pave the way to the wanted breakthrough in reliability of space weather forecast, in both qualitative and quantitative terms.

3.1.3. HI Lyman- α observations of CME from 1.1 to 2.5 R_{\odot} from KuaFu-A

To bridge the gap between the disk imagers and the externally-occulted coronagraph which is limited to 2.5 R_{\odot} , we propose that the KuaFu payload includes a Lyman- α coronagraph whose field of view extends from 1.15 to 2.7 R_{\odot} . The solar corona was first observed in this line from a rocket flown during the total eclipse of 1970 (Gabriel, 1971). In spite of the low density of the hydrogen atoms present in the corona, the strength of the Lyman- α line (121.6 nm) makes the corona quite bright. It has been convincingly shown that the coronal structures seen in Lyman- α correspond to those seen in the visible and which result from Thomson scattering of the coronal ionized gas. This is because the plasma is still collisional in the lower corona so that the hydrogen neutral atoms are coupled to the protons. This insures the validity of all diagnostics as extensively demonstrated by the UVCS spectrometer aboard SOHO. In particular, the radiance of the Lyman- α emission line is an excellent diagnostic of the distribution of the coronal density, that is the mass of the gas (it can be further noted that the strength of this line is weakly dependent upon the temperature, contrary to most other emission lines in the UV and EUV).

Spectroscopic observations of the coronal Lyman- α emission line have been performed with SPARTAN missions and most extensively by SOHO/UVCS which has performed the first and unique measurements of the solar wind well above 1.5 R_{\odot} . However UVCS is a slit spectrograph, and reconstruction of a full coronal image takes many hours of observations (consequently UVCS has only seen a few dozens of CMEs). This is not appropriate for a space weather mission such as the KuaFu, and a Lyman- α coronal imager is required. Ultimately, a spectroscopic diagnostic exploiting the technique of Doppler dimming would be highly desirable, but this ambitious and complex capability is beyond the scope and the resources available on KuaFu.

Therefore, observing the corona in the Lyman- α line is a valid alternative to white light observations, it is important to point out the potential advantages of the former approach.

- First the difficulty of observing the lower corona should not be underestimated and the SOHO/LASCO-C1 instrument has shown that instrumental stray light remains a critical issue in the visible because of the low contrast of the corona with respect to the Sun. A white light instrument will fly on STEREO and it will be of interest to see how it will perform.
- The potential superiority of the Lyman- α approach stems from the intrinsic higher contrast of the corona with the solar disk in this line compared to the visible (typically a gain of a factor 1000). This is somewhat offset by the stray-light level which is larger in the UV than in the visible. However progress in super polishing mirrors eases this limitation and altogether a gain of a factor 50 is expected in the stray-light performances of a Lyman- α coronagraph over a visible instrument.
- A further advantage is the mere absence of F-corona at 121.6 nm thus alleviating the need to separate the K and F components via polarization measurements, a process which is a source of error.

By bridging the gap between the solar disk and the inner limit of $2.5 R_{\odot}$ of the externally-occulted coronagraph, the Lyman- α coronagraph will allow to connect the coronal structures and trace the transient events (mostly CMEs) from their sources on the disk to the outer corona.

The expected high spatial resolution images of all structures (loops, arches, streamers, coronal holes, reinforcements,...) will map the distribution of the coronal density (and therefore the mass) and will further give access to the topology of the magnetic field above the photosphere, at least up to $1 R_{\odot}$ above the limb.

Coronal mass ejections (CMEs) will be detected in the low corona and easily connected to their source on the disk (flares, eruptive prominences). Their relationships to Moreton and EIT waves will be clarified. They will be tracked in the early phases of their development, allowing us to study the processes of their acceleration.

3.1.4. White light observations of CME from 2.5 to $15 R_{\odot}$ from KuaFu-A

Observing the extended corona is of utmost importance to acquire and develop a full understanding of solar activity and in particular of those phenomena, such as Coronal Mass Ejections, that are the major drivers of heliospheric and magnetospheric activity. Since the Skylab era in the early 1970s, coronagraphs have been important instruments on several solar missions, culminating in advanced telescopes such as LASCO on SOHO. Continuous imaging of the extended corona has proved to be of key importance for practical forecasting of space weather

The European solar and heliospheric community has greatly contributed to the understanding of the solar corona and the heliosphere through such important missions

as Helios, Ulysses and SOHO (LASCO, EIT and UVCS). It is actively participating in the upcoming STEREO mission, and is right now preparing for the Solar Orbiter mission to be launched in the 2013 time frame. The anticipated participation of this community in the KuaFu-A mission offers the possibility to complement these activities and increase the scientific return.

3.1.5. CME-shock related radio and plasma wave measurements from KuaFu-A

Solar radio astronomy in a broad range of frequencies provides a unique means to recognize, track and analyze energetic phenomena taking place in the solar corona and interplanetary medium, in association with solar activity and in particular to Coronal Mass Ejections.

The Waves investigation on the Wind spacecraft has recently demonstrated and exemplified the role of radio and wave observations in the study of a broad range of solar terrestrial phenomena. In particular, correlations with the SOHO optical and EUV observations of CMEs have led to major progress. This has been at the base of the STEREO mission aiming at a better understanding of the 3D development of CMEs in the heliosphere. The two spacecraft will be launched in 2006, and the mission will cover the period of the coming minimum of solar activity and the rise phase of the next cycle. So far no radio instrument is anticipated to cover the next cycle. There is thus a strong need of radio observations during the next solar cycle and beyond, for two main reasons that will be developed below: (i) essential support to a space weather program; (ii) making progress in the knowledge of fundamental problems of physics and astrophysics.

On a scientific point of view, the objectives of the investigation are twofold:

(1) provide a comprehensive and continuous survey of radio emissions in the volume of the heliosphere between the corona and the orbit of the Earth (these radio emission trace energetic phenomena such as beams of relativistic electrons and interplanetary shock waves frequently associated with both solar flares and solar mass ejections); and

(2) provide in-situ information (qualitative and quantitative) on the wave activity and plasma properties of CMEs which are directed at Earth.

Radio emission is essentially generated through the interaction of energetic electrons (produced in solar flares and shocked wind) with the ambient solar wind plasma. Most radiation mechanisms produce radiation on a frequency close to the local plasma frequency, which is directly proportional to $\sqrt{N_e}$, leading to the strong frequency-distance dependence shown in Table 3.1.

Radio and plasma wave instrumentation on board a spacecraft usually covers the

measurement of both the electric field and magnetic field in a broad frequency band, ranging from a fraction of 1 Hz up to several 10 MHz, which covers characteristic frequencies in the solar corona and interplanetary medium. For instance, the so-called Wind/Waves instrument measures both electrostatic waves and electromagnetic waves, leading to different diagnostics: electrostatic waves mostly provide in-situ information, in the close vicinity of the spacecraft, while electromagnetic waves can provide extensive remote sensing of energetic phenomena in the solar corona and interplanetary medium.

Table 3.1: Radio frequency ranging in the interplanetary space

	electron density N_e (cm ⁻³)	radio frequency
low corona	$\sim 10^8 - 10^{10}$	100 MHz – 1 GHz
medium corona	$\sim 10^6 - 10^8$	10 MHz – 100 MHz
$\sim 10 R_\odot$	$\sim 10^4$	~ 1 MHz
$\sim 40 R_\odot$	$\sim 10^3$	~ 300 kHz
~ 1 AU	~ 10	~ 30 kHz

In order to achieve the scientific objectives of the KuaFu-A mission, the radio and plasma wave investigation will have to measure the electric fields in a large range of frequencies in order to address both remote-sensing and in-situ measurements of active phenomena in interplanetary space. The receiver will cover the range from a few kHz (e.g., 4 kHz) up to several 10 MHz (e.g., 20 MHz), corresponding to frequencies in the interplanetary medium from the upper corona (about one solar radius above the surface of the Sun up to the orbit of the Earth, and giving access to some in-situ measurement capability).

The instrument will measure the solar and interplanetary radio waves in the frequency range from a few kHz up to about 20 MHz, giving access to the medium corona (above $2 R_\odot$ from Sun center) up to 1 AU.

Since radio radiation is generally beamed (with typical half-power beam widths of 60 degrees, sometimes less) more or less along a radial direction from the Sun, this technique is particularly relevant to observe and measure the progression of events directed at Earth.

3.1.6. Hard X-ray/Gamma-ray observation from KuaFu-A

Although over the past decades high energy X-Ray and gamma-ray observations have been done many times, some of the primary questions concerning the fundamentals of flares and CMEs still remain unsolved. High energy X-ray and Gamma-ray observations constitute a unique diagnostic of flare accelerated electrons and ions up to relativistic energies which are basically independent of the magnetic field. Solar hard X-rays and gamma-rays are by-products of solar flares due to the interaction of high energy electrons and ions with the solar atmosphere. Spectroscopic observations

of hard X-rays to gamma-rays can provide important clues to the plasma heating and particle acceleration processes. Especially hard X-ray observations provides the most direct information for understanding the energy release processes and the electron acceleration mechanisms, and the gamma-ray observations provide irreplaceable information for study of the highest –energy flare phenomena.

Optionally, incorporation of a facility to image the solar X-Ray and gamma-rays into the KuaFu mission would greatly enhance the scientific return.

3.2. In situ observations on KuaFu-A

3.2.1. ICME in situ observation

The Solar Wind Instrument Package (SWIP) will continuously observe the solar wind status and variability (stream structure, co-rotating interaction regions, Alfvénic fluctuations, shock waves, magnetic clouds). SWIP will measure the basic plasma parameters of the solar wind right in front of the Earth:

- Proton velocity, density, and temperature, needed for analyzing the actual status of the solar wind (slow wind, high-speed stream, sheath plasma, ejecta) that is about to hit the Earth system.
- Plasma electron velocity distribution, needed for completing the knowledge of the solar wind status. In particular, suprathermal electrons (energies of 100 to 400 eV) will allow us to determine the presence of magnetic clouds.
- Interplanetary magnetic field (IMF), needed for determining the magnetic topology of the impinging solar wind, in particular with respect to the occurrence of a southward pointing B_z . This happens in the course of Alfvénic fluctuations (typically in high-speed streams) and in magnetic clouds (in the aftermath of CMEs). The magnetometer instrument on the KuaFu-A spacecraft must measure it with high precision (better than 1nT) and at a time resolution of 1s or better. In the year 2012, KuaFu-A may be the only spacecraft exploring the solar wind and magnetic field at L1, and hence the input conditions into the terrestrial system – essential information for understanding the Earth’s magnetospheric dynamics. However, it is likely that at least one other spacecraft will be operating at L1. In this case, combining data with KuaFu-A will allow the measurement of the 3D structure of the interplanetary magnetic field, both in the background solar wind and within coronal mass ejections and co-rotating interaction regions. This 3D structure controls the propagation of energetic particles, such as cosmic rays, throughout the solar system and Kua-Fu measurements would help us to understand this fundamental plasma physics problem. In addition, the relative times at which structures pass multiple spacecraft can be used to deduce their orientation. This can then be used to predict the arrival times of such structures (shocks, southward magnetic field turnings) at the Earth

more accurately than is possible with a single spacecraft.

3.2.2. Solar energetic particles observation

The Solar Energetic Particle Sensor (SEPS) is designed to measure the fluxes of energetic particles accelerated at flare sites and at shock fronts. Ion energies of up to 100 MeV/nucleon and electron energies up to 7 MeV should be covered, with a modest spectral resolution. Instruments of this type have been used on many space missions. The SEP telescopes of the IMPACT instrument on STEREO could serve as a guideline (see <http://sprg.ssl.berkeley.edu/impact/instruments/index.html>). The time resolution should be of the order of one minute.

3.3. Global imaging on KuaFu B1+B2

3.3.1. Electron and proton aurora continuous imaging

3.3.1.1. FUV Auroral Monitoring Cameras (UVAMC)

Global auroral imaging began in the early 1970s with the Auroral Scanning Photometer (ASP) on ISIS2 satellite (launched April 1, 1971). ASP used the satellite spin and its orbital motion to provide the very first global auroral images (obtained in both 557.7 nm and 130.4 nm once per orbit). The ISIS2 system was operated for almost 10 years and yielded a number of discoveries, including the diffuse auroral oval [Lui et al., 1975].

Since ISIS2, global auroral imaging has evolved significantly. Imagers on Kyokko, DE 1, HILAT, and Polar Bear operated in the UV, allowing for the first time imaging of the aurora on the dayside. Global imagers on Dynamics explorer and Viking allowed more than one image per pass, with the Viking UV instrument providing an impressive cadence of one image every 20s. In fact, the Viking instrument utilized a combination of UV filters, UV-reflective coatings, and a UV-sensitive image intensifier fiber-optically coupled to a 256 by 256 pixel CCD to obtain short-exposure (1s) simultaneous global UV images in the LBH-short band and the LBH plus an extension into the part of the spectrum including the 1304 Å OI line. Viking provided an exciting new picture of the global time-evolving auroral distribution and new insights into the substorm dynamic [see *Henderson et al.*, 1998]. Images from the two filters could be used to estimate energy deposition and the mean electron energy, however resonant scattering and a requirement of knowing the O/N₂ ratio seriously limited the accuracy of these derived quantities.

The next significant leap forward in global imaging came with the ISTP Polar satellite, which carried two imaging packages. The Visible Imaging System [VIS; see

Frank et al., 1995] consists of two cameras for night-side auroral imaging in the visible wavelengths. The two cameras deliver images with different spatial resolutions (~ 10 and ~ 20 km at apogee), and have produced images that have been widely used in studies of magnetospheric dynamics [see, eg., *McWilliams et al.*, 2001; *Nakamura et al.*, 1999]. In addition to VIS, Polar carries a UV imaging package (UVI for Ultraviolet Auroral Imager), which provides images of the entire auroral oval for roughly half of the 18-hour Polar orbit. Polar UVI has also been widely used in studies of global magnetospheric dynamics [see, for example, *Sergeev et al.*, 1999]. The nominal UVI spatial resolution is 50 km at apogee, with an integration time of ~ 30 seconds and sensitivity of $50 R_E$. This sensitivity is still the best ever achieved with a global imager.

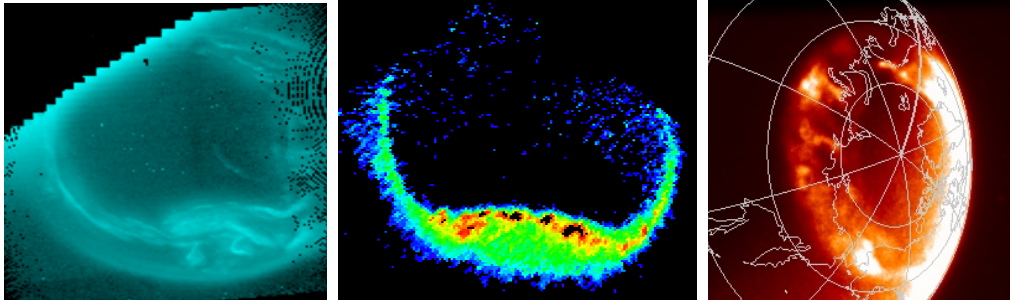


Fig. 3.2: Left: ISIS II image of the global aurora obtained in 1971 (once per orbit); middle: Viking image from April 1, 1986 (once every 20 seconds); right: IMAGE FUV WIC.

Auroral imaging from space has, for over thirty years, been our only true method for studying the spatio-temporal evolution of the magnetospheric system. In the very early days, global auroral images proved in an instant the existence of both the continuous auroral oval and the diffuse aurora. Global electron auroral images have been used to map the evolution of the substorm expansion, the effects of solar wind pressure pulses on the central plasma sheet, and the steady-state nature of dayside reconnection under at least some circumstances. Because of global auroral imaging, we are able to study the complex interplay between convection, conductivity, and field-aligned currents. Whenever they are available, global auroral images are used for essential context for other studies. As global auroral images are not available on a continuous basis, they have not been widely used in space weather.

The science requirements that would drive the design of the UVAMC are as follows:

1. The need for determination of characteristic energy and energy flux of precipitating electrons on a global scale [motivates isolation of LBH-L and LBH-S];
2. The need for global images with ~ 30 km spatial resolution to facilitate studies of Multi-scale processes and natural complexity [motivates large CCD and selection of FOV];
3. The need to image dim features [places limitations on CCD size, aperture, and

FOV, and places strong requirements on optical throughput].

The UVAMC instruments would each be comprised of two FUV imagers and a common electronics box. The two component imagers on each obtain global images at a 30s cadence (corresponding to the satellite spin period which is in turn determined by the requirements of the FUVSI – see below). They would deliver quantitative intensities from well separated parts of the LBH band, with the objective of using relative and absolute intensities for determination of characteristic energy and energy flux of precipitating electrons on a global scale. Our technical objective is 10^{10} out of band pass rejection. In order to achieve the spatial resolution that we are aiming for from near apogee, the instrument must have at least a 512×512 pixel CCD and a FOV that is wide enough to span the entire auroral zone and polar cap for a significant fraction of the orbit. Finally, the aperture must be as small as possible (for compactness and lower mass) while admitting enough light for reasonable signal to noise for dim aurora (i.e., in the tens of Rayleighs integrated across the appropriate part of the spectrum).

The heritage for these imagers are the past University of Calgary FUV instruments (Viking, Freja, InterBall, and IMAGE-WIC); however, the design of this new instrument will need to be different if we are to meet our technical objectives, and hence our scientific objectives. In particular, we propose moving to a 3 mirror design, which permits us better out of band pass rejection. **This new instrument will provide wavelength separated LBH electron auroral observations with ~30 km resolution over the global auroral distribution. Furthermore, it will image even dim aurora (~20 Rayleigh features).**

3.3.1.2. FUV Spectro-Imager (FUVSI)

Scattering of solar Lyman- α by the geocoronal hydrogen surrounding the Earth produces the Lyman- α emission line at 121.6 nm. Part of the auroral Lyman- α emission of neutral hydrogen is due to charge exchange of energetic protons that cascade into the atmosphere. One objective of the FUVSI instrument is the imaging of this type of Lyman- α emission. As the protons penetrate into the atmosphere, they capture electrons from the major constituents by charge exchange reactions. They become fast neutral hydrogen atoms radiating Doppler-shifted Lyman- α emission. A high spectral resolution is needed because the greatest intensity emission is quite close to the cold Lyman- α wavelength. Unfortunately, the size and weight of the spacecraft instrumentation limit the spectral resolution. A limit of 0.2 nm was defined which means that efficient detection of protons only occurred at several keV energy ranges.

Precipitating electrons produce several other bright, discrete auroral emission features in the FUV range which favorably compete with the day-glow emissions. For the electron aurora, the brightest is 130.4 nm OI, which is multiply scattered in the atmosphere and thus cannot be used for auroral morphology studies. In that respect, the OI 135.6 nm line is an excellent emission feature for imaging and can be related to the total electron precipitation. A primary requirement of the measurement is a spectral

separation of the 135.6 emission from that of 130.4 nm. Separation of the 130.4 and 135.6 nm lines necessitates the use of a spectrometer because even reflective narrow-band filter technology cannot satisfy the ~ 3 nm wavelength resolution requirement.

Science requirements driving the FUVSI design are:

- (1) to image the entire auroral oval from a spinning spacecraft at 6 (TBC) R_E apogee altitude.
- (2) to separate spectrally the hot proton precipitation from the statistical noise of the intense, cold geocoronal.
- (3) to separate spectrally the electron and proton auroras. FUV consists of two imagers that combine high spectral discrimination, high spatial resolution, and the greatest possible sensitivity to meet these requirements.

The first requirement drives the 15-degree FOV. The second requirement needs a high spectral resolution, better than 0.2 nm. The Doppler-shifted Ly- α signal to be detected is 100 times less intense than the Lyman- α coronal emission at 121.6 nm. Nitrogen emissions near 120 nm (triplet lines at 119.955, 120.022 and 120.071 nm) also have to be filtered out. The third requirement means that the 135.6 nm signal has to be isolated from the 130.4 nm line. The spatial resolution requirement specifies that, from 7 Earth radii, the aurora must be imaged with a 90×90 km resolution. The related angular resolution is then about 7×7 arcmin driving to a detector of 128×128 pixels. The relatively high wavelength resolution requirement is satisfied by the FUVSI. The 0.2 nm wavelength resolution drives the size of the instrument and consequently the number of mirrors in the optics system. Also the narrowness of the slits in the spectrometer limit the dwell time during which a pixel is in the field of view.

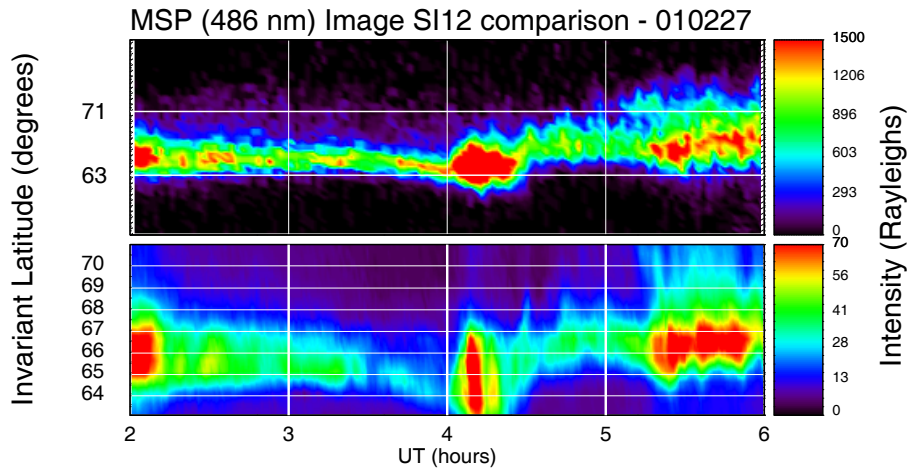


Fig. 3.3: Comparison of proton auroral observations obtained in Lyman- α by the SI12 on IMAGE, and in Balmer- β by the CANOPUS MSP at Gillam. To facilitate visual comparison, a

keogram has been constructed from the S12 data.

The FUVSI instrument was selected to fly on the NASA mission IMAGE in 2000. The data (see, for example, figure below) show that the specifications, which drove the development of the instrument, were justified.

3.3.2. Conjugate aurora activity imaging

The KuaFu mission will enable the continuous imaging of the global auroral oval in the northern hemisphere. In turn this continuous global imaging will provide crucial information on the response of the auroral oval during magnetic storms which tend to have time scales of days and represent the major large scale manifestation of “space weather” events in the ionosphere. However, imaging of one hemisphere alone does not provide full information on the auroral response to large scale energy input on the southern auroral oval is not likewise being imaged. The purpose of the Wide Field Auroral Imager is to provide such systematic coverage.

The science case for systematic conjugate imaging is easy to make. As stated above, there is a dearth of such observations from past missions and ground-based programs because conjugate imaging was never a primary motivator of those programs. We know that conjugate imaging is important. With such imaging, we can explore when diffuse and discrete auroral forms are conjugate and when they are not. Such work will immediately uncover flaws in our understanding of inter-hemispheric mapping, situations where parallel electric fields decouple the two hemispheres, and either confirm or refute our understanding of various forms of diffuse aurora. Conjugate imaging will be particularly valuable when brought to bear on substorm optical onset, PBIs, cusp aurora during northward IMF, trans-polar arcs, and the global auroral response to storms.

Systematic conjugate imaging will be provided by observations of the southern auroral oval as one satellite passes through perigee. In principle, we could use the UVAMC imagers to carry out this task. However their FOVs will be selected to facilitate viewing of the whole oval from above 4 R_E . This FOV will be too narrow for *optimum* conjugate viewing from perigee, so it is desirable to carry a light-weight wide FOV imager designed specifically for qualitative global imaging from near perigee. In other words, this imager would not meet the strict wavelength isolation, spatial resolution, and SNR requirements that the UVAMC would be held to.

The Wide Field FUV Auroral Imager provides high resolution, multi-wavelength auroral imaging in a low-mass, compact package. The novel use of a microchannel plate (MCP) as focusing optic allows a wide field-of-view camera, suitable for both perigee and apogee imaging, to be fitted into an instrument of approximate dimensions 100×100×100mm, and a mass of 1kg. Several instrument configurations are possible, optimized for different orbital and spin characteristics.

3.3.3. Ring current remote sensing

In addition to the requirements described (above) in relation to auroral research, a global perspective is also needed when investigating many fundamental aspects of magnetospheric physics (for example, particle origins, loss processes, transport mechanisms and their time dependence). These topics are all inextricably linked to two of the most important dynamic features that characterise the magnetosphere - namely geomagnetic storms and substorms (Alexeev, 2003). The ring current as an indicator of magnetic storms, will, for the first time, be continuously, remotely, globally, sensed by a pair of neutral atom imagers on KuaFu (NAIK).

Energetic Neutral Atoms (ENAs) in the Earth's magnetosphere are produced via a charge exchange mechanism between singly charged magnetospheric ions and atoms of the exosphere. The neutrals produced leave the interaction region with essentially the same energy and velocity as the originally impinging ions and they are unaffected by ambient electric and magnetic fields. They can, thus, be utilised to remotely image (aboard suitably instrumented spacecraft), interacting plasma populations in the neutral gas in which they were created. Since ENA emissions are directional and determined by the ion pitch-angles at their point of origin, some ENAs are, in addition, directed Earthward where they undergo additional charge exchange collisions in the dense, low altitude, atmosphere and contribute to the formation of a low altitude Equatorial Radiation Belt (Hovestadt *et al.*, 1972)

Since ENA images are pitch-angle sensitive, they can be used to reconstruct the ion distribution function of the inner magnetosphere. Neutral atom images of plasma structures in geospace are composed of integrals made along lines-of-sight from the vantage point of a suitable measuring instrument aboard a spacecraft.

Although morphology and dynamics is directly associated with ENA images, the parent ion distribution must be retrieved from ENA images. There are several techniques for achieving this, of which the most useful is the Constrained Linear Inversion technique of DeMajistre *et al.* (2004).

Once the ion distributions have been derived, it is straightforward to proceed to derive the relevant global pressure distribution and the associated electrical currents present (following a procedure developed by Roelof *et al.*, 2004). It is, thereafter, possible to compute the associated magnetic disturbances using the Biot-Savart Law.

Historical-Present Background

The first report of energetic neutral atom production was made by Vegard (1939) when describing a diffuse and shifted H β line in the auroral optical spectrum, which he correctly interpreted to be Doppler-shifted radiation associated with energetic precipitating protons neutralized in the upper atmosphere (see also Vegard, 1948). Thereafter, Hovestadt and Scholer (1976) suggested that ENAs produced as a result of charge exchange between trapped protons and exospheric neutral hydrogen might be

used to remotely sense the Earth’s ring current. An overview of the historical developments that, thereafter, lead to the sophisticated ENA imagers of the present day is contained in McKenna-Lawlor *et al.* 2005.

At present, there are a number of ongoing and planned ENA experiments comprising instrumentation either already in operation or shortly to be flown. These include:

- (1) The Imaging Proton Spectrometer (IPS), which is part of the Comprehensive Energetic Particle and Pitch Angle Distribution (CEPPAD) instrument on the POLAR spacecraft. Based on CEPPAD ENA measurements, Jorgenssen (1997) formulated a new global magnetospheric GENI (Global Energetic Neutral Atom Index) index that better reflects ring current behavior than does the Dst/Dst* Indices used in earlier studies to indicate magnetic storm intensity (see, for example, Sugiura and Kannei, 1991; Kozyra and Liemohn, 2003).
- (2) A special operational mode of the Imaging Energetic Particle Spectrometer (RAPID) on CLUSTER, is configured to allow ENAs to be detected (Wilken *et al.*, 1997). See also the restricted capability of the Charge Element and Isotope Analysis System (CELIAS) aboard SOHO to measure ENAs (Hovestadt *et al.* 1995).
- (3) The Magnetopause-to-Aurora Global Exploration (IMAGE) spacecraft presently carries ENA imagers that detect LENAs (10-300 eV); MENAs (1-30 keV) and HENAs (10-200 keV. Relevant to KuaFu-B is the IMAGE capability to detect MENAs and HENAs. (see, for example, Pollock *et al.*, 2000 and Mitchell *et al.*, 2000).
- (4) The NeUtral Atom Detector Unit (NUADU) aboard China’s Double Star polar spacecraft is currently successfully recording ENA data. Simultaneous measurements with IMAGE (MENA/HENA) are made during serendipitous intervals when favorable orbital configurations permit the ring current to be jointly viewed from the two spacecraft.
- (5) The TWINS mission comprises two high-inclination, high altitude spacecraft provided by a, non-NASA, US organization. Wide-angle imaging neutral-atom spectrometers on each potentially provide a pair of vantage points for ENA imaging in the energy range 1-70 keV. Each spacecraft will follow a Molniya orbit (63.4° ; $7.2 R_E \times 1000 \text{ km}$, 12^h), and will be three-axis stabilized, with approximately nadir pointing. Each will acquire image data with a time resolution of 60s. Twelve seconds (without data collection) are required between images, providing a duty cycle for data collection of 83%, and an effective time resolution of 72s. The nominal design lifetime for each instrument is four years. The launch date for the first spacecraft may be in 2005, although this cannot be confirmed.

The information outlined above indicates that neutral atom imaging is recognized, world wide, to be a very powerful technique for studying magnetospheric physics and

this has prompted the development of an advanced imaging instrument (NAIK) for the KuaFu Project - with heritage from NUADU on Double Star. NAIK has the capability to record full 4π Energetic Neutral Atom (ENA) distributions through employing sixteen solid state detectors and exploiting spacecraft rotation.

ENA Science

ENAs are produced in the Earth’s atmosphere via a charge exchange mechanism between singly charged energetic ions and the cold neutral atoms of the exosphere. Since they are not affected by ambient electric and magnetic fields, directly propagating ENA particles can be used to image, and remotely diagnose, plasma populations in the neutral gas in which they are created. Thus they, in effect, provide a means to make the active magnetospheric plasma visible. The ENA data recorded by NAIK can provide insights into circumstances in the Ring Current responsible for stimulating those magnetic storms/sub-storms, that underlie various aspects of space weather. Outstanding physics problems that can be associatively addressed include:

- Determining the morphology of the ring current under different magnetospheric conditions so as to characterize the inner magnetosphere under changing space weather conditions.
- Study of particle energization processes in the inner magnetosphere; of plasma convection and of sub-storm injections;
- Continuous observation of the global ENA index;
- Study of the interaction of the ring current with the upper atmosphere;
- Investigation of the inter-relationship between the ring current and the electric field of the inner magnetosphere;
- Exploring the role of the CPS as a source of particles for the ring current (in conjunction with UVAMC and FUVSI).

ENA images provide unique morphological information concerning the ring current (e.g. its global asymmetry, energy dependent particle drifts, locations of initiating plasma injections etc.). By suitably composing ENA images into ENA moves, it is possible to study the dynamic responses of the ring current to changes in interplanetary conditions and to observe the processes of ring current growth and decay.

Space Weather Studies

Since the dynamics of the ring current reflect, to a large extent, space weather conditions, ring current studies currently constitute a key element in space weather research.

ENA images of the ring current can be used to infer the plasma pressure and gradients that drive the current systems of the inner magnetosphere during storms (Roelof *et al.* 2004). In turn, knowledge concerning pressure development during geomagnetic storms is a vital component in understanding stretching of the Earth’s

magnetic field lines (Tsyganenko *et al.* 2003). The energization and loss of radiation belt protons and electrons are each believed to be intimately related to the topology of the magnetic field in the inner magnetosphere.

By studying sequences of plasma pressure variations obtained from ENA images recorded aboard KuaFu-B, it will be possible to relate the instantaneous responses of the ring current to those changes in interplanetary conditions detected upstream at KuaFu-A, (while recognizing that some modification of the drivers can occur between L1 and the Earth).

Magnetosphere-Ionosphere (M-I) Coupling

The analysis of ENA data already obtained aboard IMAGE, indicates that significant effects on global ring current morphology are produced due to M-I coupling (Brandt et al. 2002, Brandt et al., 2005 Goldstein et al. 2005). In this regard, the Region-2 current system was found to be driven by the pressure gradients in the inner magnetosphere which, in turn, were recognized to distort the local geomagnetic field. Plasma pressure in the inner magnetosphere provides, overall a key to understanding (a) M-I coupling and (b) the diamagnetic effects related to those adiabatic electron radiation belt dynamics that pertain during geomagnetic storms.

Also, it was possible to observe plasma sheet dynamics during substorms out to $\sim 15 R_E$. From storm onset, the ENA fluxes from the plasma sheet were found to typically increase by an order of magnitude over some 30 min. The fluxes were subsequently restored to their original level during the substorm recovery phase. At the time of onset, oxygen ions were observed to become energized and intensified by about an order of magnitude more than was the case for protons (Mitchell *et al.* 2003). This is likely to have been due to non adiabatic behavior related to the gyro-period of the heavy ions (Delcourt, 2002). Such effects can be observed continuously by the NAIK instruments aboard KuaFu-B at 30s resolution. (It is noted that the spin period of IMAGE is two minutes, and that ENA imaging is constrained to periods when this spacecraft is above the radiation belts).

Field Aligned Currents

An important contemporary topic is the effect of the differences in the conductivity of the two terrestrial hemispheres. Depending on the season, one hemisphere receives less sunlight and, in consequence, displays lower conductivity as well as higher auroral precipitation. Because of the conductivity difference, there has to be field-aligned current flow between the two hemispheres. This can be investigated over the period of the KuaFu-B mission using the NAIK imagers, supported by complementary data provided by complementary onboard experiments.

Conductance can be estimated from EUV images of the auroral region as has been already demonstrated in Ebihara et al. 2004, and references therein. Simultaneous observations of the morphology of the ring current can impose valuable constraints in the matter of modelling global M-I coupling. In essence, the estimated conductances can

be used in the models to estimate how the ionospheric conductance affects the electric field distribution and, thereby, the ring current morphology.

Overview of NAIK on KuaFu-B

A Neutral Atom Imager (NAIK) instrument will be flown aboard KuaFu-B1 and KuaFu-B2. The main scientific objective of this experiment is to obtain Energetic Neutral Atom (ENA) images of the Earth’s ring current in the approximate energy range 20-300keV.

ENA images recorded aboard KuaFu-B will provide the first ever 24×7 observations of ring current dynamics. Thus, although the NAIK instrument is closely within the heritage of NUADU, the orbit traversed and twin spacecraft configuration allows a technical breakthrough to be achieved in the matter of supporting continuous ring current observations. Against this backdrop, the time resolution of 30s will allow very rapid changes in the ring current to be imaged, allowing unique information to be made available as to how the ring current responds to changing interplanetary conditions.

Added value will be obtained through planning complementary observation campaigns with other instruments of the payload.

3.4. In situ observations on KuaFu B1+B2

KuaFu-B1 & B2 would most likely be the only polar orbiting high altitude satellites during that timeframe. The importance of the cusp, lobes and high-latitude plasma sheet in the transport of mass and energy within geospace and in particular to the inner magnetosphere and the ionosphere make it urgent that KuaFu-B carry at least some *in situ* instrumentation. This is even more important given that KuaFu has the overarching scientific objective of quantifying solar and solar wind inputs to geospace and their consequences on the CPS, inner magnetosphere and the IT system. We recognize and acknowledge that the global perigee imaging are the *raison d’être* for KuaFu-B, but we are committed to fielding *in situ* instruments on the satellite pair.

The KuaFu-B *in situ* package will consist of three instruments. The first is the fluxgate magnetometer, which is a mainstay of *in situ* geospace observations. Given the successes of Polar and Cluster, it is clear that we cannot do state-of-the-art science with a stand-alone magnetometer, and at least some *in situ* particle observations are required. Furthermore, high-energy particle observations will contribute to a global constellation of radiation-belt observations (RBSPs, ORBITALS, & navigation satellites), and further our mission objective of studying the interactions between various geospace plasma regions (i.e., the CPS, plasmasphere, and ring current).

3.4.1. Magnetic field observation

The magnetometer on the KuaFu-B is a high-precision instrument designed to provide measurements of the vector magnetic field in space along the $7 R_E \times 1.8 R_E$ orbit at both high and low altitudes in the polar magnetosphere. This orbit is designed to probe both northern and southern high latitude magnetosphere in the region of the cusp around the apogee simultaneously. Around the perigee, the auroral electron acceleration will be investigated. The magnetic fields investigation will be used to investigate the field-aligned current systems and the role they play in the particle acceleration. Moreover, it will also help to organize and interpret data from other instruments, especially the experiments for energetic particles, plasmas, and electric fields experiments on KuaFu.

The magnetometer is sensitive enough to measure perturbations produced by currents and waves as small as 0.25 nT (a much improved resolution than Polar magnetometer which is 10 nT) in perigee (typical ± 8000 nT), and 8 pT (Polar magnetometer: 100 pT) in a 200 nT field (typical at apogee). Thus the small amplitude of the magnetic field oscillations associated with field-aligned currents will be measured in an accuracy never achieved before. In the sense of data rate, KuaFu will be much better than the earlier or current missions. For Polar magnetometer, the nominal high data resolution is 8 vectors per second. We plan to have the 128Hz data along the KuaFu orbit. The high time resolution data will enable us to study the turbulence and non-linear process in the cusp region caused the particle acceleration for the first time.

Overall, the magnetometer plays a key role in coordinating the KuaFu plasma investigation of the magnetosphere.

The fluxgate magnetometer is a three-axis system using high, stable, low noise, ring core sensors to provide magnetic field information for DC to 100 Hz. It takes the heritage of the Venus Express magnetometer, with slightly modification to accommodate the Earth's orbit. For example, we need to consider the Earth radiation environment in designing the electronic box thickness. We have to re-design the measurement range to make the instrument more flexible in the Earth magnetic field.

It consists of two triaxial fluxgate sensors. The dual sensor configuration was chosen for better measuring the stray magnetic fields produced from other S/C units, and for redundancy. The electronics box comprises two sensor electronics boards, the DPU board and the DC/DC converter. The electronic box weighs only 1000 g. However, this number might increase slightly if we have to increase the thickness of the box wall. Please note that the harness mass is not included in our calculation because the harness length/mass is dependent on the boom length.

3.4.2. Energetic particles events observation

The enhancement provided by KuaFu over previous missions is also that it

provides two-point measurements, and conjugate *in situ* measurements in particular, in the context of continuous auroral imaging

3.4.2.1. Medium-Energy Charged Particle Imager (IES/IPS)

Both the energetic protons and electrons provide a powerful diagnostic of acceleration processes that operate in the ring current, auroral region and in the dayside cusp boundaries, so their continued measurement, *in situ*, is a vital part of the mission. The near-instantaneous response of energetic electrons enables active phenomena, such as the onset of reconnection and substorm behavior in general, to be closely related to the prevailing magnetic structure. They can provide near-instantaneous information about distant regions of geospace, due to the great speeds they achieve along field lines, approaching 20 R_E/s at 50 keV, whilst preserving the mapping of magnetic topology, owing to their relatively small gyroradii (typically less than 50 km at 50 keV). Energetic ions, conversely, have large gyroradii, which can sense the existence or approach of boundaries over thousands of kilometers.

One of the key scientific objectives of continuous auroral imagery is the ability to determine the size of the polar cap, and hence the open flux content of the magnetosphere. The poleward boundary of the auroral oval is a good proxy for the open/closed boundary, but for detailed work it is necessary to "calibrate" the auroral observations with particle measurements. These simultaneous measurements of both energetic electrons and protons also allow the diagnosis of the particle populations that are giving rise to the aurora, being observed continuously. This diagnosis involves investigation of acceleration processes, field-line mapping from high altitudes to the ionosphere and the associated current systems.

Specific science objectives would be to:

- identify to identify key plasma regions (e.g. cusp and lobe) using the two spacecraft locations.
- quantify the amount of open flux in the magnetosphere by combining continuous auroral imaging of the open/closed field line boundary with *in situ* plasma measurements.
- quantify the response of the auroral region to solar wind-magnetosphere coupling and substorms.
- study the distribution of energetic ions in the cusp and adjacent regions.
- identify the substorm-associated precipitation, connection between tail reconnection and the auroral bulge.
- link the connection of particle signatures in the cusp with dayside auroral features, e.g. the relationship between FTEs and poleward-moving auroral forms (PMAFs).

- Locate the lobe reconnection (northward IMF) and cusp auroral spot using in particular conjugate measurements.
- determine response of the ring current to interplanetary events

3.4.2.2. High energy charged particle experiment

Electrons in the Earth’s radiation belts range in energy from 400 keV (a somewhat arbitrary lower limit to be considered a radiation belt electron) to above 15 MeV. The increase of the flux of high energy electrons is related to the process of the Sun-Earth storms.

The damaging aspects of solar energetic particles on spacecraft come mainly from fluence effects. Protons and other ions in the ten to several hundred MeV range are very penetrating, and one large event can be as damaging as many years of normal on-orbit operation in the space environment (Baker, 2000).

Effects on satellite hardware of the radiation environments have been reviewed by Baker (2000, 2001). Satellite systems can be impaired by surface damage or through direct penetration of the electronics by high velocity solar protons, and by deep or surface-charging (Baker, 2000). The high energy protons or ions can cause the single event upsets (SEU) and single event latchup (SEL) in space electronics systems. Most of SEUs cause the software faults. Some kinds of SEL are recoverable, but some are unrecoverable that may permanently damage the device. The high energy electrons can penetrate the skin of satellite and accumulate in the insulator to cause deep charging and discharging pulse which may be the consequence of the satellite faults or damages.

The enhancements of the high energy electron and proton, so-called energetic particle events, are important phenomena of the “Space Weather”(Gold, et al., 1998). The measurements of high energy electrons and protons are important for the “linkage of causes and effects” in solar-terrestrial space. Particles can be accelerated by unclear processes in the magnetosphere; their relatively fast motion can carry information about the energization process over significant distances to an observing platform, and provide important clues on the nature of the process. Furthermore, their kinetic properties can be used to trace out plasma structures over distances as large as an Earth radius. Information can even be transmitted over global distances by the rapid drift of energetic particles in field gradients or, even more important, by field-aligned swift electrons traveling with speeds comparable with the speed of light. The particle environments both in- and out-board the satellite will be simultaneously registered by KuaFu B.

KuaFu-Bs will pass through the inner and outer radiation belts, and cover large range of L value (1.1 to 9). The High Energy Charged Particle Experiment (HECPE) onboard KuaFu B will detect simultaneously the in- and out-board radiation environments to show the direct effects on the satellite of the charged particles. The goals of HECPE are:

- (1) to investigate whole radiation belt of the Earth;
- (2) to make in-situ measurements of the fluxes of the high energy electron with MeV order and proton with ten MeV order;
- (3) to directly show the in- and outboard connections of the satellite radiation environment, and give direct observation of the “linkage of causes and effects” in solar-terrestrial space.

The energy ranges covered by KuaFu B can be determined as

- (1) For electrons: $E > 0.5$ MeV, $E > 1.0$ MeV, and $E > 2.0$ MeV.
- (2) For protons: 5-10 MeV, 10-20 MeV, 20-40 MeV, and 40-80 MeV.

The low limits of the measurement energy (0.5 MeV for an electron and 5 MeV for a proton) are determined by considering those particle can or might penetrate the skin of satellite to threaten its work. The high limits are determined by two reasons. One is that the fluxes of the electrons with more than 4 MeV and protons with more than 100 MeV are much lower. The other reason is due to the technical limit of the instrument.

3.5. Radio science experiments on KuaFu B1+B2

KuaFu-B would be an important platform that must be utilized to carry innovative new instruments that can remote sense with radio as well as optical techniques. The radio techniques that would be utilized as part of KuaFu-B would carry out important space weather and space science functions, would contribute to the overarching KuaFu and ILWS objectives of system-level geospace science, and would be an important technology pathfinder for applications of these techniques on future missions.

Radio frequency transmissions from Low Earth Orbiting (LEO) Satellites can be used to study the plasma in the upper atmosphere by (1) providing profiles and two dimensional images of the ionosphere and (2) observing phase and amplitude scintillations induced in radio waves propagating through the ionosphere. In addition, the received radio data can be applied to the neutral atmosphere by (a) detecting horizontal fluctuations in tropospheric water vapor and (b) yielding accurate position data for satellite drag and neutral density determination. Possible ionospheric observations could be carried out either via radio links between either the satellite pair or each satellite and the ground station.

The application of bi-frequency radio beacon (BFRB) has resulted in fruitful achievements in ionospheric research, and encourages further application of this technique in space sciences. However, the ability of BFRB to detect multi-spatio-temporal structures in ionosphere, especially the small scale phenomena caused by nonlinear processes is quite limited. Hereby the Tri-Band Beacon (TBB) technique is suggested. The TBB is a three-frequency radio beacon to provide transmissions at VHF, UHF and L-band. Tomographic imaging of the ionosphere is a

recently developed technique that uses integrated measurements and computer reconstructions to determine electron densities. The integral of electron density along vertical or oblique paths is obtained by employing radio transmissions from LEO satellite transmitters to a chain of receivers on the Earth’s surface. Analyzing the total electron content (TEC) data using computerized ionospheric tomography (CIT) produces two-dimensional maps of the ionospheric plasma. Once the ionospheric effects on the radio wave propagation have been determined, the Doppler shifts of the UHF and VHF transmissions can be analyzed to give positioning of the LEO satellites to within a few meters. By measuring the effects of the atmospheric drag on the LEO satellites, global data for neutral densities in the upper atmosphere can be obtained. There is an additional phase delay of the VHF/UHF/L-bands from the neutral constituents of the troposphere. This phase delay can be used to provide measurements of integrated water vapor. The spatial distribution of water vapor density may be determined with high precision phase measurements from a linear array of ground receivers observing the L-band transmissions of the TBB.

The goals of the TBB are as follows:

- to measure the ionospheric total electron content (TEC) and derive the ionospheric electron density profiles by CIT technique;
- to investigate the ionospheric scintillation and irregularity;
- to measure the vapor content in the troposphere;
- to help in positioning of the satellite (orbit).

3.5.1. Ionosphere disturbance observation

The simplest model of TBB operation involves one ground station continuously recording the amplitudes of transmissions from the LEO satellite at 150, 400 and 1067 MHz. The outputs of phase detectors in the receiver are scaled to yield a continuous record of total electron content from horizon to zenith to horizon as the satellite beacon crosses over the ground station.

The TBB beacon transmissions can be observed by chains comprised of linear arrays of receivers. For tomographic measurements of the ionosphere using the TBB, similar linear arrays will have to be set up and aligned with the orbit of the LEO satellites

3.5.2. Radio Wave Scintillation Measurements

Scintillations are a major problem for radio systems using satellite to ground links near the magnetic equator and at the high-latitudes that include the polar cap and auroral regions. VHF communication links can be affected by scintillations at all times during the solar cycle, with the severity peaking near the period of solar maximum. At UHF

and the L-band, strong scintillations are encountered during the solar maximum period, especially near the magnetic equator and in the Asian sector.

Amplitude and phase scintillations are often associated with large gradients in TEC. At high latitudes, these gradients are associated with enhanced ionization density as in polar cap patches or auroral blobs. At low latitudes, these gradients are observed in plasma bubbles or “depletions” of plasma density. The Tri-Band Beacon experiment on LEO satellite will provide simultaneous measurements of TEC along with phase and amplitude scintillations at 150, 400 and 1067 MHz. To the first order approximation, the Tri-band Beacon will allow the determination of the frequency dependence of scintillation in weak and strongly turbulent structures near the magnetic equator. With simultaneous TEC determination, the distribution of scintillation causing irregularities with respect to the TEC structures will be determined.

3.5.3. Tropospheric Observations from near Perigee

The LEO satellite has the potential for similar observations using the low-Earth orbiting (LEO) TBB in the VHF, UHF and L-bands. If the water vapor measurements are performed with sufficient precision, they will be an inexpensive alternative to water vapor estimations from radiometers. Additionally, the geometry of the measurements will be well suited to the use of tomographic techniques to produce two-dimensional images of the water vapor along the orbital plane. Just as tomography has been used to image the ionosphere, a similar approach can be employed to provide two-dimensional maps of water vapor in the troposphere.

The refraction of radio waves by the neutral atmosphere (dry gases and water vapor) is independent of frequency, producing delays in the signal from the satellite to the receiving station. The troposphere is the lower part of the Earth’s atmosphere (up to about 20 km) and contains the bulk of the neutral atmosphere contributing to signal delay. Tropospheric delay has a hydrostatic component (dry gases) and a wet component (water vapor). The hydrostatic component is larger but far less variable and can be predicted from surface pressure measurements. The wet delay along a particular radio signal path is essentially a measure of the total amount of water vapor through which the signal passes.

Water vapor varies with geographic region and local weather conditions, contributing from 0 to a few cm of vertical radio delay in the dry polar regions and from 20 to 40 cm of vertical delay in wet equatorial regions. Slant paths at very low elevation angles pass through significantly larger amounts of water vapor than vertical paths. The slant paths can have wet delays that are a factor of five larger than that of a vertical path. So at a site with 20 cm of vertical wet delay, slant paths could be delayed by 1 m or so due to water vapor.

Double differencing of the Doppler data is used to reduce the effects of satellite orbit uncertainties and to remove errors due to satellite and receiver clock variability.

Ionospheric effects are removed by an improved dual-frequency correction algorithm which includes a model for higher order ionospheric terms. The hydrostatic delay term of the troposphere is modeled using surface pressure measurements. Since the path length term is well characterized, the only remaining terms are the tropospheric delays due to water vapor (or wet delay), multi-path, system noise, and residual errors in the other terms. The zenith wet delay at each station is estimated from the relative double differenced measurements using either a least squares inversion or a Kalman filtering approach. Using these techniques, zenith wet delay is obtained with an accuracy and precision better than 14 mm.

Table 3.2: Tri-Band Beacon Requirements

Observational Requirements		
Data Parameter	Observational Requirements	Comment
TBB phase measurement	<32 mm	Ground receiver @ 150 MHz
TBB sampling rate	> 50 Hz	Ground receiver
Science Requirements		
Data Parameter	Science Requirement	Comment
Water vapor profile	<1~10%	Double differencing of the Doppler data to remove errors
Electron density profile	<1~20%	Profile quality near the F2 peak can be worse elsewhere; Limited by horizontal gradients
TBB TEC	0.003 TECU	Relative TEC
	1~3 TECU	Absolute TEC
Scintillation TBB	n/a	>50 Hz SNR data
LEO Position	~100 cm	3-D rms position error
LEO velocity	<0.1mm/s	Relative velocity error for paired satellites

3.5.4. High Resolution Orbit Determination

Doppler measurements from ground based receivers of the TBB signals can provide precise orbits of each COSMIC satellite. The stability of the TBB is specified to be 1 part in 10^{12} which yields a displacement error of 20 cm in position. Other system errors for the LEO satellites, like un-modeled forces, residual fraction and antenna pattern are in the 1-m range. Tracking of satellites is accomplished by a number of techniques including (1) radar ranging, and (2) onboard Doppler beacon transmitter. Atmospheric drag is the predominant natural force that affects the LEO satellite orbits, especially when the satellites are near their injection altitude of 400 km. The orbit data obtained using the TBB Doppler position technique can be analyzed to yield the drag acceleration. The orbit determination using the TBB for Doppler ranging can provide a scientific data source for a global map of these fluctuations.

4. Scientific Payload

4.1. Scientific payload on KuaFu-A

4.1.1. Extreme/Far UV Disk Imager Package (EDI)

4.1.1.1. Overview

The extreme ultraviolet (EUV) and far ultraviolet (FUV) imaging telescopes onboard KuaFu-A are being designed to enhance our understanding of solar activity. Dynamical processes at the Sun impact Earth and human activities. Near-real-time prediction capabilities are needed to quantify the effects of Space Weather. These capabilities will evolve from a better understanding of solar and heliospheric physics, in conjunction with adequate solar observations.

Our EUV/FUV package on KuaFu-A will fill the gap between the SWAP/-PROBA2, SECCHI/STEREO, AIA/SDO era (between 2006 and 2011) and the forthcoming Solar Orbiter mission, which is presently expected to start scientific operations not earlier than 2017, after a cruise phase of several years.

To study solar eruptive events at the source of its origination, we have to observe the corona in a very wide range of temperature regimes. Therefore the coronal imaging suite will comprise two telescopes for the study of the base of the hot solar corona. An extreme ultraviolet (EUV) telescope to observe the hot, upper coronal structures, and a far ultraviolet (FUV) telescope (at the hydrogen Lyman- α wavelength) to image the base of the lower corona.

Two filtergraph telescopes will compose the EUV/FUV Imager package. The two telescopes will produce quasi-monochromatic images of the solar corona in a field of view with a minimal extent of 45 arcmin around Sun center. These images will be recorded on 2-D detectors with cameras, providing a resolution of about 2.6 seconds of arc squared per pixel, or less.

Both telescopes will share a similar optical scheme, each being tuned according to its aperture size. The optical design is based on an off-axis Ritchey-Chrétien system, with two off-axis mirrors. Each channel will have a set of specific filters, aiming at rejecting the visible and infrared (IR) part of the solar spectrum, and to define a narrow band pass centered on the wavelength of interest.

There is an important flight heritage with this concept of EUV telescopes:

SOHO/EIT, phase-A of AIA/SDO¹, PROBA-2/SWAP, and forthcoming projects with Solar Orbiter. The Lyman- α instrument has flight heritage from the TRC² (R. Bonnet et al, 1980) camera.

4.1.1.2. EUV filtergraph telescope

General design

The design of the EUV telescope is based on a 2-mirror off-axis telescope³, derived from the SOHO/EIT⁴ instrument and currently developed for the PROBA-2/SWAP⁵ telescope. Compared to classical centered solutions, this design (see Fig. 4.1) offers the advantages of smaller filters, lighter mirrors, and absence of an external baffle.

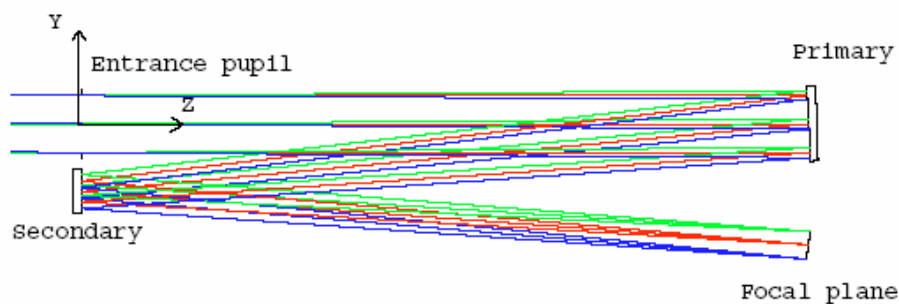


Fig. 4.1: Optical scheme of the EUV filtergraph.

Table 4.1: EUV channel parameters (will be updated depending on final detector choice)

¹ MAGRITTE: an instrument suite for the Solar Atmospheric Imaging Assembly (AIA) aboard the Solar Dynamics Observatory (SDO), P. Rochus, J.M. Defise et al, SPIE 5171, 2003

² High-resolution Lyman- α filtergrams of the Sun, R. Bonnet et al., Astr. J. 237:L47-L50

³ SWAP: Sun watcher with a new EUV telescope on a technology demonstration platform, J.M. Defise et al., ICSO Conference 2004

⁴ EIT: Extreme-UV Imaging Telescope for the SOHO mission. J.P. Delaboudiniere et al., Solar Physics 162, 291-312, 1995

⁵ PROBA-II Payload: A Belgian Mini Space Weather Observatory, P. Rochus, J.M. Defise et al., IAF Conference Proceedings 2004

Field of view:	≥45 arcmin square
Spectral wavelength:	19.5 nm central wavelength (1 nm FWHM bandpass)
Total length	~ 600 mm
Max width x height	~ 180 mm x 150 mm
Entrance pupil:	33 mm diameter
Focal length:	1200 mm
Detector	CMOS APS with scintillator coating Candidate: STAR1000 from FillFactory or successors under development

The two mirrors are mounted on a planar optical bench that will provide the adequate stability and fixations for two internal planar baffles. The bench itself will be connected to the S/C platform with flexible legs, avoiding stress disturbances from platform deformations.

The EUV/FUV wavelength range requires the use of super-polished mirrors in order to reduce the scattering of light from optical surfaces and to reach the adequate image quality. This will be achieved with super-polishing of mirror substrates, a technique which has already been used in previous space programs.

Filters and coatings

In the EUV spectral range, the spectral selection is achieved with two transmission foil filters and specific coatings deposited on the mirrors. The foil filters are made of a thin aluminium foil (150 nm thick), used to reflect the visible and IR part of the solar spectrum outside the instrument, allowing the EUV flux (17 to 50 nm) to be transmitted. The mirrors are coated with EUV multilayers, made of periodic stack (20 to 30 stacks) of bi-layers optimized to provide reflectivity (in quasi-normal incidence) and accurate spectral selection with bandwidth of the order of 1.5 nm FWHM. The combination of the two filters and the two reflections on the multilayer mirrors will provide a very narrow band pass centred at the wavelength of the spectral line of interest.

The required cleanliness of the optical components and the need for protection of the filters require an aperture door on the front section of the instrument. It is the only mechanism to be implemented in the instrument, except if an image stabilization system is needed.

Detector

The images are recorded by a camera based on an active pixel sensor (APS) detector. The present baseline can be the use of a CMOS/APS of the STAR1000 series (Fillfactory, B), covered with a scintillator coating in order to provide sensitivity in the

EUV range. This detector does not require the use of a shutter, and allows also non-destructive readout. This feature can be very useful to fully exploit instrument for solar corona imaging. Other possibilities currently under development can be used, such as backside-illuminated thinned CMOS detectors.

The detector needs to be operated at low temperature (below -30°C) in order to reduce the thermal noise. This will be achieved with a classical implementation of a cold finger connected to an external radiator viewing cold space.

Pointing stabilization

If the pointing stability of the spacecraft is not sufficient (typically pointing jitter > 5 arcsec over a 10 s period), an active image stabilization system will be implemented. It consists in a piezoelectric transducers (PZT) mechanism mounted at the back of the secondary mirror mount. The PZTs are driven by the signal of an additional sensor, a guide telescope. The guide telescope is a simple lens system connected to a 4-quadrant detector. It will provide the Sun pointing offset of the platform at a cadence of ~ 100 Hz. The guide telescope has to be mounted in the close vicinity or on the EUV/FUV telescope assembly. The PZT system will compensate the spacecraft jitter with an active tilting of the secondary mirror over two rotational axes during the exposure time.

Overall implementation

The EUV filtergraph telescope can be implemented as shown in Fig. 4.2.

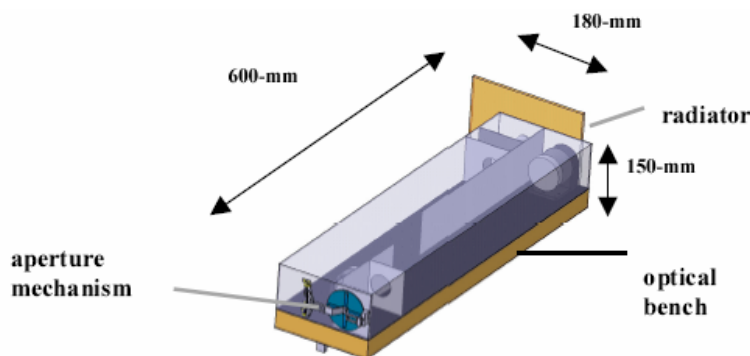


Fig. 4.2: EUV Instrument concept.

4.1.1.3. Lyman- α filtergraph telescope

General design

The far ultraviolet (FUV) channel at the hydrogen Lyman- α wavelength 121.6 nm

is using a very similar design as the EUV filtergraph. Because the diffraction becomes more important with increasing wavelength, the FUV channel requires the use of a larger aperture diameter limiting the spatial resolution of the telescope. Therefore, the design requires an aperture of 60 mm, which will consequently enlarge the dimensions of the telescope. Larger optics will also require larger off-axis angles.

Coatings

The optical mirrors of the FUV telescope will use reflective coatings of aluminium with MgF_2 protective layers. These coatings are standard technology providing reflectivity of more than 80% in the Lyman- α wavelength range. This is making the instrument extremely efficient at the strongest solar emission line.

Filters

The Lyman- α filtergraph will consist of an interference filter on MgF_2 substrate to isolate the spectral line at 121.5 nm. The narrow-band interference filter will be used at the entrance of the telescope, where it rejects EUV and X-rays and protects the secondary mirror coating by rejection of visible light by a factor of 10^4 . Acton Research Corporation (ARC) is fully capable of producing such a filter to specification. To achieve the required spectral purity, a solar-blind detector will be used to suppress the residual continuum radiation passing through the filter. The combination of these yields a spectral purity of >90% for the Lyman- α line emission versus background/continuum radiation in quiet and active areas of the solar disk of the Sun.

Detector

Given that standard silicon detectors are not sensitive at 121 nm; the detector can be identical to the EUV detector, i.e. a CMOS APS with a scintillator coating. The high sensitivity of these devices to visible light makes it necessary to use an additional Lyman- α filter near the focal plane. Another alternative that can be considered is include the use of an image intensifier instead of the filter. This intensifier, based on microchannel plates (MCP) makes the sensor more sensitive in the FUV and at the same time guarantees solar-blindness at wavelengths longer than 160 nm. This technology has already flight heritage and such detectors are now commercially available. The intensifier is made of a microchannel plate stack with an anode consisting of a fiber-optic block with scintillator coating. Light is detected by an active pixel array sensor similar to the one used by the EUV filtergraph. The front sides of the microchannel plates (photocathode) are coated with KBr, and the unit will be sealed by a MgF_2 window which provides a short wavelength cutoff below Lyman- α .

Table 4.2: FUV channel parameters

Field of view:	≥45 arcmin square
Spectral wavelength:	121.5 nm central wavelength
Total length	~ 600 mm
Max width X Height	~ 300 mm x 200 mm
Entrance pupil:	60 mm diameter
Focal length:	1200 mm
Detector	CMOS APS with scintillator coating or other alternatives

4.1.1.4. Electronics

Each of the EUV/FUV channels will include its own proximity electronics used to drive and read the detector. A local memory buffer will be included. This local electronics will be implemented in the focal plane assemblies. In order to optimize the electronics development, the two units will use similar readout electronics and focal plane assemblies. They will be connected to a single common electronic box. This box will provide the power supply with adequate voltages to the two focal planes, and will ensure the communication of the data to the platform.

If required due to potential lack of pointing stability, the guide telescope will be connected to the common electronics box that will drive the PZT mechanisms of each filtergraph. The functionalities of the electronics box will need to be agreed according to the capabilities of the central computer of the platform. Image compression will be extensively used for the two EUV/FUV imagers. Compression factors ranging from 3 to 50 can be accommodated, depending on the computing resources available in the electronics box or in the platform central onboard computer.

4.1.1.5. Open parameters

Several parameters can be still be adjusted according to the overall needs of the payload instruments and common science goals, the platform capabilities and the available detector technologies:

- FOV extension (> 45 arcmin)
- EUV channel band pass: (19.5 nm or wider band pass at 17.4 nm)
- Need for image stabilization system to compensate for platform jitter
- Detector type (and size of pixels)
- Accommodation of the two imagers and the GT in a single structure

4.1.1.6. Payload resources

The estimated resources are detailed in Table 4.3. These values are preliminary estimates that will need to be adjusted according to the final design options that will be selected.

An example of instrument accommodation in a common structure is shown in Fig. 4.3.

Table 4.3: EUV/FUV Imager Package (mass and volume will be updated after a first design phase)

Mass (2 filtergraphs + 1 GT + 1 electronics box)	25 kg
Dimensions	
EUV Imager	600 x 180 x 150
Lyman- α imager	600 x 300 x 200
Guide Telescope	600 x 120 x 120
Power	20 W
Data rate	100 kbps

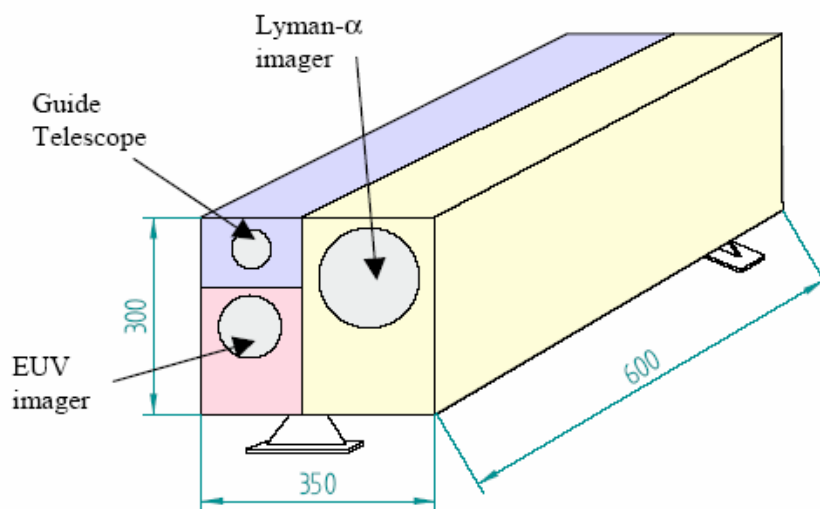


Fig. 4.3: Possible accommodation of the two EUV/FUV units with their Guide Telescope. The (separate) electronics box is not shown.

4.1.2. White Light Coronagraph (Ku-Cor)

4.1.2.1. Instrument technical description

The design of the KuaFu-A coronagraph “Ku-Cor” is based on externally occulted coronagraphs built for recent past missions, essentially the LASCO C2 and C3 instruments and the yet to be flown SECCHI COR 2 of the STEREO mission, which is itself a combination of the C2 and C3 instruments. Ku-Cor will adopt the approach of a single instrument having a large field of view extending from 2.5 to 15 solar radii and a pixel scale of 14 arcsec but will incorporate specific adjustment systems which have been successfully implemented on LASCO-C2 and allow one to obtain images of unsurpassed quality. The table below summarizes the main characteristics of the proposed Ku-Cor.

Table 4.4: Main optical parameters of Ku-Cor

Field of view	2.5-15 R_{\odot}
Spatial scale	14 arcsec/pixel
Focal Plane Array	2048 × 2048
Band pass	650-750 nm
Exposure times	3 s for B 3 × 10s for pB
Maximum cadence	22 s
Aperture	Ø 30 mm
Effective Focal Length	200 mm
Stray light / Disk light rejection	10^{-11} B_{\odot}
Pixel size	13.5 × 13.5 μm^2

4.1.2.2. Proposed optical design

The optical design of the proposed coronagraph is an externally occulted, all-refractive Lyot coronagraph working in visible light as is shown in Fig. 4.4. All lenses have spherical surfaces thus allowing optimum superpolishing, in particular for the front optical element, to minimize instrumental stray light. The total length of this instrument is of the order of 1200 mm, and its cross section is about 160 × 160 mm.

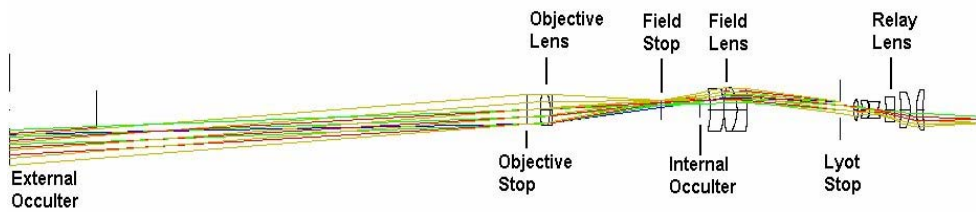


Fig. 4.4: The optical layout of the proposed Ku-Cor coronagraph

The table below summarizes the key components of the coronagraph and specifies the heritage, either LASCO C2 or SECCHI COR 2.

Table 4.5: Choice of the adopted solutions for some critical items of the Ku-Cor coronagraph

Subsystem	Select	Comment
Optical concept	COR2	FOV vs. spatial resolution
Door	COR2-C2	Similar designs
External occulter + tube aperture	C2	Simpler design – Superior performance
Objective lens (O1)	C2	Doublet in optical contact-AR Coated
IOCS	C2	Not available on COR2
Shutter	COR2	Placed in front of O3 (pupil)
Lyot Spot	C2	Deposited on the O3 front surface
Polarizer assembly	COR2	Rotating polarizer
Structure	C2	Rectangular

The external occulter derived from LASCO C2 is a truncated cone which gives superior performances while being extremely simple. The selection of the objective lens (O1) is a very critical issue. We adopt the LASCO C2 solution in which O1 is a simple doublet with the two AR coated lenses being in contact by “molecular bond”. The internal occulter centering system (IOCS) allows the displacement of the internal occulter and thus centering it with respect to the Sun center direction. This mechanism had been extremely useful on LASCO C2, because it permits to compensate some minor misalignment observed in the instrument after launch. The shutter will be placed in front of the O3 objective where there is an image of the entrance pupil. The Lyot spot will be deposited directly on the first lens of O3 to block the ghost images created by the O1 objective lens. The polarizer assembly consists of a rotating achromatic polarizer in Polarcor. This solution has the advantage of easy access to all the optical components, which greatly improves the mounting of all the subsystems and their alignment. The FPA is based on a commercially available $2k \times 2k$ CCD detector which needs to be cooled to about -70 degrees and be protected, along with its proximity electronics, from

space radiation with proper shielding. The table at the page hereafter summarizes the different components of the proposed KuaFu-A coronagraph.

Table 4.6: CU-KOR main components

Sub-Systems	Remarks
Structure	
Coronagraph Optical Bench (COB)	Rectangular section
Motorized isostatic legs	For S/C fixation.
Optics Components	
Objective Field, Relay Lenses	O1, O2, O3
Rejection Mirror	A1
Field and Lyot Stops	A1, A2, A3, A4
Optical Baffles	Vanes
Polarizer	Polarcor
Filter	650-750 nm
External Occultor	
Internal Occultor	
IO focusing lens	
Mechanisms	
Door mechanism	
Internal Occultor mechanism	Adjustable mechanism
Polarizer mechanism	Hollow-core Motor + Polarcor
O2 focusing lens adjustable mech.	
Shutter Mechanism	
Focal Plane Assembly (FPA) & CCD	
CCD + proximity electronics	
CCD Holder	
FPA thermal control	Cold finger; passive radiator
Data processing unit (DPU)	Instrument control and data handling
Thermal control	
Thermal regulation	Heaters, thermal sensors, harness, dedicated software
Electrical	
E-Box (1)	
Internal harness	CCD-CEB, mechanisms cables; connectors plate

4.1.2.3. Structure

The structure of the instrument will be an openable rectangular box in aluminium. This solution has the advantage of easy access to all optical components, which greatly improves the mounting of all subsystems, their alignment and the access for cleaning. The total length of this instrument is of the order of 1200 mm, and its cross section is about $160 \times 160 \text{ mm}^2$. A possibility of a folded configuration could be investigated, with a reduced length of the instrument but with a width which is twice the nominal width. The folded configuration implies to insert two adjustable folding flat mirrors in the optical path.

4.1.2.4. Mechanisms

There are five mechanisms:

- The front door mechanism (FdM). It must be a dust seal in order to avoid the dust contamination during the operation on ground.
- The Internal Occultor Centering System (IOCS). It permits to adjust, in flight, the location of the inner occultor on the external occultor image given by O1.
- The refocusing mechanism (RM), for fine tuning the focus in flight, by adjustment of the O2 location.
- The shutter.
- The polarizer assembly is driven by a hollow core motor.

4.1.2.5. Alignment and pointing

It is required that the coronagraph be pointed to the center of the Sun with an absolute accuracy of 45 arcsec. This requires co-alignment with the other Sun-pointed instruments and with the Sun tracker at an accuracy which will be difficult to achieve during assembly and integration on the ground and moreover to maintain on orbit, after zero-g release and thermo-elastic stabilization. We are therefore recommending the approach successfully implemented on SOHO/LASCO, i.e., “motorized legs” which allow the in-flight fine pointing of the instrument (the absolute criterion is to perfectly balance the diffraction fringe surrounding the occultor). This is an open-loop system which will be used initially for instrument set-up and later occasionally in case of drift. We also recommend to associate a boresighter (or guide telescope) to be used as an external reference for the optical axis of the instrument and for initial pointing. It is a very simple telescope system consisting of a doublet lens and a 4-quadrant detector.

The required pointing stability is 3 arcsec over 30 s and is driven by the polarization sequence. This requirement must be achieved by the satellite as a

coronagraph does not offer simple pointing capability. Indeed a separate pointing platform would be very heavy and cumbersome to implement.

4.1.2.6. Electronic Box

The KU-COR Electronics Box will contain four functional modules:

- Data Processing Unit (DPU), consisting of the digital signal processor board (DSP), extension board (EXT) with spacecraft interface specific circuits, the mass memory board (MMB), and the DPU interface board (DIB) with instrument interface specific electronics
- Mechanism controller board (MCB), including FPGA based controllers (for polarizer mechanism, internal occulter centring system, refocusing mechanism and entrance door) and a H/K subsystem for position encoding, temperature data acquisition and thermal regulation
- Power converter module (PCM), containing DC/DC switching converters, over current protection, EMI filters, latch and solid state relays for power distribution control, and a PCM H/K subsystem for voltage, current and temperature data acquisition, CCD Read out Board and a CCD housekeeping board

All the modules are integrated in an aluminum box that interfaces with the spacecraft structure. The distance between the E-box and the detector should not exceed one meter.

4.1.2.7. Resources

Dimensions

The external dimensions of the coronagraph optical bench are 1200 mm x 160 mm × 160 mm in the nominal non-folded configuration.

Mass

The mass evaluation is given in the table hereafter

Table 4.7: Mass evaluation

Element	Mass (g)
Coronagraph assembly	21550
E-Box	10000
Motorized isostatic legs	3600
TOTAL	35150

Power consumption evaluation

✓ Operational mode

The power requirement evaluation is given in the table hereafter (all in Watt)

Table 4.8

Mode	A	B
E-Box		
DPU	7	
MCB	1	
PCM	2	
CRB	1	
Secondary power	11	
Primary power E-Box ($\eta=0,7$)	15,7	
Power Dissipation of the E-Box	15,7	
Mechanism/ lamps		
Front Door Mechanism		7
IOCS		7
Refocusing mechanism		7
Shutter		10
Polarizer mechanism		7
Stimuli		2
Calibration lamps		2
Motorized Isostatic legs		10
Thermal Regulation		
Operational	20	20
Primary power for KU-COR	35,7	

Column A: No mechanism movement, CCD operational

Column B: Gives the power consumption for every mechanism/lamp. Only one device is operated at a time. Typical duration is a few seconds, excepted stimuli and calibration lamps.

✓ Non-operational mode

The non-operational power consumption dedicated by the thermal regulation is estimated at 15 W. It allows structure and CCD to remain in non-op temperature conditions.

The CCD annealing needs a heater power of 25W. This operation could take typically 40 h.

4.1.3. Lyman- α Coronagraph (Ly-Cor)

4.1.3.1. Instrument description

A classical, internally-occulted Lyot coronagraph is required so as to preserve the image quality down to the inner limit of the field of view (note that this is not the case in externally-occulted coronagraphs since the external occulter degrades the point spread function). An all-reflective optical system is further required to operate in the ultraviolet. So altogether, the optical design follows the general concept of a Lyot coronagraph but adapted to a solution with mirrors rather than lenses. The most basic solution requires 5 mirrors to carry out the various steps of stray light rejection in a coronagraph. This solution presents two disadvantages. First it requires that the first mirror M1 be parabolic a shape which does not allow to reach an ultimate super polished finish. Second, it imposes that the detector be near the entrance pupil, i.e., towards the Sun thus complicating its cooling. We favor a solution with 6 mirrors (see Fig. 4.5) which alleviates both difficulties and further makes the instrument very compact.

Table 4.9: Main optical parameters

Field of view	1.15 -2.7 R_{\odot}
Spatial scale	2.5 arcsec/pixel
Focal Plane Array	2048 \times 2048
Bandpass	Few Angstroem centered on 121.6 nm
Exposure times	TBD
Maximum cadence	1.5 images/minute
Aperture	\varnothing 30 mm
Effective Focal Length	1100 mm
Stray light / Disk light rejection	$2.5 \cdot 10^{-6}$ at 1.5 R_{\odot}
Pixel size	TBD

4.1.3.2. Proposed optical design

The entrance aperture A0 (30mm diameter) allows the full Sun and the corona to illuminate the off-axis spherical mirror M1 (400mm focal length). M1 is mounted on a two-axis gimbal system allowing its fine pointing.

M1 is highly superpolished to a roughness of 0.04 nm (RMS) to minimize the stray light scattered in the instrument. Monocrystal silicon will be the baseline and prototypes have already been manufactured.

A real image of both the Sun and the corona is formed onto a flat mirror M2 which acts as a field mirror. The solar disk image passes through a hole (equivalent radius 1.15

R_{\odot}) at the center of this mirror and is used to detect and correct pointing errors via a close loop control system by acting on the actuators located behind the M1 mirror.

The M3 mirror is identical to M1 and altogether with M4, form an afocal system fully corrected for Seidel aberrations. The Lyot stop which blocks the diffraction from the M1 mirror, is placed between M4 and M5, together with the narrow band filter centered on the Lyman-alpha line. The system M5+M6 finally images the corona on the detector.

Spectral purity is mandatory and will be achieved by:

- i) Mo/Si multilayers coating of the mirrors,
- ii) a solar-blind detector,
- iii) the aforementioned narrow band filter.

The detector will be composed of an intensifier (MCP with a solar-blind photocathode) fiber optically coupled to a CMOS detector, such as in development at MPS (Lindau).

The figure here after gives the optical design of the Lyman α coronagraph.

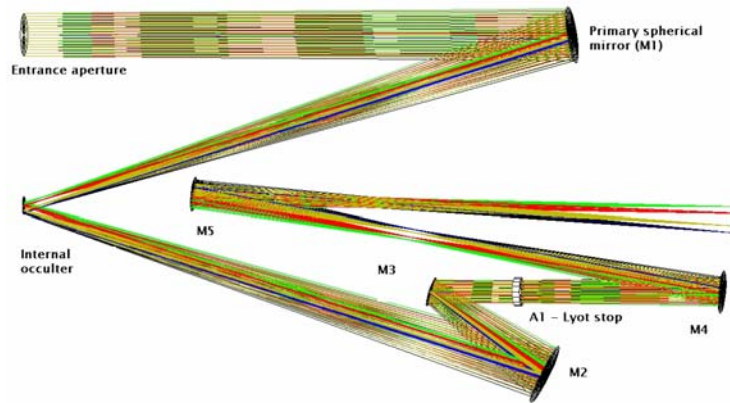


Fig. 4.5: The optical layout of the proposed lyman α coronagraph

Table 4.10: Lyman α coronagraph main components

Sub-Systems	Remarks
Structure	
Coronagraph Optical Bench (COB)	Rectangular section
Optics Components	
Optical Baffles	Vanes
Coronagraphic part	M1, internal occulter mirror
Collimation part	M2, M3
Field and Lyot Stops	A1, Lyot stop
Re imaging part (Gregorian telescope)	M4,M5

Filter	Narrow band interference
Mechanisms	
Door mechanism	
M1 cover	Protective cover against the contamination
Coronagraph Pointing system	M1 pointing adjustment
Pointing Control System	Electronic device
Focal Plane Assy (FPA)	
MCP image intensifier fiber coupled to a CMOS detector	Solar blind photocathode
FPA Holder	
FPA thermal control	Cold finger; passive radiator
Detector electronics	Detector proximity electronics and data formatting.
Thermal	
Thermal regulation	Heaters, thermal sensors, harness, dedicated software
Internal Check in flight	
Optical device	To check the status of the instrument in flight
Electrical	
E-Box	
Internal harness	CCD-CEB, mechanisms cables; connectors plate

4.1.3.3. Structure

The structure of the instrument will be a parallelepipedic box in aluminium equipped with a cover. This solution has the advantage of easy access to all the optical components, which greatly improves the mounting of all the subsystems, their alignment and the access for the cleaning. The **Lyman-alpha Coronagraph (LyCo)** will be mechanically coupled to the **Visible Coronagraph (ViCo)**. And the boresight of the two instruments will be parallel within 10 arcsec.

The total length of this instrument is of the order of 620 mm, and its section is about 320 x100 mm. A possibility of a folded configuration could be investigated, in order to get a more compact and stiffer structure.

4.1.3.4. Mechanisms

There are five mechanisms:

- The front door mechanism (FdM). It must be dust seal in order to avoid the dust contamination during the operation on ground and designed in such a way to avoid the dust production during vibrations.
- The M1 mirror being very sensitive to the contamination, a motorized multi-shots cover is provided to protect the component
- The pointing system located behind the M1 mirror
- The pointing control system (PCS), which is in fact an electronic device located behind the internal occulter mirror (M2), used to identify the alignment errors and to control the alignment correction operation carried out, thanks to an open loop, with the M1 mirror.
- The refocusing mechanism

4.1.3.5. Alignment and pointing

As far as the visible coronagraph is the most demanding instrument versus the pointing requirement it must be co-aligned with accuracy with respect to the sun tracker. The LyCO will be mechanically attached on the ViCo instrument and their boresights will be accurately aligned within 10 arcsec during the integration at instrument level. It is reminded that M1 mirror of LyCO is equipped with some adjustment device allowing re-adjusting and fine tuning the co-alignment of the instrument in flight.

During the integration operation at satellite level, the coronagraphs must be co-aligned with the sun tracker and all the other sun pointed instrument have to be co-aligned with the coronagraphs.

Two solutions can be envisaged to integrate the instruments on the satellite.

1. As proposed in the Document "KU-COR a coronagraph for the KUAFU mission" ref LAM.PJT.COR.NOT.050221_01, the ViCo is attached onto the platform by means of motorized legs that allows correcting, in flight, the default induced by the “zero g” release and the thermo-elastic stabilization. This approach was implemented with success on the SOHO satellite with the instrument LASCO. There is an open loop system which will be used initially for instrument set-up and later occasionally in case of drift. We also recommend to associate a boresighter (or guide telescope) to be used as an external reference for the optical axis of the instrument and for initial pointing. It is a very simple system consisting of a doublet lens and a 4-quadrant detector. With this solution the coronagraphs and the sun tracker could be perfectly co-aligned in flight but the mass of the motorized legs, which has been evaluated at 3.6 kg, has to be considered.
2. The second solution consists in mounting directly the ViCo on the satellite and to co-align it with respect to the sun tracker. All the sun pointed instruments will be co-aligned with the coronagraphs. The “zero g” release and the thermo-elastic stabilization in flight will obviously lead to a misalignment between the

coronagraphs and the sun tracker and the offset will always have to be taken into account during the satellite pointing operations. The offset value will be defined by ViCo and send to the satellite which will have to correct the pointing direction accordingly. Of course, the pointing direction of all the other sun pointed instrument will move the same way.

4.1.3.6. Electronic Box

The Device, common to the two coronagraphs, will contain four functional modules:

- Data Processing Unit (DPU) , consisting of the digital signal processor board (DSP), extension board (EXT) with spacecraft interface specific circuits, the mass memory board (MMB), and the DPU interface board (DIB) with instrument interface specific electronics
- Mechanism controller board (MCB), including FPGA based controllers used to control all the mechanism of the visible instrument VICO and the mechanisms of LyCO listed at paragraph 2.3 of this document, and the thermal regulation.
- Power converter module (PCM), containing DC/DC switching converters, over current protection, EMI filters, latch and solid state relays for power distribution control, and a PCM H/K subsystem for voltage, current and temperature data acquisition, CCD Read out Board and a CCD housekeeping board.

All the modules are integrated in an aluminum box which protects them against radiations and is in interface with the satellite. The distance between the e-box and the detectors should not exceed one meter.

4.1.3.7. Resources

Dimensions

The external dimensions of the Lyman Coronagraph optical bench are 620 mm x 320 mm x 100 mm in the nominal non folded configuration.

Mass

The mass evaluation is given in the table hereafter

Table 4.11: Mass evaluation

Element	Mass (kg) Including margin
Lyman Coronagraph Ass'y	20.0
Contribution to E-Box (1) +	3.5

harness	
TOTAL	23.5

(1) the mass given here in corresponds to the extra-mass of the electronic and external harness that will be necessary to add to the mass already estimated for the ViCo coronagraph.

Power consumption evaluation

✓ Operational mode

The power requirement evaluation is given in the table hereafter.

Table 4.12

Mode	A	B
E-Box		
DPU	7	
MCB	1	
PCM	2	
CRB	1	
Secondary power	11	
Primary power E-Box ($\eta=0,7$)	15,7	
Power Dissipation of the E-Box	15,7	
Mechanism/ lamps		
Front Door Mechanism		7
M1 Cover mechanism		7
Pointing control system	2	
M1 pointing adjustment mechanism (2 motors)		7
Refocusing mechanism		7
Stimuli		2
Check in flight device		2
Thermal Regulation		
Operational	20	
Primary power for LyCO	37,7	

Column A : No mechanism movement, CCD and thermal regulation operational

Column B : Gives the power consumption for every mechanism/lamps. Only one device is operated at once. Typical duration is a few seconds, excepted stimuli.

✓ **Non Operational mode**

The Non Operational power consumption dedicated at the thermal regulation is estimated at 10 W (TBC). It allows structure and CCD to remain in non-op temperature conditions.

The CCD annealing could be operated thanks to a heater of 25 W (TBC). This operation could take typically 40h.

4.1.4. KuaFu radio and plasma wave instrument (FengBo)

4.1.4.1. Overview

The FengBo instrument comprises an antenna system consisting of three orthogonal rigid booms allowing for direction finding measurement (3-D localization of the source region in the interplanetary space). Also shown on Figure 4.6 is the sensitivity level determined by the preamplifier noise.

As shown in Figure 4.6, the low-frequency part of the range will give access to in-situ wave phenomena, including those associated with the passage of interplanetary shocks, CMEs, CIRs, etc. For instance, when the dense material of a CME crosses the spacecraft, valuable information will be derived on the wave activity, the local plasma electron density, and other parameters.

The same receivers can be used to analyze the different types of waves detected by different sensors, for instance electric antennas and magnetic coils. Most main space programs, either in solar terrestrial physics or planetary physics, include an integrated radio and plasma wave package, and there is a lot of knowledge in the design of the sensors and receivers, as well as in the analysis techniques. In addition, all aspects of electromagnetic cleanliness are well understood and no longer a problem for modern spacecraft designs (e.g., ULYSSES, Wind/Waves, CASSINI, IMAGE, CLUSTER).

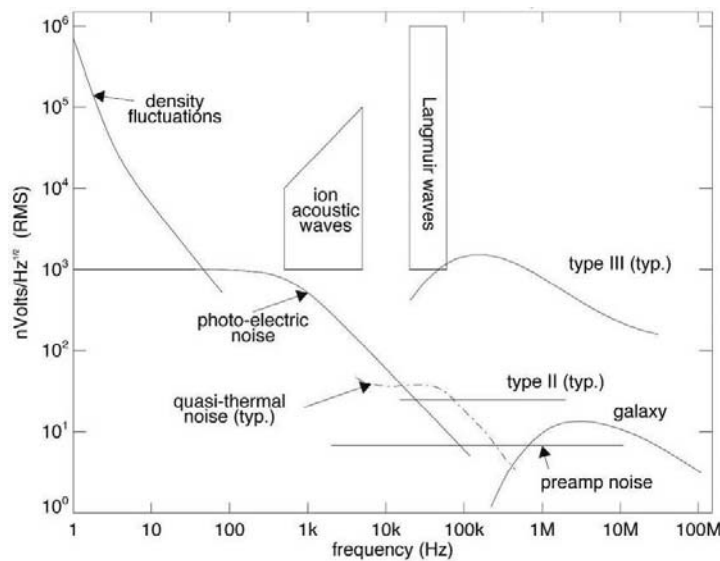


Fig. 4.6 The range of phenomena accessible using the radio technique and sensitivity level determined by the preamplifier noise

4.1.4.2. Instrument concept and heritage

The instrument is designed to observe energetic phenomena in the solar wind between the Sun and the Earth.

Different designs are used on many space missions and have a lot of heritage since the birth of space radio astronomy at long wavelengths. The KuaFu-A/FengBo instrument will inherit directly from the Cassini and the STEREO radio instruments. The main reason is that they are conceived for a three-axis stabilized spacecraft on which optical imaging is critical. Indeed, radio-wave measurements require antenna booms for which two limitations have to be considered: (i) influence on spacecraft stability; (ii) field of view of optical instruments and other wide-angle sensors. For KuaFu-A, the design will be similar to STEREO, on which the antennas are mounted on the side opposite to the Sun. Figure 4.7 shows the antenna mounting on one of the STEREO spacecraft.

The receiver system will be inherited from a long line of successful radio instruments on a large variety of missions (RAE, ISEE-3/ICE, ULYSSES, WIND, CASSINI, CLUSTER and STEREO). The particular FengBo design will directly derive from the STEREO design (our two STEREO instruments are in the process of tests and integration for a launch early next year). However, it will be simplified, since the KuaFu-A science objectives do not require a wave form analyzer. The FengBo design will also benefit from our current studies for the BepiColombo mission to planet Mercury, on which a similar equipment is being defined (This instrument will be part of the Radio and Plasma Wave package on the MMO, part of the JAXA support to the ESA mission). For this contribution, there is an on-going R&D program, supported by CNES, to miniaturize the receivers and gain significantly in mass and power.

Very good progress is being achieved on this miniaturization, and there is good hope to switch to this technology for BepiColombo, as well as any other future instrument (e.g., Solar Orbiter, Solar Probe, etc., and KuaFu-A/FengBo).

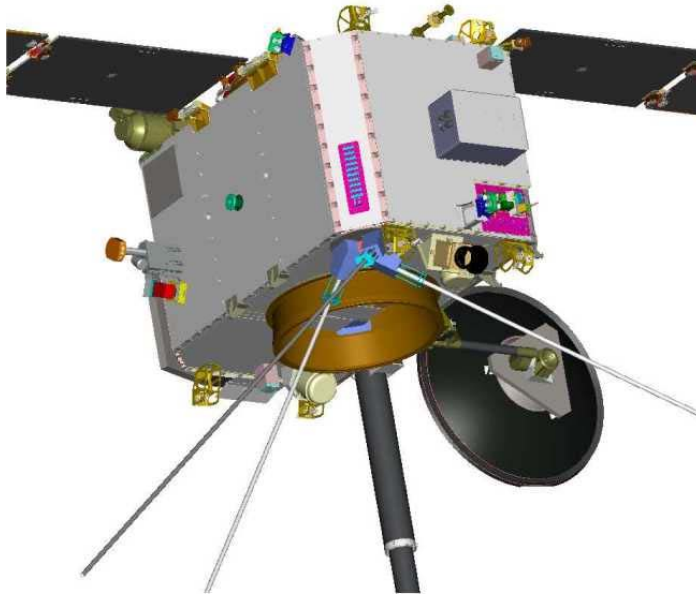


Fig 4.7: STEREO spacecraft : View of the back side (opposite to the Sun) of one of the two STEREO spacecraft, showing the antenna mounting. Antennas are not shown to full length on this figure. The large boom (not shown to full length) carries the magnetometer and other particle instruments.

The receiver will use the state-of-the-art techniques and will consist of the following sub systems:

Low Frequency Receiver (LFR)

- 1 channel, 2 bands (160 kHz-40 kHz), (40 kHz-10 kHz)

High Frequency Receiver (HFR)

- 2 channels, 125 kHz to 16.025 MHz in 319 steps of 50 kHz

The Digital Processing Unit will command the different subsystems and interface with the spacecraft. The DPU can also interface with other instruments on board the spacecraft, particularly the Energetic Particle Detector, to allow for special modes to be used in real time.

4.1.4.3. Instrument resources

Instrument resources are summarized below.

Mass: 11 to 12 kg (total)

Breakdown:

Main electronics: 3.5 to 4.5 kg (depending on capabilities)

(this includes receivers, DPU, Power Converter, Body)

Antenna assembly: 7 kg

(this includes mounting and deployment mechanism)

External harnessing: 0.5 kg

Power: 10 W

Bit rate: 2 to 4 kbps (depending on objectives and capabilities)

Box size: about 5 modules A4: significantly smaller when the new technology is used.

4.1.4.4. Special requirements: Electro-Magnetic Cleanliness

Many of the scientific objectives of the Radio wave observations on KuaFu-A are based on the measurement of low-level signals for which maximum sensitivity is required. Several inexpensive measures must be taken at the spacecraft and project level to ensure that the KuaFu-A spacecraft is clean from the point of view of both conducted and radiated electromagnetic interference. The sensitivity of the FengBo instrument will be approximately 2×10^{-9} V/(m $\sqrt{\text{Hz}}$) in the frequency range of 1 kHz to 16 MHz. Although these sensitivities may appear to require an excessively "clean" spacecraft, they are not difficult to achieve if good EMC practices are incorporated in the spacecraft design. Among others, the Cassini and Image spacecraft give recent testimony to this fact.

It is important to realize that an EMC-clean spacecraft is beneficial for every instrument, as well as for spacecraft systems. Given the progress made in understanding the principles, these EMC controls are easy to implement and do not require extensive or expensive testing. The FengBo team will encourage the KuaFu-A Project to set up a consultant EMC board to study the general grounding and shielding philosophies, instrument-particular exceptions/waivers, and test procedures for the mission. This committee would define an inexpensive, coherent scheme for minimizing interference. For example, a single point or "star" ground has often been suggested as the path to a clean spacecraft. This can be a burdensome requirement on many types of measurements and has been shown not to be very effective at high frequencies. Instead of such arbitrary rules, the EMC committee would work to find acceptable compromises using a "best engineering practices" point of view. Many of the interests of an EMC committee will overlap with other spacecraft cleanliness issues such as magnetic cleanliness and electrostatic cleanliness. Currents induced in the spacecraft structure are a major source of EMC disturbances because any voltage on the spacecraft surface induced by such currents will couple readily into the antennas. Good grounding and harness shielding practices will control these currents and should be the basis of an EMC "philosophy".

Power converters also represent a serious source of interference if left uncontrolled. The EMC committee would develop a plan for the use of crystal controlled DC-DC conversion in all spacecraft systems (including instruments), which can limit the interference to narrow frequency bands. The committee would review all subsystem test results and, in the case of test results in excess of defined limits, determine what remedial action (if any) is required.

Finally, the KuaFu-A spacecraft should be tested in a large EMC chamber at some point in the integration and test process.

4.1.5. Solar Wind Instruments Package (SWIP)

4.1.5.1. Principle and preliminary design

SWIP should include:

- A plasma ion detector (PID) will mainly be devoted to solar wind protons. We envisage a classical electrostatic analyzer system that allows determining the energy spectrum and both angles of incidence of the solar wind ions. The ability of measuring protons and helium ions separately is highly desirable but not mandatory. The energy range should extend from 0.2 to 10 keV. Various designs as used on many missions in the past are possible. The one used for the ROMAP (see <http://rzv048.rz.tu-bs.de/forschung/projekte/roslan/romap/>) instrument recently launched with the Rosetta mission might serve as a valid example of a minimum mass design. PID requires a free field of view towards the Sun of about sixty degrees in width, and therefore should be mounted near the front of the spacecraft. Since KuaFu-A is three-axis stabilized, angular coverage requires an electrostatic deflection system in front of the main instrument.
- A plasma electron instrument (PIE) will allow to measure the full electron spectrum that includes both the low-energy plasma electrons (with energies as low as 10 eV) and suprathermal electrons (with energies up to 10 keV). Special care must be taken to keep photoelectrons away from PIE. The field of view should cover as much as possible of the full 4π solid angle. This is required in order to allow detection of directed components of the electron population, i.e., Strahl electrons (in high-speed streams) and bi-directional electron streams (typical for magnetic clouds). PIE could be mounted on an extended beam in the permanent shadow of the S/C. Then it is protected from direct Sunlight, and the S/C obstructs only a minor fraction of the full 4π field of view. The SWEA and STE instruments on the upcoming STEREO mission could serve as a guideline for this type of instrument (see <http://sprg.ssl.berkeley.edu/impact/instruments/index.html>).
- A magnetometer (MAG) should continuously measure the three vector components of the IMF, up to about 100nT. We propose a dual-sensor fluxgate magnetometer

instrument for the KuaFu-A mission. The instrument is similar to many others flown on previous missions. The design proposed here bears direct heritage from the instruments on the Cluster, Double Star and Venus Express spacecraft. Each fluxgate sensor measures three orthogonal components of the magnetic field vector. The sensors are mounted on a boom which extends away from the spacecraft body to a distance of 2 to 3 meters. One sensor is mounted at the end of the boom and the second sensor about 0.5 meters from the end. The dual-sensor configuration serves two purposes: firstly, it provides redundancy and enhanced reliability, which is highly desirable given the scientific importance of the magnetic field measurements on KuaFu-A. Secondly, it allows the instrument to measure the *difference* between the fields at the two sensors. The field difference is due to magnetic interference coming from the spacecraft itself, so the dual-sensor measurements allow the detection and correction of magnetic interference. This results in an overall improvement in the measurement accuracy.

4.1.5.2. Payload resources: mass, power, data rate

As a baseline of how SWIP can be minimized in terms of required resources, one might consider the ROMAP instrument: the whole package, including a PID, PIE and MAG, all mounted as a single assembly at the end of a 1-meter boom, had a total mass of rather exactly 1 kg and a peak power consumption of 0.8 W. The data rate can be programmed such that optimum information is transmitted for the variable telemetry conditions that occur during the Rosetta mission. For KuaFu-A, we anticipate a different design in that PID will not be part of the boom instruments and will rather be located at the Sunward front of the S/C. This requires separate housing and additional harness to the electronics unit. Further, since PID might include a provision for separating and separately analyzing helium ions, the requirements will differ from ROMAP.

Table 4.13: Payload resource of SWIP

Instrument	Mass	Power	Data rate
	(g)	(W)	bps
PID	1500	1.5	1000
PIE	1500	1.5	1000
MAG	2000	2.0	2000
Electronics unit	1000	1.0	
Total SWIP	6000	6.0	4000

These are very rough guesses, based on previously built instruments. We believe these numbers can be met within a 20% margin.

4.1.5.3. Mission requirements of SWIPS on KuaFu-A

Orbit

Near-circular orbit around the L1 point, similar to SOHO and ACE.

Precision of control

The science requirements include continuous knowledge of the KuaFu-A position, with standard precision (ie., that obtained on a regular basis for SOHO, WIND and ACE).

Attitude

The spacecraft attitude should not deviate by more than say three degrees from Sun center line (note that the optical instruments have much more stringent requirements). Knowledge of attitude is needed within 0.1 deg precision. With respect to the roll position, we would recommend that the S/C is oriented such that its y-axis (perpendicular to its x-axis which should always be pointed towards Sun center) is always pointing at one solar pole.

Pointing

Three-axis stabilized, with main reference axis always pointed towards Sun center.

Pointing stability

The SWIPS data cycle takes about 1 minute. In that time the S/C pointing should not change by more than 0.1 deg.

4.1.5.4. Special requirements: continuous data transmission

Continuous data transmission to Earth is mandatory for a space weather explorer spacecraft. For example, a “beacon mode” as used for STEREO, would provide uninterrupted real-time transmission of KuaFu-A data, with highly reduced telemetry rate. The full data stream must always be stored on-board and be transmitted later.

4.1.6. Solar Energetic Particle Sensor (SEPS)

SEPS is designed to measure fluxes and composition of Solar Energetic Particles (SEPs) as required to meet the scientific goals of KuaFu A.

4.1.6.1. Instrument description

In order to satisfy these measurement requirements, SEPS consists of 4 sensors summarized in the table below.

Table 4.14

<i>Sensor</i>	<i>particles measured</i>	<i>energy range</i>	<i>mass (kg)</i>	<i>power (mW)</i>	<i>data rate (bps)</i>	<i>time resolution</i>
SEPT	electrons	20 - 400 keV	0.9	1100	120	1 min
	protons	20 - 7000 keV				1 min
	^4He					
SIT	^3He	0.15 - 0.25 MeV/nuc	0.93	660	240	30 s
	^4He	0.03 - 2 MeV/nuc				30 s
	$Z>2$	0.03 - 2 MeV/nuc				30 s
LET	protons	1.5 - 3.5 MeV/nuc	0.51	180	320	1 - 15 min
	^3He	1.5 - 1.6 MeV/nuc				15 min
	^4He	1.5 - 40 MeV/nuc				1 min
	$Z>2$	1.5 - 40 MeV/nuc				15 min
	$^{22}\text{Ne}/^{20}\text{Ne}$					
HET	electrons	1 - 8 MeV	0.7	70	120	1 - 15 min
	protons	13 - 100 MeV				1 - 15 min
	^3He	15 - 60 MeV				15 min
	^4He	13 - 100 MeV				1 - 15 min
	$Z>2$					

SEPT - The Solar Electron Proton Telescope

The Electron and Proton Telescope reference instrument is similar to the STEREO Solar Electron Proton Telescope (SEPT). The sensor telescope is constructed as an open

cylinder with two solid-state detectors. One detector aperture (electron side) is covered by a thin organic foil and the other detector aperture is surrounded by a magnet. The thin foil leaves the electron spectrum essentially unchanged but stops low energy protons (i.e, it is essentially only sensitive to electrons in the energy range 20 keV - 400 keV). The magnet sweeps away electrons on the other side of the cylinder but lets ions pass to that detector. Ions within an energy band from 400 keV/nucleon to 7 MeV/nucleon will be measured in this detector. The electron detector also detects ions with energy high enough to enter through the thin foil - this flux can be computed and subtracted from the electron flux.

Two sensor telescopes are mounted parallel, but with the electron/proton detectors facing opposite directions. These form a compact unit since the magnetic fields are shared between the telescopes. The complete telescope FOV consists of two 56° cones. The external magnetic field can be kept to low levels by exact matching of the individual magnets.

SIT - The Suprathermal Ion Telescope

SIT is a time-of-flight mass spectrometer whose telescope cross section is shown in the associated figure. The FOV is $16^\circ \times 44^\circ$, with the 44° angle in the ecliptic plane. Referring to the figure, the telescope analyses ions that enter the telescope through a thin entrance foil (200Å Al on 1000Å polyimide) and stop in an array of 9 solid state detectors. Secondary electrons from the entrance foil and solid state detector are accelerated and deflected, then strike chevron microchannel plates (MCPs), providing START and STOP signals for the time-of-flight measurement. The solid state detector signal provides a measurement of the kinetic energy of the ion. The time-of-flight T , the energy E , and the 8 cm path length in the telescope (L) are then combined to derive the mass of the ion: $M = 2E(T/L)^2$. The incident energy is obtained by correcting for the energy losses in the entrance foil and detector window.

The SIT geometry factor is 0.20 cm² sr, large enough to allow study of even small impulsive solar particle events. SIT is optimized for detection of He and heavy ions: the triggering efficiency for protons is $\ll 1\%$, ensuring the ability to measure heavy ions even in very large intensity events in the inner solar system. For each ion triggering the telescope, time-of-flight and energy information is obtained. Full information on selected events is telemetered, and all events are classified into mass & energy bins which are summed on-board to allow rapid accumulation of flux and spectra. SIT uses a common low-voltage power supply, and detector bias, and generates its own high voltage (~4 kV) for the microchannel plate/secondary electron assembly. The only commanding is occasional (every few months) adjustment of MCP bias.

LET - the Low Energy Telescope

The Low Energy Telescope (LET) measures the elemental composition of H-Fe and angular distribution of protons and helium. The energy range of protons and helium is 0.5 - 20 MeV/nucleon. In the energy range 1.5 - 20 MeV/nucleon ³He is resolved from ⁴He. Heavier ions are measured from 2.5 MeV/nucleon (O) and reach up to 60

MeV/nucleon (Fe). Thus, LET covers the gap between EPT and HET for protons and helium, and between SIS and HET for heavier ions.

In precise identification of ions, LET relies on the well-proven dE/dx -E technique with pulse height measurements. Most abundant species are identified and tabulated in energy by on-board algorithms in order to limit the telemetry requirements. Thus only a sample of pulse height data is linked down. In addition, classification in mass and energy based on a hardware implementation without pulse height analysis is required for high flux conditions. All data are collected with a time resolution of the order of seconds and with a wide angular coverage.

LET has three front telescopes each consisting of two silicon detectors (D1 and D2 in Fig. 3.4.4), and sharing a common stack of larger silicon detectors extending the energy range up to 20 MeV for protons. The view cone of each telescope is 25×25 degrees, with a total angular coverage of 115 degrees. The total geometric factor of LET is 0.11 cm² sr, approximately independent on energy. In the ideal case, LET should be accommodated such that the axis of the view cone of the centre telescope is in the ecliptic plane, the other two telescopes looking at North and South of the ecliptic. In addition, for full directional measurements, LET should be mounted on a scanning platform with an unobstructed view in the range 20-340 degrees towards West of sun.

HET - The High Energy Telescope

Several identical telescopes define the fields of view by sharing a CsI scintillator calorimeter in an efficient, weight saving geometry and allowing for substantial anisotropy information. The telescopes each contain three circular PIPS SSDs (thickness of 0.15 mm, 1 mm and 1 mm) with a total geometric factor of ~ 0.5 cm² sr. The FOV limits ion path length differences in all detectors so individual elements from protons to iron can be resolved. The particle type (e, p, heavy nuclei) is identified by measurement of energy loss (dE/dx) versus total energy via pulse height analysis. Penetrating particle signatures will be pulse height analysed as well in order to provide additional channels for adjacent higher energies and minimally ionizing particles. The whole detector system is wrapped in active anti-coincidence shielding. The CsI light output is detected with photodiodes, and so is the plastic scintillator. For the anti-coincidence shielding readout a photomultiplier tube or photodiodes are foreseen. Without any extra sensor mass, the detector can be used for X-ray and positron observations. The high-Z CsI scintillator material is extremely sensitive to X-rays. Positrons are identified by an electron energy loss signal in two front SSDs of any of the telescopes, with no signal in the third SSD, in coincidence with the observation of the annihilation X-ray energy of 511 keV in the CsI scintillator.

If no X-ray information is required, the CsI crystal can be descoped, and additional SSDs are included to increase elemental resolution via the dE/dx method.

4.1.6.2. Resource

All four sensors are body mounted onto KuaFu-A but have different field-of-view requirements.

SEPT: ~ 60 degree full opening angle cone centered along the Parker spiral both in the sunward and anti-sunward direction.

SIT: 45 by 20 degrees opening angle centered at 60 degrees away from the Sun-spacecraft line and in the ecliptic. The 45 degrees lie in the ecliptic.

LET: 133 by 30 degrees centered along the nominal Parker spiral both in the sunward and anti-sunward direction.

HET: 50 degree full opening angle cone centered along the Parker spiral both in the sunward and anti-sunward direction.

Pointing requirements of all SEPS sensors are modest, knowledge of 1 degree is sufficient to meet the scientific requirements.

4.1.7. Hard X-Ray and Gamma-ray Spectrometer (HXGR)

4.1.7.1. Instrument concept

The hard X-ray and gamma-ray spectrometer consists of several new-type room temperature semiconductor detectors (CdTe). The power consumption, weight and volume can be suppressed several times compared to an instrument based on normal techniques. Because of the charge collection problem in such detectors, the size and thickness of the CdTe detector is limited. For increasing the sensitivity of the observations, about ten detectors will be joined together to cover the energy range from 10 keV-3 MeV. The energy resolution is about 3% at 662 keV, which is about 2.5 times higher than that of present solar X-ray or gamma-ray detectors. For reducing the backgrounds, each detector can be used as an anticoincidence detector for the nearby CdTe detectors. Simulation results show that above 99% charged-particle backgrounds can be rejected using this method.

4.1.7.2. Instrument Summary

Area:	40 cm ²
Size:	15 cm × 10 cm × 10 cm
Energy resolution:	3% at 662 keV
Weight:	3 kg
Power:	5 W
Data Rate:	1 k bytes/s

4.2. Scientific payload on KuaFu-B

The science objectives of the KuaFu-B mission warrant global imagers, *in situ* observations, and ionospheric observations. The global imaging requirements drive the orbit selection. As well, the large data rates of the UVAMC are the primary driver of the KuaFu-B telemetry requirements. As we are after better spatial resolution than has previously been achieved, there is a strong requirement for pointing and knowledge of orientation. The spin rate is set primarily by the needs of the FUVSI, which requires a 30 s spin rate to function best.

The instrument complement on KuaFu is divided into three types:

(1) The global imaging instrument complement consists of the UVAMC electron auroral imagers, FUVSI Spectroscopic Imager, WFAI perigee imager, and the NAIK ENA ring current imager;

(2) The *in situ* fluxgate magnetometers, as well as the three charged-particle instruments;

(3) The radio-science experiments onboard KuaFu-B, carried out by a Tri-Band Beacon (TBB) using the downlink signal.

4.2.1. Far Ultraviolet aurora monitoring cameras (UVAMC)

General Design

The design of the UVAMC imagers is motivated by a desire to record snapshots of auroral dynamics with high temporal resolution under night-time as well as fully sunlit conditions. An intensified FUV CCD-based imager with fast optics will be developed. Such a design allows each image pixel to be exposed simultaneously, giving true snapshot ability as well as high temporal resolution. Given that the spacecraft spins at a rate of 2 rpm, a too long exposure time would result in smearing of the image across the CCD. In fact, given the various parameters of the mission, the allowable exposure time would be no more than a few milliseconds before smear would become significant. Even with a fast optical design and an image intensifier, this exposure time is far too short to be able to image faint auroral emissions. To overcome this problem, the CCD will be run in the Time Delay and Integration (TDI) mode. This approach works well provided that the columns of the CCD (i.e., the direction of charge-stepping) is aligned almost exactly perpendicular to the spin axis of the satellite so that the image points move strictly along a CCD column (and not at some oblique angle to it). Considering the high spatial resolution requirement, this will place demands on the satellite platform pointing stabilization performance.

Optical Design

The image-forming section of each camera is comprised of a fast, off-axis all-reflecting telescope with three spherical mirrors. The three-axis system is a departure from the heritage University of Calgary line of imagers (Viking, Freja, InterBall, IMAGE-WIC), but is warranted by our objective to achieve isolation of signal from parts of the LBH band (ie., for separation of the LBH-L and LBH-S signals). This type of reflecting telescope is compact, is fully corrected for spherical aberration, coma, and astigmatism. Moreover, it has excellent resolution over most of its field of view and has a high throughput in the far ultraviolet part of the spectrum. Each camera has a 25 degree circular field of view with an optical axis perpendicular to the spacecraft spin axis. This field of view must be unobstructed by booms or other protrusions that would scatter sunlight into the optical system and causing possible damage to the detector. Adequate baffling will be implemented, and a reusable aperture door is planned.

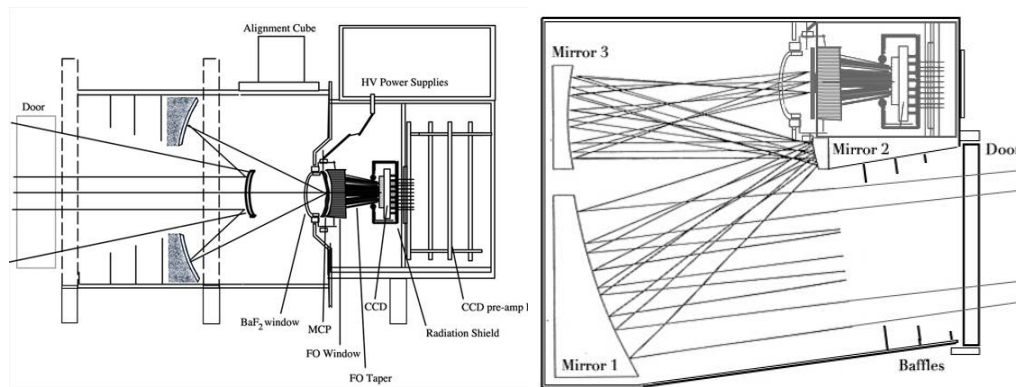


Fig. 4.8 UVAMC optical design. **Left:** two mirror (heritage) design. **Right:** Three mirror concept to be utilized on KuaFu-B.

Filter and Coatings

Special proprietary dielectric multilayer mirror coatings (Torr et al., 1995) will be used. These have very low reflectivity in the Visible and Near-UV region, and are manufactured for high reflectivity in the LBH-short or LBH-long wavelength region, as required. The three reflecting surfaces on which to deposit such coatings will help us achieve the required 10^{10} out-of-band rejection, for an imager sensitivity of ~ 30 Rayleighs in a TDI exposure captured during the 30 second spin. In addition, there is a BaF₂ window in front of the detector, which provides the short wavelength cutoff. A CsI (solar blind) MCP photocathode provides additional long wavelength cutoff at about 200 nm. A high level of cleanliness is required during handling, installation and testing. UVAMC optical components must not be exposed to environments exceeding 100,000 particles per cubic foot, greater than 0.5 microns in size [TBC]. All parts must be protected from contamination during shipping and handling. A sealed aperture door will provide some measure of protection of the filters and coatings.

Detector

A micro-channel plate (MCP) image intensifier placed at the focal surface of the

camera is illuminated by the FUV image formed by the all-reflecting optics. Rather than an open intensifier as was used in the VIKING UV Imager, a closed (i.e., sealed) design is employed in order to avoid contamination of sensitive elements (e.g., photocathode) and saturation due to ambient electron fluxes.

The sealing is accomplished by placing a BaF₂ filter as a window in front of the photocathode. For structural reasons, the windows must be relatively thick. 2.5 mm of BaF₂ will be used in order to provide the short wavelengths cut-offs. Once a photon passes through the window, it impinges upon a photocathode material (CsI) designed to be photoemissive over a particular wavelength region. The CsI photocathode is opaque and deposited directly on the front surface of the MCP.

Once a photoelectron is confined to a MCP pore, it is accelerated by a potential of several kV to produce a cascade of electrons out from the rear of the MCP. This acceleration is necessary for the electrons to traverse an aluminum coating overlaid on a P43 phosphor. The purpose of the coating is to shield the subsequent optical chain from light which penetrates (without photoconversion) the MCP. P43 is baselined in spite of its low efficiency (30% of P20) because of its particularly fast decay time (> 100 ns). This is required because of the relatively high spin rate of the spacecraft: since a pixel (a resolution element on the ground) sweeps through the field of view at a fairly high rate, it is required that the response of the phosphor due to one pixel must be sufficiently decayed before the next pixel arrives. Once the electrons strike the phosphor, photons are produced. These photons are then fiber-optically coupled to the CCD.

The baselined CCD is a 2048×2048 pixels chip (e2v CCD42), binned down to 512×512 yielding a ~ 30 km resolution from apogee with a 25 degree field of view. The CCD will not require a mechanical shutter. The CCD needs to be operated at some stabilized temperature below 0 degrees C in order to reduce thermal noise. This is accomplished by using a radiator that faces directly towards Earth, supplemented by low-power active cooling (or heating) from a TEC. This solution provides for best control of the CCD temperature at a fairly low power and mass penalty. Another solution is to use a radiator at the back of the spacecraft and having the spacecraft attitude control ensure that the radiator never sees the Sun. This is attractive in terms of required radiator area, but could be heavy, depending on final spacecraft topology. These issues will have to be revisited at the appropriate time. The power figures given in [Table 4.15] include provision for some low-power active cooling. Temperature sensors will be mounted at strategic places, and temperature will be continuously monitored.

We point out that although our plan is to use 4×4 binning down to 512×512 pixel images, there is a very real possibility that soon-to-be-released photocathode materials would increase our optical efficiency by a factor of 5. If this new technology reaches flight-readiness in time to be included in the UVAMC imaging systems, then we would likely argue to back off to 2×2 binning, still achieving a better sensitivity than that baselined, and improving apogee NADIR resolution to ~ 15 km.

Table 4.15 Initial specifications for the optical design of the UVAMC.

Exposure	Rows on square CCD	512
	Total FoV [degrees]	25
	Angular pixel FoV [degrees]	0.049
	Spin Period [seconds]	30
	Spin Rate [degrees/second]	12.0
	Effective Exposure time [seconds]	2.1
	Cadence [seconds]	30.0
Optical Efficiency	Mirror reflectivity	0.85
	Resulting reflectivity, 3 reflections	0.61
	FUV Filter Transmission	1.00
	Intensifier window transm	0.96
	Photocathode QE [conventional technology]	0.15
	MCP efficiency	0.55
	Total of above [throughput]	0.049
Optical Parameters	Aperture [cm ²]	6
	Diameter [mm]	27.6
	Assumed MCP diameter [mm]	40
	f/#	3.3
	Pixel Omega [square pixels]	7.26E-07
Signal to Noise	Radiance-kR conversion factor	7.96E+07
	Calculated Sensitivity [counts/kR/s]	16.866
	Counts/R/pixel/exposure	0.035
	Noise Equivalent Signal [R/exp]	28.459
	Good SNR	3.0
	Brightness for good SNR [R/exp]	256
Spatial Resolution	1 RE [m]	6.38E+06
	Satellite Apogee [Re]	7
	Derived Altitude [km]	38280.00
	Full Earth angle from above altitude [degrees]	16.43
	Auroral Oval subtends from alt [km]	1048
	Nadir resolution at apogee [km]	32.6
Data Rate	Bits per pixel	12
	Total bits/image	3.15E+06
	telemetry rate-no compression [Mbits/s]	0.10
	telemetry rate-no compression [Mbits/s]	0.03

Orbit suitability for Spatial Resolution Requirements

The 1.8×7 Earth Radii orbit (geocentric distances) proposed for KuaFu allows for continuous global imaging with excellent spatial resolution over much of the auroral

and polar regions, and down to mid latitudes. Mid-latitudes are important if we are to study the global consequences of large geomagnetic storms. To demonstrate that this is an effective orbit for UVAMC, we include Figure 4.9, which is a panel plot of distributions of UVAMC spatial resolutions for pixels with geomagnetic latitudes greater than 40 degrees. Note that in producing this figure, we used the proposed 25 degree FOV and 512×512 pixel image. There are 20 panels in the plot corresponding to equally spaced times during one orbit.

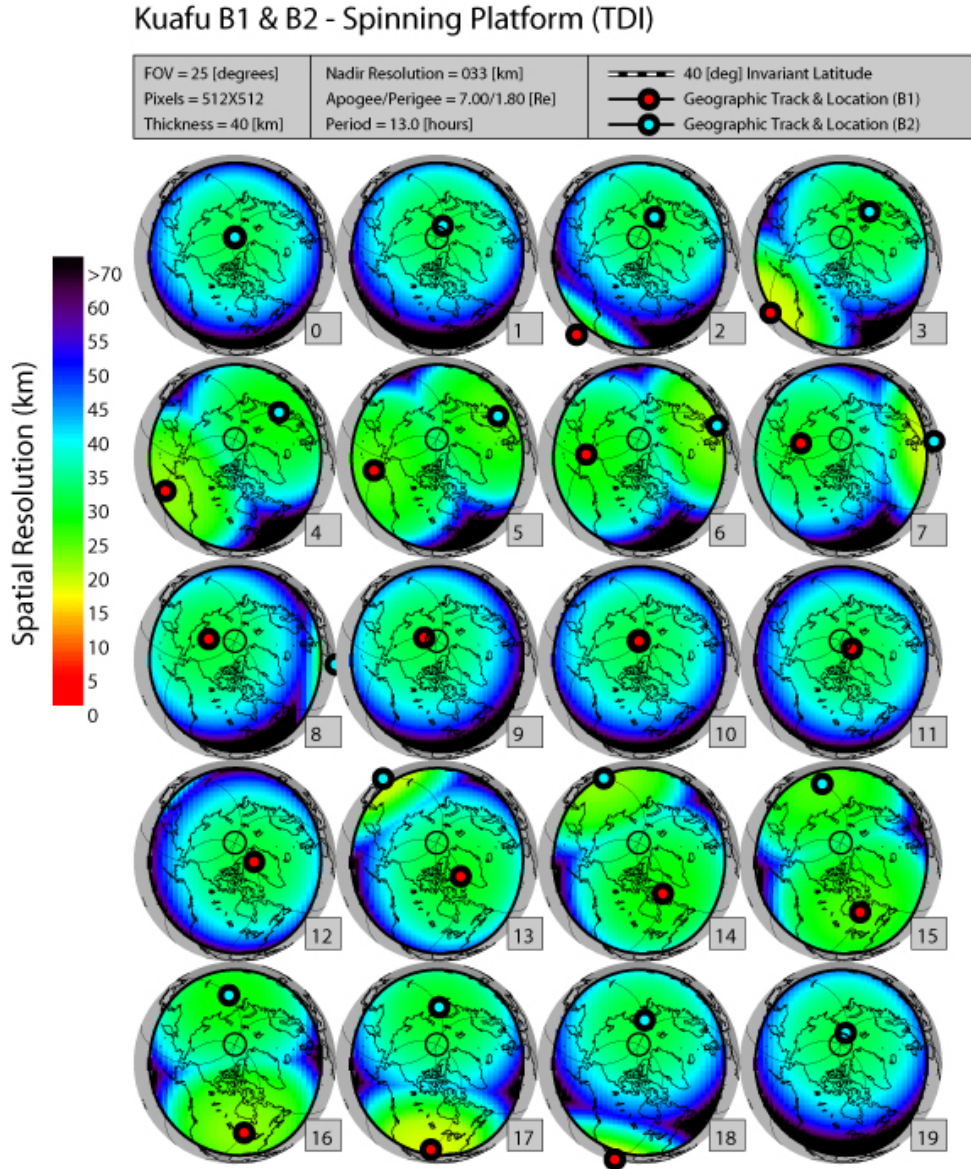


Fig. 4.9: Distribution of KuaFu-B UVAMC spatial resolutions that would be obtained by UVAMC instruments with the proposed specifications (512×512 pixel images with a 25 degree FOV) on the two satellites in the proposed orbit. The twenty plots are from equally spaced times during one full orbital period. Note that KuaFu B goes from apogee to apogee during this time.

Electronics (UVAMC-E)

The two imagers will be controlled by a common electronics box, the UVAMC-E. UVAMC-E will be DSP or FPGA based, depending on the results of upcoming radiation dosage modeling. The controller provides bias voltages, three phase clock signals to the CCD parallel and serial registers, signal processing to extract and digitize (16 bits, via a dual-slope integrator) the CCD output signal, and a fast serial interface (e.g., asynchronous RS-422) to the spacecraft main data handling unit. There will be built in a capability to command the imagers into a variety of operational modes (frame rates, binning, CCD gain, etc).

The design of the dual-slope integrator and clock drivers are optimized for fast settling time. As the electronics unit (and the preamplifier) will have more than sufficient speed, it is possible to continuously clock the CCD and thus generate images greater in extent than the 2048 rows of the CCD. This allows us to exceed the 25-degree field of view in the scan plane. Thus, a full 360-degree image could in principle be generated, highly useful for in-orbit sensitivity and spatial calibrations using stars. By utilizing on chip binning, signal to noise ratio can be increased during operational modes where some spatial resolution can be sacrificed. To this end, in order to achieve our requirements we anticipate utilizing 4×4 binning down to 512×512 pixels.

In case of radiation-induced upsets, internal program memory and registers can be reloaded from EDAC protected memory periodically, as signaled by a watchdog timer. More drastic failures may require a re-initialization from on-board EPROM. The instrument input power supply voltage will be $+28\text{VDC} \pm 6\text{V}$. The instrument will survive indefinite application of input voltages between 0 and +40V, with no damage.

Alignment of CCD with Spin-Axis

Both the UVAMC and SI instruments require a spinning platform. To accomplish the stated science, precise alignment of the instrument on the satellite is required. The basic image acquisition method utilizing the TDI (Time-Delayed Integration) approach requires that the CCD charge transfer direction be parallel (or anti-parallel, depending on the optical design) to the direction of the spin. This in turn generally requires that the optical axis of each camera must be perpendicular to the spin axis. The plane swept out by the vector perpendicular to the spin axis in which the optical axis lies is denoted the "scan plane". Proper operation requires accurate knowledge of the actual scan plane and hence spin axis rotation vector.

Alignment is crucial and involves 3 degrees of freedom. These are

- (1) Angle with respect to a fixed scan plane position (initial accuracy of 1-2 degrees is sufficient, while accuracy to within one pixel FOV is required for proper data analysis). Accuracy to within one pixel field of view is required for proper data analysis.
- (2) Optical axis of each camera should be within TBD degrees of scan plane.

(3) Charge transfer direction must be within 0.014 degrees (half a pixel over a distance of 2048 pixels) of parallel to scan plane. This is the most crucial alignment as mismatch between charge transfer direction and spin direction will result in image smear.

The cameras will be equipped with alignment cubes to achieve proper alignment. It is important to note that correct alignment will require full knowledge of true satellite rotation axis. This must be determined during full-up satellite tests.

Open parameters

Several parameters can still be adjusted according to the overall needs of other payload instruments, platform capabilities, and available detector technologies:

- (1) Detector (CCD) type and format
- (2) TDI mode or summing multiple short exposures
- (3) UVAMC-0 and UVAMC-1 can be one single structure bolted to the base plate, or two separate structures bolted to the base plate
- (4) Type of high-speed interface to main KuaFu data handling unit
- (5) Active or passive cooling of the CCD

Payload resources

Table 4.16 Initial technical budget for each UVAMC. Note these are estimates and are subject to change as a result of Phase-A work.

Mass UVAMC-0 (LBH-long imager)	9.0 kg
Mass UVAMC-1 (LBH-short imager)	9.0 kg
Mass UVAMC-E (Electronics box)	3.0 kg
Dimensions UVAMC-0	25 x 24 x 15 cm
Dimensions UVAMC-1	25 x 24 x 15 cm
Dimensions UVAMC-E	20 x 20 x 10 cm
Power UVAMC-0	4 W
Power UVAMC-1	4 W
Power UVAMC-E	3 W
Data rate, per image	3.15×10^6 bits
Data rate, total per UVAMC	0.1 Mbits/sec (sustained)
Temperature Limits	Survival, non-operational: -40 C to +60 C Operational: -25 C to +40 C (electronics) -25 C to +20 C (cameras)

Estimated (February 2005) payload resource requirements are listed in Table 4.16. These are preliminary "guesstimates" that will need to be adjusted according to final design options that will be selected. The spacecraft design must ensure that the

combined conducted and radiated emissions from all sources will not adversely affect the correct scientific operation of the UVAMC instruments or degrade the performance of elements of the spacecraft bus subsystems.

4.2.2. Far Ultraviolet Spectro-Imager (FUVSI)

Optical Design

The first element in the imaging monochromator is an aperture in the form of a grill of parallel slits followed by a collimating mirror that produces parallel light from any point in the entrance aperture plane.

The grating follows the collimating mirror at the distance so that any parallel light coming through the slit is focuses to a point at the grating. Thus, an object at infinity in front of the instrument is imaged close to the grating surface. The grating disperses the light according to wavelength. The wavelength-related angular dispersion of the light is the same for all points of the image. Thus, imaging and wavelength selection are independent of each other.

The grating is spherical and focuses parallel light at the plane of the exit slit. A spectral region defined by the position and size of the slit(s) receive an equal amount of light from any point in the image. The last component of the system, the back imager, focuses the intermediate image situated at the grating, on the detector. The location and width of the exit slit(s) define the spectral region and the spectral width of the light passing through the system and therefore, the spectrometer acts like an afocal filter in the optical system.

Two wavelengths are selected with two separate exit slits, one for imaging the Doppler-shifted Lyman- α , the other one for the O I 135.6 nm emission.

The most remarkable property of this Imaging Monochromator is that imaging and wavelength properties independent of each other giving the capacity to combine e.g. high spectral with low imaging resolutions or vice versa.

Next figure shows a ray-tracing at 121.8 and 135.6 nm including the zero and +1 diffraction orders only (for clarity). The instrument consists of two main optical subsystems: a monochromator, and a “twin” back-imager (one at 121.8 nm and the other one at 135.6 nm).

The monochromator was designed to produce the largest dispersion, in order to reach the required high spectral resolution. Focal length is 500 mm and the grating ruling is 3600 lp/mm (holographic recording). The grating curvature is spherical; the collimator curvature is hyperbolic. The linear spectral dispersion is about 1820 $\mu\text{m}/\text{nm}$ in the exit slit plane. As depicted in figure 4.10, a first image of the Earth is produced approximately at the grating plane. The aim of the back-imager is to relay this image after diffraction by the grating, in order to obtain two spectrally separated images. Each

sub-assembly of the back-imager is a two-mirror optical system. The first mirror is spherical. The second one is conical (elliptical) and off-axis. A flat folding mirror is added to the 135.6 nm imager in order to allow fitting the two detectors in close proximity.

The slit configuration is made of a grill with 9 parallel slits, designed to stop the 120 and 121.6 nm (121.567 nm) lines, simultaneously. The slit spacing (period) is determined for this purpose: 0.5223 nm i.e., one third of the wavelength difference between the two lines.

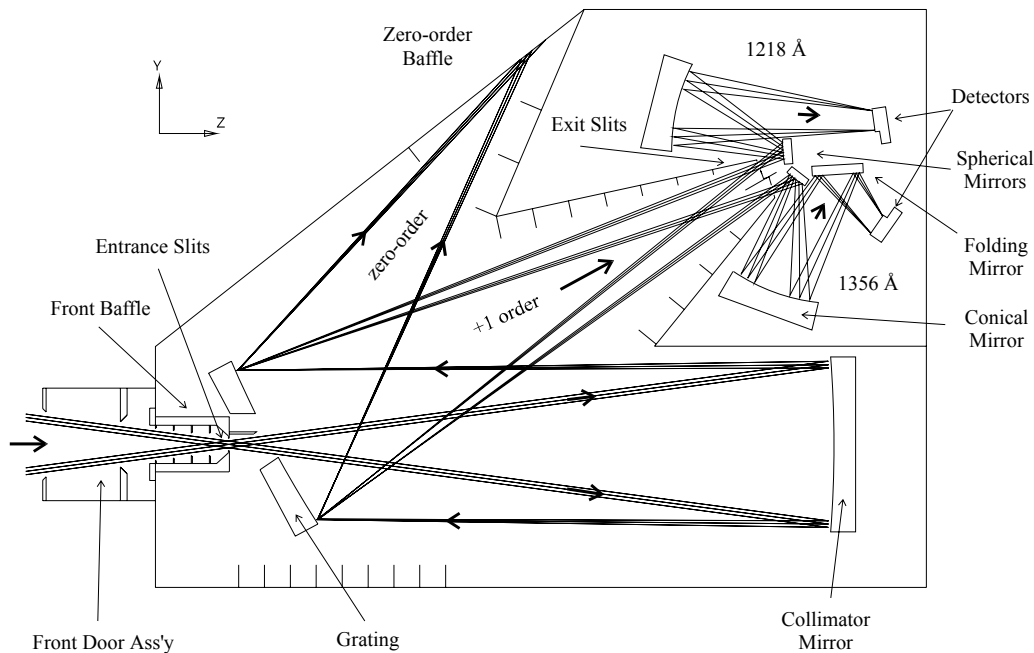


Fig 4.10: Design of FUVSI

Detectors

The detectors use a KBr photocathode on a MgF_2 window image tube with a triple-stack microchannel plate (MCP) intensification. The intensified image is detected by a crossed delay-line type detector with two 128×128 pixels, each active areas covering 20×20 mm. This kind of detector presents a QE of 17% at 121.6 nm and of 14% at 135.6 nm. The detector resolution is about 60 μm .

The detectors could probably also be CMOS covered by some type of phosphor transferring FUV to visible. The selection of the best technology is still TBD and has to be studied during the design phase of the instrument.

Electronics

The detector preamplifiers and high voltage power supplies are housed in the

sensor box near the detector. Like the other photon sensors, the FUVSI detects the position of every photoelectron by position-finding circuitry, and the images are produced in RAM memory by integrating the detected pulses according to a look-up table that is dependent on the rotation phase of the spacecraft.

A good knowledge of the satellite spinning axis with respect to the image is needed. The accuracy required for operation of UVAMC should suffice.

Operation

The FUVSI operation is such that the RAM memory stores a 2-D array of brightness measurements for two separate wavelengths (121.6 and 135.6 nm). The FUVSI has only one mode of operation. For some orientations of the spin axis, the Sun may enter the field of view at some spin phases. As with EUV, the control microprocessor will automatically reduce the high voltage to the MCPs to avoid excessive counting rates. The filters will prevent damage to the detector by focused visible sunlight.

Heritage

The FUVSI instrument is in orbit on the IMAGE NASA spacecraft since March 25, 2000. Therefore, the instrument is fully qualified with MCP detectors. If a CMOS detector is chosen, it should be similar to the SWAP/PROBA2 detector and would be qualified before 2007.

Sensitivity and Calibration

The absolute response of FUVSI is about 1% at both wavelengths of interest: 121.8 nm and 135.6 nm.

The entrance aperture slit grill is about 1 cm^2 . Therefore, assuming an input of 1.6 photons per Rayleigh, the overall efficiency of the instrument is about 0.017 counts per Rayleigh for a 5 s exposure.

The calibration of the FUVSI is relatively conventional. It will be calibrated for absolute sensitivity as a function of wavelength in band and out of band. It is important to determine the response of the instruments to natural sunlight as reflected from objects such as white clouds. Also, every pixel will be measured in the calibration to determine any geometric distortion as required for the flight software. Facilities exist at all photon imager institutions to perform these calibrations.

4.2.3. Wide Field FUV Auroral Imager (WFAI)

Module design

The camera comprises a radially-slumped square-pore MCP as focusing optic and a convex MCP detector with continuous resistive anode readout with a 400×200 pixel format. This detector type circumvents the critical spin axis alignment issues suffered by auroral imagers which require pixel level orientation for TDI readout of their intensified CCDs. An optic radius of curvature of 100 mm gives a focal length of 50 mm, with an anticipated angular resolution of 6 arcmin (1/600 radian). Figure 4.11 shows a cross-section of the camera module, indicating the simplicity of the design allowed by the use of the MCP optic. For KuaFu, the camera will have a rectangular aperture 100×50 mm² in size. The long dimension is aligned within the plane containing the spacecraft spin axis, 100 mm providing the ~50° angular field-of-view necessary to image the whole oval from a perigee altitude of 0.8 R_E . The spin of the spacecraft allows the camera to scan the oval, so that only a “slit” need be imaged. This allows the short dimension of the aperture to be divided into multiple “slits”, each fitted with a different filter, and each focusing on a different portion of the detector. Three filters could be fitted across an aperture 50 mm wide. At present it is expected that these filters will provide similar wavelength coverage to the apogee cameras onboard KuaFu, to allow like-for-like comparison between aurora in the two hemispheres. The angular resolution achievable by the camera will provide images with a spatial (nadir-pointing) resolution of 10 km from a perigee altitude of 0.8 R_E . Even at apogee the spatial resolution of the images will be of the order of 60 km, providing good science at all parts of the orbit.

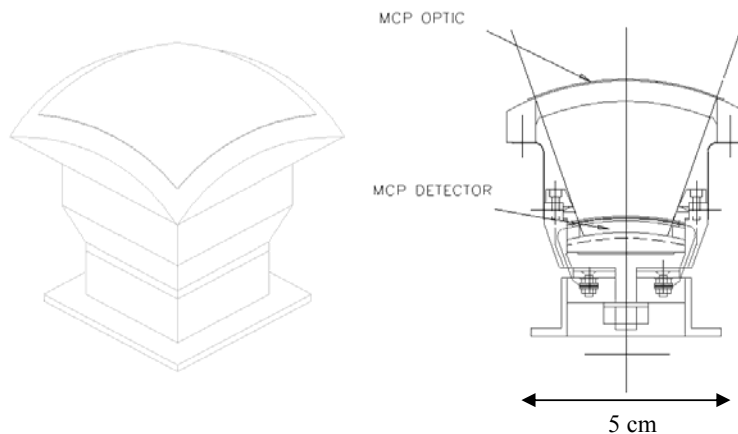


Fig. 4.11: Schematic view of a single module. The square cross section of the design permits close packing of individual modules into a multi-module telescope when necessary. Alternatively, a cylindrical structure would be appropriate if the field of view was synthesized from individual modules mounted at different locations around the spacecraft bus.

Resources

- (1) The volume estimate of a single module will be 100×100×100 mm³.
- (2) The mass estimate is 1.5 kg (including contingency).
- (3) Power requirement is 10 W.

Some outstanding issues

(1) A radiation analysis in the KuaFu orbit needs to be performed to scope the detector shielding against SAA or other particle fluxes.

(2) A thermal analysis is needed to indicate stresses arising from the unfamiliar spin mode of the satellite.

4.2.4. Neutral Atom Imager on KuaFu (NAIK)

Mechanical design

The NAIK instrument may, conveniently, be described in terms first of its Sensor Head and then of its Electronics Box, similar to NAUDU onboard DSP. Because of the different spin pattern of KuaFu platform to that of DSP, necessary modification will be made for NAIK on the basis of NAUDU.

The cylindrical Sensor Head (SH) protrudes beyond the skin of the spacecraft so as to provide a free field of view for each of its sensors. It contains 16 solid-state detectors, an electrostatic deflector/collimator system and a circular front-end electronics board (FRONT) on which is mounted a set of charge-sensitive preamplifiers and calibrated pulse amplifiers. The EB contains six electronic boards, namely a motherboard (MB), a high-voltage board (HV), two discriminator-counter boards (DCNT), a data processing unit (DPU) and a power distribution board (PD). The electrical connection between the SH and the EB is made by means of a multi-pole connector which directly connects the FRONT board to the MB. There is no cable harness inside the instrument. The high-voltage connection is provided using two, custom designed, HV connectors that directly connect the HV board to a deflection system. Those boards interfacing with the spacecraft system (the DPU and the PD), are each equipped with auxiliary sub-panels that carry the spacecraft interface connectors. These connectors protrude from the EB through openings in the back panel. [Fig. 4.12](#) shows the interconnection of several electronic boards of the instrument with the motherboard.

Sensor system

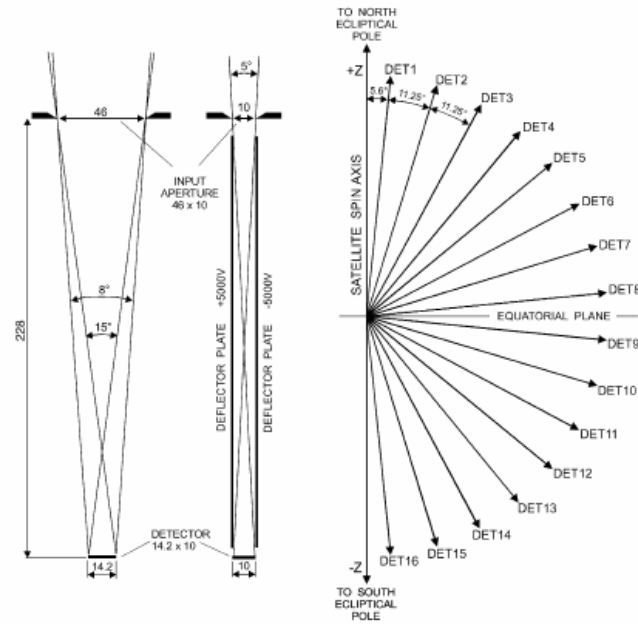


Fig. 4.12: Left: Definition of the field of view of a single detector; Right: pointing directions of the 16 detectors.

Sixteen custom designed Passivated Ion Implanted Silicon (PIPS) detectors are mounted at four different heights in the Sensor Head. These detectors, which each have a thickness of 300 μm , are fully depleted. The geometry of each sensor is characterized by a solid state detector (SSD) which has a rectangular active area of $14 \times 210 \text{ mm}^2$ and an input aperture of $46 \times 510 \text{ mm}^2$ that is located at the opposite side of the SH at a distance of 228 mm. The sensors have, individually, equal fields of view $11.5^\circ \times 2.5^\circ$ (FWHM), regularly distributed over an 180° angle in the elevation plane (Fig. 4.13). An important feature of the sensor system is its large geometric factor ($0.0125 \text{ cm}^2 \text{ sr}$ per $11.5^\circ \times 2.5^\circ$ pixel). Since mechanical collimation is employed, the pixel size does not depend on particle energy and mass. Because of the deposition on each detector of a metallization layer (200 nm of Al), the Sensor Head is impervious to Lyman- α radiation from the geocorona. The spacecraft spin allows the azimuthal plane to be divided into 128 equal sectors through counting the pulses of the onboard Spin Segment Clock (which are supplied to NAIK by the Spacecraft Service System). The full 4π solid angle is thus divided into $16 \times 128 = 2048$ pix-pixels and, given the spacecraft spin period ($T_s = 4 \text{ s}$), the integration time for one pixel is $4\text{s}/128 = 31.25 \text{ ms}$. NAIK can record a complete 4π image on the completion of each spacecraft spin, in synchronization with the spacecraft's Sun Reference Pulse. The electrostatic detection system utilizes a bipolar high-voltage system ($\pm 5 \text{ kV}$) which provides a field intensity of 10 kV/cm in the detection gap. It is designed to prevent charged particles with energies of 300 keV from entering the detectors (transmittance 0.01%). The five circular

detection plates are each manufactured from copper-epoxy fiberglass of thickness 1.6 mm. The copper surface of each plate is chemically blackened with copper sulphide to provide high-absorption properties with respect to particles and electromagnetic radiation. The plates of the detection system are mechanically supported by a set of insulation spokes, made of PEEK 450G (Poly-Ether-Ether-Ketone) high-performance plastic material. The spokes also inhibit crosstalk between sensors located in the same layer and Fig. 4.13 shows the geometry of a single layer (L1) of this four level system Fig. 4.14 shows the cross-section of the sensor head derived from a NAIK virtual model.

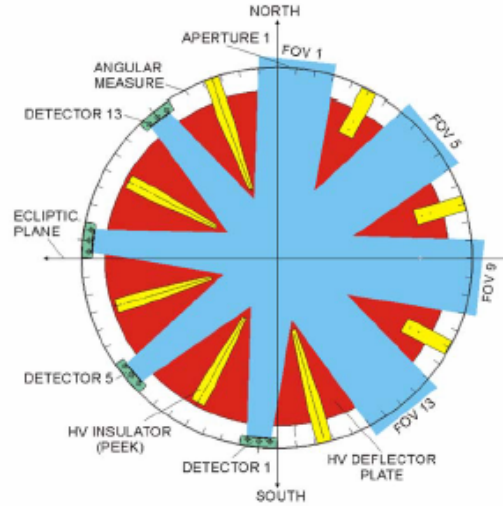


Fig. 4.13: Geometry of the Level-1 of the four-level deflection system

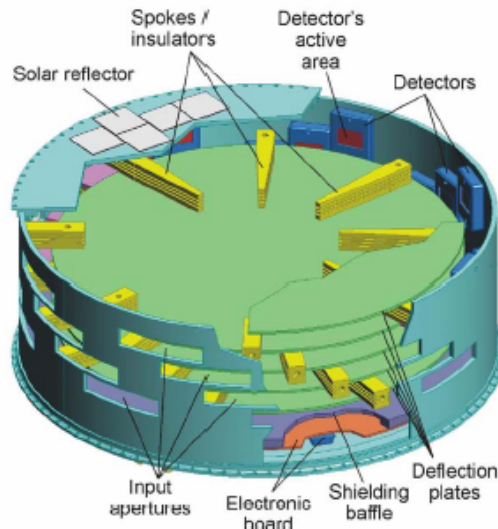


Fig. 4.14: Sensor Head cross section derived from a NAIK virtual model

Basic specification:

Table 4.17: Main Parameters of NAIK

Weight	6 kg
Maximum dimension (LWH)	290 mm×239 mm×239 mm
Power consumption	5W (from 28 V direct current)
Number of detectors	16
Detector type	PIPS , light-tight, custom design
Single detector active area	142 mm ² (14.2 mm 10mm)
Discrimination levels	20 keV, 50 keV, 100 keV, 300 keV
Field of view (each detector)	$11.5^{\circ} \times 2.5^{\circ}$ (FWHM, elev. \times azimuth)
Geometrical factor (each detector)	0.0126 cm ² sr
Resolution over 4π solid angle	2048 pixels
Image synchronization	by Sun reference pulse
Continuous data rate	0.5 kbps - 16 kbps
Charged particle cutoff energy	300 keV
Deflection high voltage	10 kV
The optimum operating condition range	-20 ⁰ C - 0 ⁰ C

4.2.5. Fluxgate Magnetometer (FGM)

Instrument description

The magnetometer consists of two triaxial fluxgate sensors with associated sensor electronics, digital processing unit and DC/DC converter (Figure 4.15).

Table 4.18: Main Parameters of FGM

Range	+/-18000 nT
Resolution	8 pT
Data rate	128 Hz
Telemetry rate	7 kbps
Power consumption	Max 4.25 W
Mass	total 1150 g
electronics box	1000 g
Sensors	2 x 75 g
Dimensions of electronics box	155 x 142 x 99 mm ³
Dimensions of sensor	67 x 67 x 42 mm ³

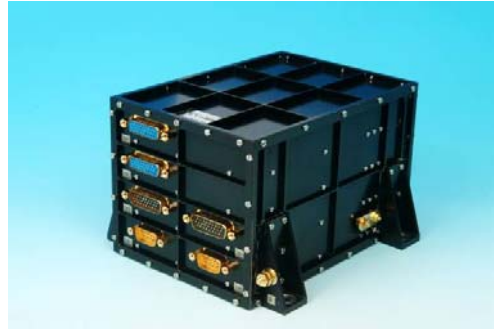


Fig. 4.15: Electronics box of Venus Express magnetometer

Request to S/C and Mission Operation

Telemetry rate: 128 vector/s, 7 kbps (primary sensor 128 Hz, Secondary sensor 2 Hz) – This is very important. KuaFu is in the similar orbit as Polar (Apogee $9 R_E$) and TC-2 (Apogee $7 R_E$), to improve the scientific return, we need better resolution both in data rate and data accuracy. We need much more telemetry rate than Polar or TC-2 (Polar: 8 Hz; TC-2: 22 Hz). High resolution data is useful to study the turbulence which is expected in the cusp region due to the high-latitude reconnection or the inflow and outflow of the plasma.

Magnetic Cleanliness

The magnetic field at the outboard sensor should be below 0.5 nT. This requires a much rigid magnetic cleanliness than TC-2. Either re-design or improvement of the solar panel of TC-2 is needed, or the boom must be significantly longer. We would suggest a 6-m rigid boom (the boom length will be the same for KuaFu A and B to make the manufacture easy).

4.2.6. Medium Energy Charged Particle Experiment (IES/IPS)

Description

The instrument design, as flown on the ISTP Polar and Cluster spacecraft, is shown in Figure 4.16. The instrument for Cluster also included a capability for species detection, but we propose that the simpler design adopted for the Polar spacecraft is more appropriate for KuaFu B. Polar had a very similar orbit to that proposed for KuaFu-B ($2 \times 9 R_E$).

The Electron Detector IES: Electrons with energies from 20 keV and 400 keV are measured with the novel Imaging Electron Spectrometer (IES).

The Proton Detector IPS: Protons with energies from 20 keV and 400 keV are measured by an essentially equivalent design for the Imaging proton spectrometer (IPS)

For both, advanced microstrip solid-state detectors having a 0.5 cm _ 1.5 cm planar format with three individual elements form the image plane for three acceptance ‘pin-hole’ systems. Each system divides a 60-° segment into three angular intervals. A schematic cross-section of an IES pinhole camera is presented in Figure 4.16. Three of these detectors arranged in the configuration provide electron/proton measurements over an 180-° fan in polar angle.

The key parameters of the instrument are given in Table 4.19 and 4.20

Table 4.19 Key Parameters of the Magnetometer Instrument

Mass, sensors	3.4 kg
Mass, DPU	2 kg.
Total mass	5.4 kg
Power consumption	5 W.
Energy range (electrons)	20-400 keV
Energy range (protons).	20-1500 keV
Polar angle resolution	180°/9
Azimuthal resolution	360°/16
Energy resolution	6 keV
Nominal no energy bins	16
Geometric factor (total/pixel)	(0.02/0.0022) cm ² sr

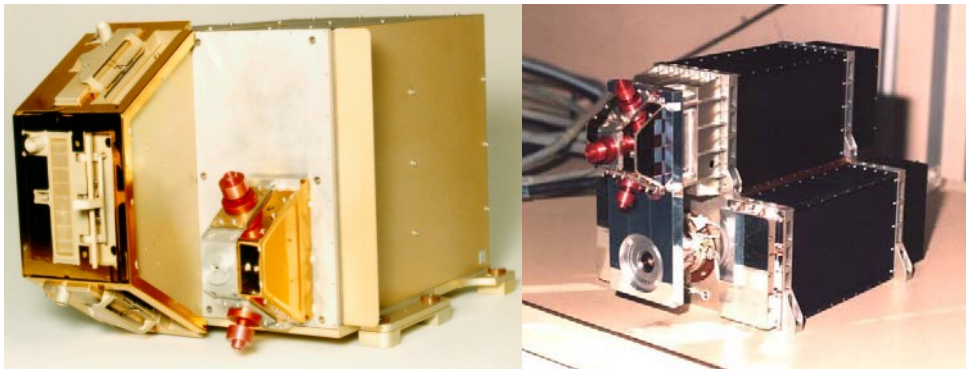


Fig. 4.16: The CEPPAD (Polar spacecraft) and RAPID (Cluster spacecraft) instruments.

Table 4.20: Operating parameters of the instrument

	IIMS	IES
Energy range (keV)		
Hydrogen (0, T)	40–75	–
Hydrogen (E , T)	75–1500	–
Hydrogen (E_M^a , T)	1500–4000	–
Electrons	–	20–400
ENA	40–200	–
Mass resolution (A/dA)	4 (oxygen)	–
Field-of-view	$\pm 3^\circ \times 180^\circ$	$\pm 17.5^\circ \times 180^\circ$
Angular coverage		
Polar (range/intervals)	$180^\circ/12$	$180^\circ/9$
Azimuthal (range/sectors)	$360^\circ/16$	$360^\circ/16$
Deflection voltage (kV)		
Range/steps	0–10/16	–
Geometric factor ($\text{cm}^2 \text{ sr}$)		
Total (180°)/per pixel	$2.7 \times 10^{-2}/2.2 \times 10^{-3}$	$2.0 \times 10^{-2}/2.2 \times 10^{-3}$

^a The value E_M corresponds to channel 256 in the energy ADC.

4.2.7. High energy charged particle experiment (HECPE)

Principle of the instrument

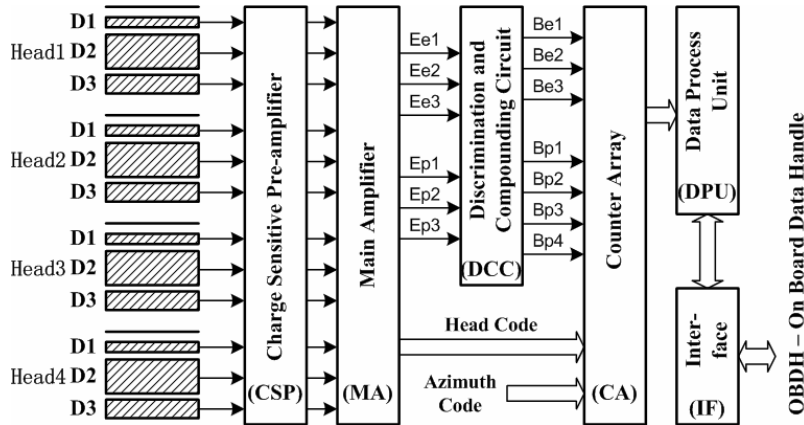


Fig. 4.17: Diagram of HECPE structure

HECPE is composed by the detection heads, Charge-Sensitive Pre-amplifier (CSP), Main Amplifier (MA), Discrimination and Compounding Circuit (DCC), Counter Array (CA), Data Process Unit (DPU), and Interface (IF), as shown in Figure 4.17.

Detection heads

The heads are as the particle telescopes. Each of them is composed of a collimator and three layers of the semiconductor detector, named as D1, D2, and D3 in Figure 4.17. They are in thickness of 100, 4000, and 1000 micron respectively. D1 and D3 are silicon PIN detectors. D2 is the stack of four 1000-micron detectors, or the silicon-lithium draft detector.

The combination of D1 and D2 is for the electron measurement. And the combination of D1, D2 and D3 is for the proton measurement. D1 is for distinguishing the electrons from protons of the incident particles. D2 is for energy measurement of electrons and low energy protons. D3 as a back detector is for energy measurement of high energy protons. In front of D1, there is an aluminum foil, thick of 30 micron, to shield the visible light.

If the energy of incident particles is much higher, their path ranges will be large than the thickness of detectors. Therefore, the energy deposition for these high energy particles depends on the incidence angle. The incidence angle is limited in 30° , half of the window angle.

Electron Circuit

CSP and MA in Figure 4.17 are signal collectors and amplifiers, they produce three signal groups. (Ee1, Ee2, E3) are from D1 and D2 for the electron measurement. (Ep1, Ep2, Ep3) are from D1, D2, and D3 for the proton measurement. The Head Code (HC) is a group of digital signal to mark which head the (Ee1, Ee2, E3) and (Ep1, Ep2, Ep3) belong to. DCC discriminates the signals to get the bin pulses by the energy of incident particles. The bin pulses are Bex (Be1, Be2, Be3) and Bpx (Bp1, Bp2, Bp3, Bp4). Bex are for the energy bins of electrons of $E > 0.5\text{MeV}$, $E > 1.0\text{MeV}$, and $E > 2.0\text{MeV}$ respectively. Bpx are for energy bins of protons of 5.0-10MeV, 10-20MeV, 20-40MeV, and 40-80MeV, respectively. Bex, Bpx, HC, and AC are sent to Counter Array (CA) to accumulate for flux measurements. The data are managed by DPU and sent to OBDH by Interface (IF).

Requirements to the platform of satellites

HECPE has follows requirements:

- Weight: about 4.5 kg
- Volume: main box about $220 \times 160 \times 165 \text{ mm}^3$
- Power +12 V, -12 V, and +5.20 V, total consumption 5.0 W
- Data rate for communication: 64 kByte per hour.
- Spin synchronous signal from OBDH.

- Data communication: Two RS422 ports to OBDH, one for data output, the other for control.
- Time code from OBDH.
- The heads need windows to the space. Each head needs 60° sight view.

4.2.8. Tri-Band beacon (TBB)

Each of the TBB measurement techniques requires high stability and phase coherence for the three transmitted frequencies. A block diagram of the scheme for frequency generation on the spacecraft is illustrated in Fig. 4.18. The three carrier frequencies (150.012, 400.032 and 1066.752 MHz) are derived from a stabilized crystal oscillator operating at 16.668 MHz. This “ovenized” oscillator has an inherent stability of 1 part in 10^{12} per 15-minute pass.

The L-band carrier near 1067 MHz is phase-modulated to send spacecraft data to ground telemetry receivers. The modulation scheme can be turned off when the L-band carrier is used for differential phase measurements.

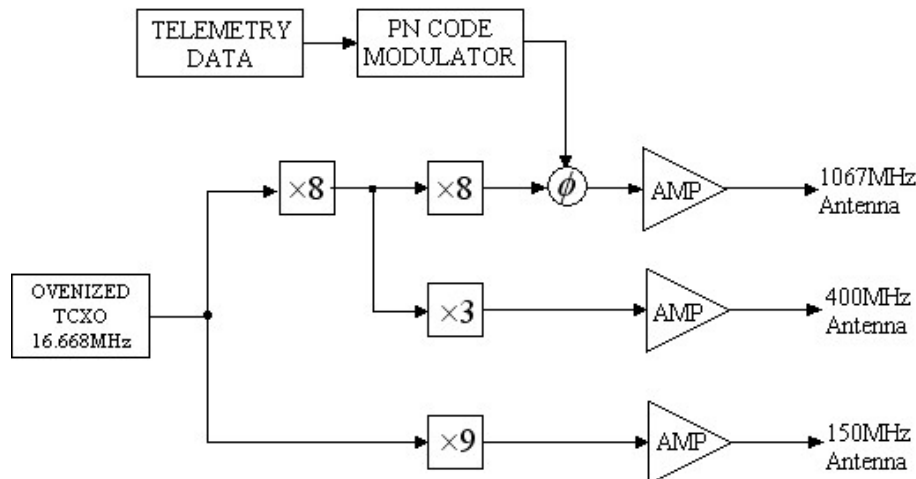


Fig. 4.18: A block diagram of the TBB

The antenna for the TBB was designed to preserve the relative phase among the three frequencies. The VHF and UHF signals are transmitted with crossed dipoles that are fed in quadrature to yield circular polarization. Each dipole has a 400 MHz trap to make it dual frequency. The third L-band frequency is radiated from a quadric-filar helix. All three antennae provide circular polarization below and horizontal polarization at the sides of the LEO satellite. The transmitter power of the TBB and the gain of the antenna must work in concert to provide at least -140 dBm (10^{-17} W) with a uniform phase front at the receiver. Table 4.21 lists the system requirements for satellite to ground links in both a quiescent and a turbulent ionosphere.

Table 4.21: Tri-Band Beacon Link Budget

*Values for a turbulent ionosphere

SUBJECT	150 MHz	400 MHz	1067 MHz
Transmitter Power (dBm)	27 (0.5 W)	30 (1.0 W)	33 (2.0 W)
Cable Loss (dB)	-1	-2	-3
TX Antenna Gain(dB)	2	2	2
Path Loss (dB)	-143.5	-152	-160.5
Scintillation (dB)	0 (-20) *	0 (-8) *	0 (-2) *
Polarization Loss (dB)	0	0	0
RX Antenna Gain (dB)	2	2.5	3.5
Signal At Receiver (dBm)	-113.5 (-133.5)*	-119.5 (-127.5) *	-122 (-124) *
Required Signal (dBm)	-130	-130	-130
Margin (dBm)	16.5 (-3.5) *	10.5 (2.5)	8 (6) *

5. KuaFu-B Orbits

The KuaFu-B orbits are based on the Canadian Ravens mission concept. The Ravens (and now KuaFu-B) mission scenario is based on the fact that it is possible to achieve continuous imaging of the auroral distribution in one hemisphere using two satellites. One way to accomplish this is with two spacecraft relatively phased on identical (coplanar) elliptical polar (90-degree inclination) orbits so that when one is at apogee, the other is at perigee. The relatively slow passage through apogee, and quick passage through perigee means that at all times at least one of the two spacecraft will be near apogee. We illustrate this concept in Figure 5.1, below. Of course, precession of the line of apsides causes the major axis of the orbital ellipse to precess, ultimately placing a time limit on how long such a satellite pair can maintain this continuous view of the auroral distribution. Calculations show, for example, that if the orbits have the same apogee and perigee as that of the NASA IMAGE spacecraft (8.2 and 1.3 R_E), and the imager fields of view are at least 20 degrees, then the satellites will have a continuous view of all points in the northern hemisphere above 50 degrees invariant magnetic latitude for roughly 1.6 years. This can be extended by raising the apogee, the perigee, or both. The former comes at the expense of spatial resolution, and the latter at the expense of ability to sustain high quality viewing throughout the orbit.

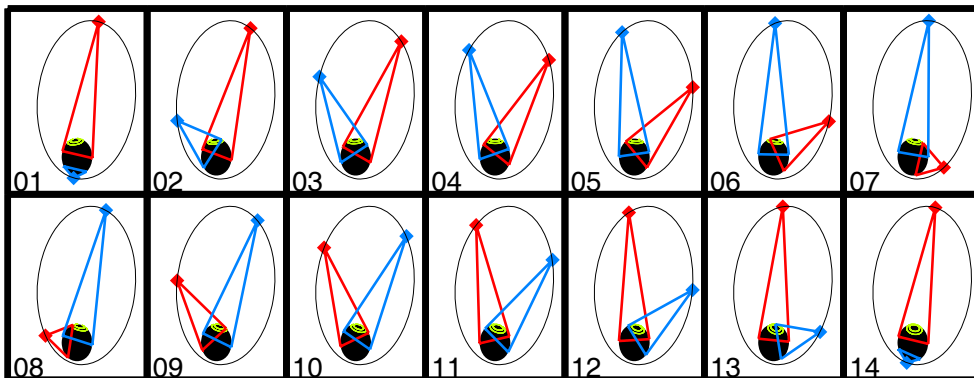


Fig. 5.1: 14 snapshots of two satellites relatively phased on identical polar orbits so that when one is at apogee the other is at perigee. At all times, the entire auroral oval (green) and polar cap are within view of at least one of the two satellites (red and blue cones).

The KuaFu-B satellite orbits will be at 90-degree inclination to maximize the time each satellite spends with an excellent view of the polar regions. The orbit must be significantly elliptical so that each satellite spends a large enough fraction of its orbital period near apogee. This is necessary for achieving the 24×7 continuous auroral coverage, but we point out the competing need that perigee should be high enough to facilitate conjugate imaging with the wide field of view (FOV) imager. For a given apogee and perigee that allows 24×7 viewing, the precession of the line of apsides then limits the duration of continuous viewing.

In order to explore possible orbits, we have developed a straightforward orbit simulation program. This program places two satellites on coplanar identical orbits. The satellites are co-rotating, 180 degrees out of phase so that when one is at apogee the other is at perigee. We are interested in how well the pair of satellites can see the northern hemisphere polar region. Given that one of our chief objectives is to study magnetic storms, we want to observe the global aurora even during active times. We have therefore assessed how well the satellites as a pair see the region above 50 degrees PACE invariant magnetic latitude.

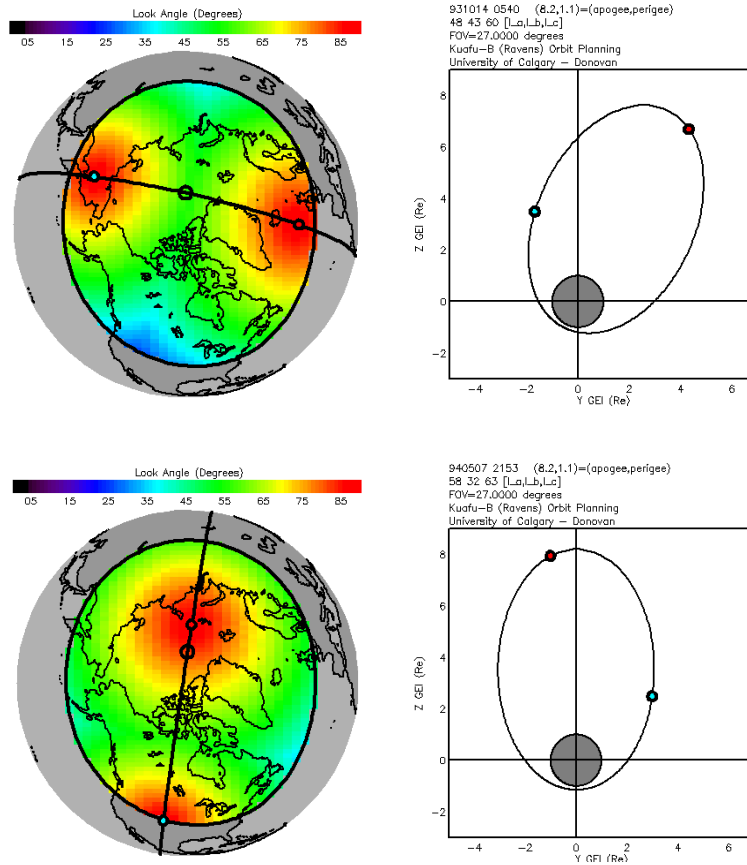


Fig. 5.2: Quality of viewing can be determined from an orbital simulation. The figure shows the “look angle” for two different times in a possible two-satellite mission. Important variables here are argument of perigee and time in specific orbit. For the specific case shown here there is roughly 6 months time between panels.

To make this assessment, we take “pixels” in the region of interest. For a given pixel, we determine which of the two satellites sees it better. Using that satellite, we determine the “look angle”, with 90 degrees being “straight down”. We then average this look angle over the entire region. An average measure of 0 means every pixel is at *best* seen obliquely (note that spatial resolution is best for a look angle of 90 and decreases away from 90. An average measure of 90 means that we are looking straight

down on every pixel, which, while being as good as it could be is only achievable with an infinite number of satellites. Our best estimate is that a number of 40 degrees is a “good image” (based on consideration of WIC images from IMAGE and spatial resolution considerations as discussed in the section on UVAMC below). We are therefore defining successful continuous global imaging to be a situation where the average look angle is greater than 40 degrees on an ongoing basis.

Our simulation then moves the satellites forward in time. We take 11 steps from an initial angle of line of apsides with the geographic pole until the line of apsides is the pole. At each of the 11 steps, we determine the “average look angle” (or “quality of viewing”) for four orbits (we rotate the Earth in step as well, which is necessary as the geomagnetic and geographic poles are not the same. This allows us to determine the length of time the quality of viewing is better than 40 degrees for a given apogee and perigee. The figure below illustrates one output from this program.

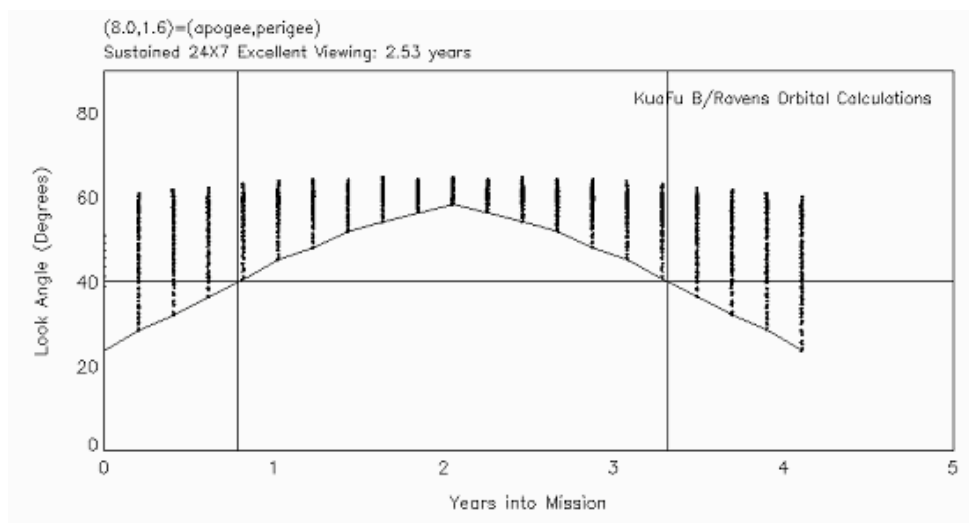


Fig. 5.3: Average look angle for different times in a simulated mission. In this instance the line of apsides reaches the pole in ~2 years. The average look angle is above 40 degrees for ~2.53 years.

Based on these calculations, and considerations of resolution, we have decided to argue for an orbit of $7 \times 1.8 R_E$ (radial from origin), with a 90 degree inclination, subject to radiation dosage issues. This gives us a roughly 13 hour orbit.

Given that conjugate auroral imaging with a wide FOV UV imager will be a technical objective for KuaFu-B, we double-checked that the orbits selected for KuaFu-B support high-quality conjugate imaging for a reasonable fraction of the orbital period. In order to carry out this test, we picked pixels in both the northern and southern hemisphere. For each pixel we carry out the above look angle calculation. For each southern hemisphere pixel there is a corresponding northern hemisphere pixel, where that correspondence is determined using the PACE invariant geomagnetic coordinates.

In other words, for this calculation, we are assuming that conjugacy is determined entirely by the internal field of the Earth, an assumption that is valid for simply estimating whether or not the orbits sustain conjugate viewing, especially at auroral latitudes.

The quality of conjugate viewing for that pair of pixels is determined by the poorest quality view of the two pixels. In other words, if one is seen well, and the other poorly, the conjugate viewing is poor. In figure 5.4, we show an example output of this calculation. The map at top left is the quality of view for the northern hemisphere only, while the map at bottom left is the conjugate quality of view (in this case excellent). The plot at the top right shows the direct (around 60) and conjugate (spikes at bottom) quality of view for four successive orbital periods. The red vertical line indicates the specific time that corresponds to the plots at left. The plot at bottom right shows the locations of B1 and B2 for that same time (in this case, excellent conjugate viewing is of course consistent with one satellite near apogee and the other near perigee). We also limited our attention to pixels above 60 degrees PACE latitude, with the idea that conjugate imaging will not be restricted to storm time, and in fact will likely be most valuable scientifically during non-storm time.

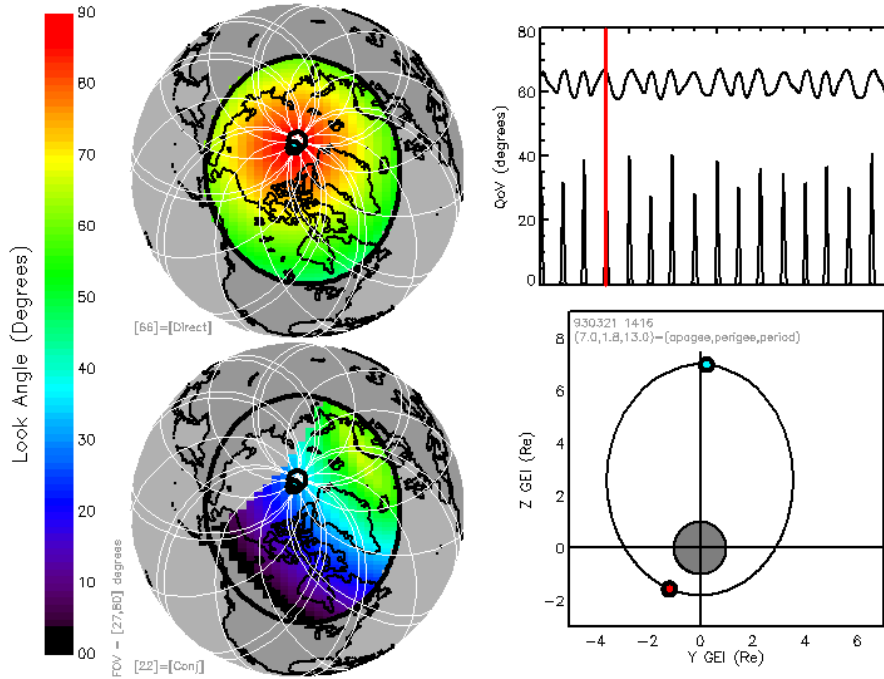


Fig. 5.4: Quality of direct and conjugate viewing for KuaFu-B using the proposed orbital parameters.

Good quality conjugate imaging for a 25-degree FOV UVAMC and a 40 degree FOV wide FOV imager operating the situation is like that shown above (proposed FOVs of the UV electron auroral instruments). The orbits are conjugate in geographic (GEI)

coordinates, however the auroral conjugacy is ordered by magnetic coordinates. The eccentricity of the dipole terms in the internal field shift the conjugate FOV relative to the direct FOV. Regardless, our calculations show that we can expect reasonable conjugate viewing (comparable to or better than that shown above), for roughly 9% of the orbit. Another way of looking at this is that we will have good quality conjugate imaging for around 35 minutes twice per orbital period.

We point out that investigation of a Molniya-type orbit demonstrated that conjugate imaging could not be supported if that type of orbit was adopted.

6. Spacecraft initial design

6.1. KuaFu-A spacecraft

6.1.1. KuaFu-A spacecraft design requirements and constraints

6.1.1.1. Mission Analysis

For KuaFu-A Mission, the key points are the following:

- How to get to the L1 point? Since the L1 point is of about 150,000,000 km away from the Earth, it is an arduous challenge for any spacecraft to reach this point. Thus, Transfer orbit and flight strategy is very important for the KuaFu-A spacecraft.
- How to stay around the L1 point? Since the L1 point is an unstable libration point, the spacecraft cannot be held near this point for a long time without any active control maneuvers. Achieving and maintaining the spacecraft orbit at L1 is of crucial importance for the mission.
- How to carry out communication between the KuaFu-A spacecraft and the Earth? Since the operating location of the KuaFu-A spacecraft is in deep space (about 1.5 million km away from Earth) the implementation of an appropriate communication link is a major challenge for this mission.
- How to achieve a sufficiently accurate spacecraft control? Some scientific instruments on the KuaFu-A spacecraft require the satellite platform to provide very highly accurate control performance.

6.1.1.2. Payload Requirement Analysis

Payload total requirements:

- Total mass: ~100 kg;
- Total power: ~120 W;
- Total data rate: ~210 kbps.

Note that the resources (in particular mass) could be reduced (ref. Table 1.1).

Also:

- Instrument accommodation, e.g., view direction, size;
- Thermal control requirements.

6.1.2. KuaFu-A spacecraft baseline design

The design of the KuaFu-A spacecraft is based on a modular concept with two main elements: the Payload Module (PLM) and the Service Module (SVM). This configuration provides easy mounting and accessibility to the payload instruments, while satisfying all instrument functional requirements, particularly with respect to viewing directions, fields-of-view, cleanliness, and pointing accuracy and stability.

The PLM consists of all the scientific instruments which are used to observe the solar activities. At present, the considered instruments include EDI, CDI, RBI, SWIP and SEPS. Of course, the design can be adjusted if the payload is changed.

The SVM is composed of 8 subsystems:

- Structure Subsystem (STS);
- Thermal Control System (TCS);
- Attitude and Orbit Control subsystem (AOCS);
- Data Management subsystem (DMS);
- TT&C Subsystem (TT&CS);
- Data Transmission Subsystem (DTS)
- Power Supply Subsystem (PSS).

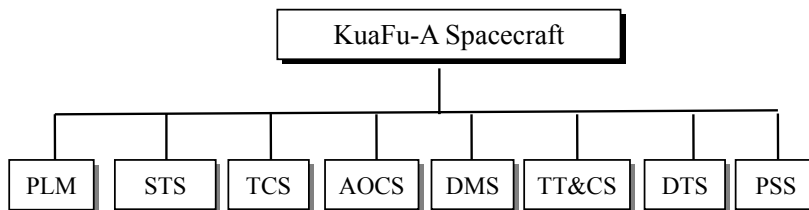


Fig. 6.1: The overall system structure of the KuaFu-A

Fig. 6.1 shows the overall system structure of the KuaFu-A spacecraft.

For the KuaFu-A design, the main ideas are as follows:

- A passive thermal control system is mainly adopted, supported by an active thermal control system, if needed.
- DMS is responsible for the comprehensive onboard information processing and performing highly efficient and reliable management and control.

- An attitude computer controls momentum wheels in order to maintain normal Sun pointing and perform attitude maneuver. A hydrazine system is used to adjust attitude and orbit.
- S-band TT&C is adopted, and for data transmission X-band is used.
- GaAs/Ge solar arrays and CdNi batteries (re-assessment needed) are applied to provide the required electrical power to all on-board equipments.

6.1.2.1. Coordinate system Definitions

The KuaFu-A spacecraft uses a fundamental reference frame: the absolute reference frame (X_a, Y_a, Z_a). It is defined as follows:

- Its origin coincides with the spacecraft mass centre;
- Its X-axis is along the spacecraft-Sun line and oriented towards the centre of the Sun;
- Its Z-axis is vertical to the ecliptic plane; **(We prefer it to be pointing to the solar northern pole, as is done on SOHO).**
- Its Y-axis completes the right-handed orthogonal reference frame.

6.1.2.2. Preliminary Configuration

The conceptual configuration of the KuaFu-A spacecraft is shown in Fig. A6.2 and Fig. 6.3. Some points to be considered:

- Mass distribution:
 - Location of center of mass
 - Structure and mass symmetry
 - Dynamics characteristic
- FOV requirements:
 - Instruments: EUV (or FUV), CDI, SWIPS
 - Attitude sensors: DSS (digital solar sensor), ASS (analog solar sensor) and SS (star sensor)
 - Antennas: TT&C antennas(6, 4 omni directional antennas and 2 medium gain antennas) and data transmission antenna(1, 0.8m parabolic antenna)
- Instrument and equipment assembly requirements:
 - Field of view pointing

- Attitude and orbit control equipment requirements
- Deployable equipment assembly
- Special thermal control requirements
- Cleanliness requirements

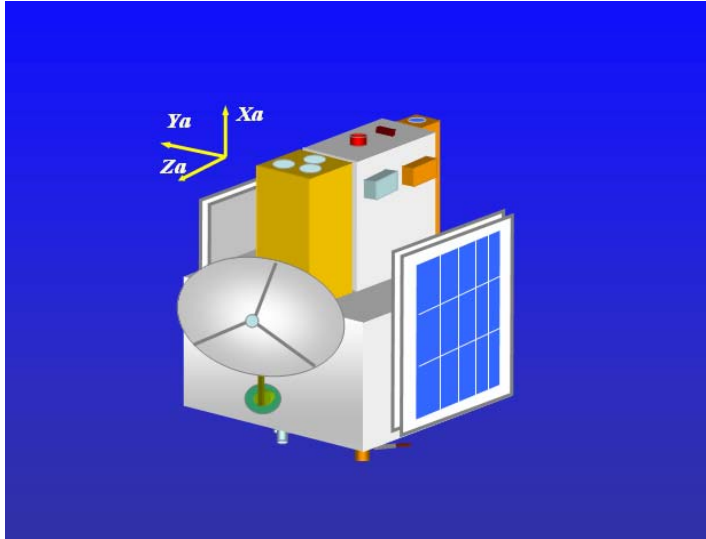


Fig. 6.2: Initial configuration (a) of the KuaFu-A spacecraft (before deployment)

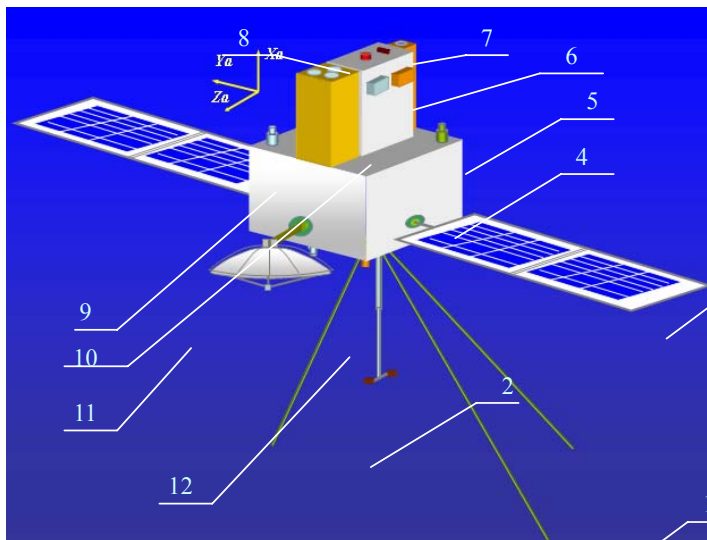


Fig. 6.3: Mission configuration (b) of the KuaFu-A spacecraft (after deployment)

Notes: 1 RBI (deployed); 2 SWIP (PID mounted on the front); 3 solar arrays; 4 SVM cabin; 5 TT&C omni directional antenna; 6 SEPS; 7 CDI ; 8 DSS ; 9 EDI; 10 PLM cabin; 11 Data transmission antenna; 12 Thruster.

6.1.2.3. Preliminary Orbit Consideration

Phase Description and Attitude requirement

Table 6.1: Phase Description

Phase	Attitude requirement	
	Direct transfer	Phasing loops
Launch phase	n/a	n/a
Transfer phase	+X pointing to the Sun, +Z vertical to the Ecliptic Plane	+X pointing to the Sun, +Z vertical to the Ecliptic Plane
Operation phase	+X pointing to the Sun, +Z (see remark above!) vertical to the Ecliptic Plane	+X pointing to the Sun, +Z vertical to the Ecliptic Plane

Transfer

Under investigation yet, either direct transfer or phasing loops would be taken.

6.1.3. KuaFu-A spacecraft propulsion and hydrazine budget

ΔV (Hydrazine) Budget

Determining the ΔV budget based on the following assumption:

- The total mass of the spacecraft is around 700 kg
- The magnitude of A_y of the operation halo orbit is about 670,000 km

The correction plan and ΔV budget is shown in the following table.

Table 6.2: ΔV budget

	Direct Transfer	Phasing Loops
Insertion Inaccuracy Correction	50 m/s	20 m/s
Phasing Loops	n/a	50 m/s
Final Perigee Correction	n/a	15 m/s
Lunar Encounter Correction	n/a	5 m/s
Midcourse Correction	5 m/s	5 m/s
Halo Orbit Insertion	80 m/s	10 m/s
Station Keeping	4 m/s/y	4 m/s/y
Emergency	100 m/s	100 m/s

Total (5 years)	265m/s	225 m/s
-----------------	--------	---------

Therefore, 100 kg hydrazine, which will give us more than 300m/s, will meet the mission budget.

6.1.4. KuaFu-A spacecraft major parameters and specifications

The major performance parameters of the KuaFu-A spacecraft are summarized in Table 6.3. Also, the mass budget and the power budget are shown in Table 6.4 and Table 6.5.

Table 6.3: Major Parameters of the KuaFu-A spacecraft

Size	1350 mm×1440 mm×1400 mm (Before deployed) 5500 mm×5200 mm×3300 mm (After deployed)
Mass	Total: 700 kg Payload: 100 kg Platform: 500 kg (100 kg hydrazine included) Margin: 100 kg
Power	Total: 290 W Payload: 120 W Platform: 150 W Margin: 20 W
Attitude control	Attitude pointing error: < 45° (X axis) Attitude stability: 3°/30 s (X axis)
TT&C	Band: S band Data rate: 1 kbps
Data transmission	Band: X band Data rate: 210 kbps

Table 6.4: Mass Budget of the KuaFu-A spacecraft

Payload	100 kg
STS	130 kg
AOCS	Equipment: 150 kg Hydrazine: 100 kg
TT&CS	20 kg
DTS	20 kg
DMS	30 kg
PSS	50 kg
Margin	100 kg
Total	700 kg

Table 6.5: Power Budget of the KuaFu-A spacecraft

Payload	120 W
AOCS	80 W
TT&CS	20 W
DTS	25 W
DMS	20 W
Margin	20 W
Total	285 W

6.2. KuaFu-B spacecraft

6.2.1. KuaFu-B spacecraft design requirements and constraints

Two satellites, KuaFu-B-1 and KuaFu-B-2, are put forward to meet the KuaFu-B mission requirements. The satellites pair, with the same science payloads, will run the same operational orbit, $6 \times 0.8 R_E$ (altitude) and 90 degree inclination, one at the perigee while the other at the apogee.

The KuaFu-B satellite will be re-designed based on the full experience from Double Star Project.

The KuaFu-B pair could be double launched into parking orbit in 2012 by one CZ-3B rocket and then do a maneuver into operational orbit by themselves. Or they could be single launched into the target orbit directly by CZ-2C/SM, which carried successfully the DSP satellites.

Up to now, 8 science payloads, UVAMC, FUVSI, WFAI, NAIK, FGM, IES/IPS, HECPE and TBB, would be carried by KuaFu-B pair to meet the KuaFu-B mission aims.

The original KuaFu-B mission had such unique requirements that must be met:

- 1) The spin rate is 0.5~6 rpm
- 2) The spin axial perpendicular to the orbit plane
- 3) Continuously and seamlessly observe the North Pole region with KuaFu-B pair
- 4) The magnetic field at the outboard sensor should be below than 0.5 nT.

KuaFu-B could be either launched by a “double launch” or a “single launch”.

● Double Launch

The KuaFu-B pair could be launched into polar orbit together by CZ-3B rocket, which is designed by CALT. The pair will be accommodated into the fairing of rocket as shown in figure 6.4

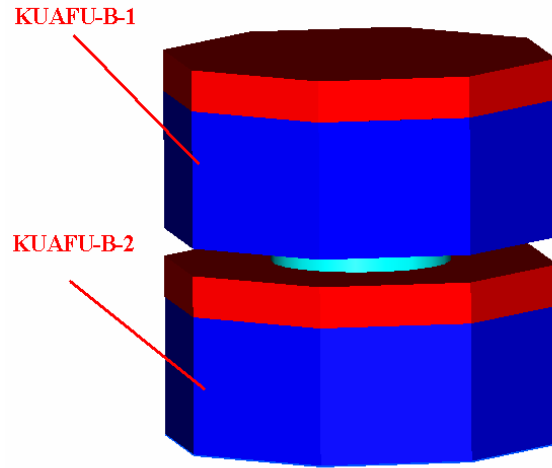


Fig 6.4: The configuration of KuaFu-B pair in the fairing

At first, the pair will be launched into a smaller elliptic parking orbit with $0.8 R_E$ perigee altitude with 90-degree inclination. The one will fulfill the maneuver first to the operational orbit at the perigee. Then two spacecraft will not run in the same orbit until the other one will be kicked as soon as they have 180-degree phase difference.

- **Single launch**

The satellite could be launched by CZ-2C/SM rocket one by one.

6.2.2. KuaFu-B spacecraft baseline design

Structure Subsystem

The conceptual deployed KuaFu-B satellite is shown in Fig.6.5. The KuaFu-B spacecraft, 2900 millimeters in diameter and 1300 millimeters in height, is spin-stabilized. The total mass of the KuaFu-B is about 400 kg with propellant.

Viewed from either end, KuaFu-B has the form of a regular octagon. The main body of the spacecraft is a cylinder that consists of ten honeycomb panels. 8 side panels constitute the cylinder and the forward panel and aft panel are fixed to them.

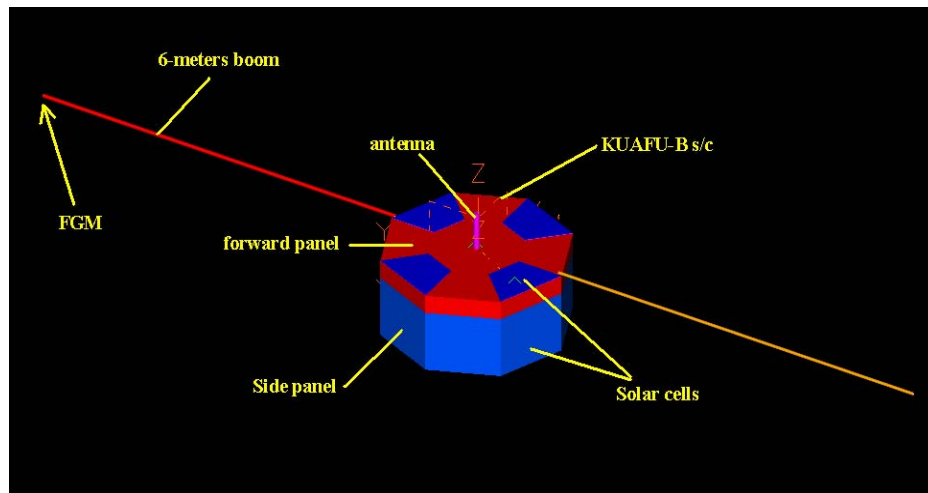


Fig. 6.5: The configuration of KuaFu-B spacecraft with deployed booms

The Solar arrays are attached to the KuaFu-B's 8 side panels, and the 2 end panels provide sufficient power to the science instruments and the s/c subsystems. The total power provided by the solar cells is about 250 W. When in eclipse, electrical power will be provided by a battery.

Mechanism Sub-system

Two rigid booms are installed on the front side of the KuaFu-B spacecraft. The length of the boom after being deployed is 6 meters and the 2 booms are stowed for launch. At the end of one boom, FGM is mounted in order to meet the rigorous requirement of magnetic cleanliness and avoid the interference from the spacecraft.

As shown in Figure 6.5, it would be better to mount two symmetric booms on the spacecraft. So, there is another opportunity for any boom-mounted unit having a mass less than 400g.

6.2.3. KuaFu-B spacecraft major parameters and specifications

Key Parameters of KuaFu-B spacecraft:

Spin rate:	6 rpm
Spacecraft Diameter:	2900 mm
Spacecraft Height:	1300 mm
Mass:	400 kg

Mass Allocated to Science Payloads:	43 kg
Solar Array Power:	250 W
Power Allocated to Science Payloads:	50 W
Life time:	>3 year

Orbit Parameters:

Orbit inclination:	90 degree
Apogee altitude:	6 R _E
Perigee altitude:	0.8 R _E
Eccentricity:	0.48
Period:	17.67 hours

Mass Allocation of KuaFu-B Spacecraft:

Mechanical Sub-system (Deployable Booms):	140 kg (35 kg)
Attitude Determination & Control Sub-system:	40 kg
On-board Data Handling Sub-system:	55 kg
Communications	12 kg
Electrical Power Sub-system:	70 kg
Thermal Sub-system:	20 kg
Science Instruments:	60 kg
Total (margin):	400 kg (20 kg)

Power Allocation:

Sub-system		Power (W)
KuaFu-B s/c	Attitude Determination & Control Sub-system	17
	Communications	21
	On-board Data Handling Sub-system	25
	Thermal Sub-system	18
	Electrical Power Sub-system	12
Science Payload	Science instruments	50
	Data Handling	35
	Transmission	80
Total (W)		250

KuaFu-B Spacecraft Description:

Structure:	Octagon cylinder Diameter: 2900 mm Height: 1300 mm
Mechanisms:	Two deployable booms, each 6000 mm
Attitude:	Spin-stabilized
Communications:	S-Band Downlink: 1Mbps when range smaller than 8000 km. Uplink: 1000 bps
Data Storage:	2 Gbit (TBD)
Power:	Body-Mounted Solar Cells & Battery

List of Acronyms

ACE:	Advanced Composition Explorer
AIA:	Solar Atmospheric Imaging Assembly
AMIE:	Assimilative Mapping of Ionospheric Electrodynamics
AMISR:	The Advanced Modular Incoherent Scatter Radar
AOCS:	Attitude and Orbit Control subsystem
AR:	Active Region
ASP:	Auroral Scanning Photometer
ASS:	Analog Solar Sensor
BATS-R-US:	Block-Adaptive Tree Solar-wind Roe Upwind Scheme
BFRB:	Bi-Frequency Radio Beacon
CCD:	Charge Coupled Device
CDI:	Coronal Dynamics Imager
CGSM:	Canadian GeoSpace Monitoring
CIR:	Corotating Interaction Region
CIT:	Computerized Ionospheric Tomography
CME:	Coronal Mass Ejection
CNES:	Centre National d'Etudes Spatiales
COR:	Coronagraph
CPS:	Central Plasma Sheet
DASI:	Distributed arrays of small instruments
DE:	Dynamics Explorer
DIB:	DPU Interface Board
DMS:	Data Management subsystem
DPU:	Data Processing Unit
DSP:	Digital Signal Processor
DSS:	Digital Solar Sensor
DTS:	Data Transmission Subsystem

EDI: EUV/FUV Disk Imager

EISCAT: European Incoherent Scatter Radar

EIT: EUV Imaging Telescope

EM: electromagnetic

EMC: Electro-Magnetic Cleanliness

ENA: Energetic Neutral Atom

EPIC: Energetic Particle and Ion Composition

ePOP: enhanced Polar Outflow Probe

ESA: European Space Agency

EUV: Extreme Ultraviolet

EXT: Extension Board

FAST: The Fast Auroral Snapshot

FdM: Front Door Mechanism

FGM: Fluxgate Magnetometer

FOV: Field of View

FUV: Far Ultraviolet

UVAMC: Far Ultraviolet Aurora Monitoring Camera

FUVSI: Far Ultraviolet Spectro-Imager

FWHM: Full Width at Half Maximum

GCR: Galactic Cosmic Ray

HECPE: High Energy Charged Particle Experiment

HEPT: High Energy Particle Telescope

HFR: High Frequency Receiver

HILAT: High Latitude Research Satellite

HXGS : Hard X-ray and Gamma-ray Spectrometer

ICESTAR Interhemispheric Conjugacy Effects in Solar-Terrestrial and Aeronomy Research

IES: Imaging Electron Spectrometer

ILWS: International Living With a Star

IMAGE: Imager for Magnetopause-to-Aurora Global Exploration

IMF: Interplanetary Magnetic Field

IMP: Interplanetary Monitoring Platform

IMPACT: In-situ Measurements of Particles and CME Transients (on STEREO)

IOCS: Internal Occultor Centering System

IPS: Imaging Proton Spectrometer

IR: Infrared

ISEE: International Sun-Earth Explorers

ISIS: International Satellites for Ionospheric Studies

IT: Ionosphere-Thermosphere

ITSP: International Solar-Terrestrial Physics

JAXA: Japan Aerospace Exploration Agency

KH: Kelvin-Helmholtz

Ku-Cor: KuaFu-A Coronagraph

LASCO: Large Angle and Spectrometric Coronagraph

LBH: Lyman Birge Hopfield band

LBH-l: LBH long

LBH-s: LBH short

LEO: Low Earth Orbit

LFR: Low Frequency Receiver

MAG: Magnetometer

MCB: Mechanism Controller Board

MHD: magnetohydrodynamics

MI Coupling: Magnetosphere-Ionosphere Coupling

MMB: Mass Memory Board

MXUVI: Multiple XUV Imager

NAIK: Neutral Atom Imager on KuaFu

NASA: National Aeronautics and Space Administration

NOAA: National Oceanic and Atmospheric Administration

NPOES: National Polar Orbit Environment Satellite

NSFC: National Natural Science Foundation of China

PBI: poleward boundary intensifications

PCM: Power Converter Module

PID: Plasma Ion Detector

PIE: Plasma Electron Instrument

PLM: Payload Module

PSBL: Plasma Sheet Boundary Layer

PSS: Power Supply Subsystem

PZT: Piezoelectric Transducer

RB: Radiation Belt

RBI: Radio Burst Instrument

RBSP: Radiation Belt Storm Probes

RM: Refocusing Mechanism

ROMAP: Rosetta Lander Magnetometer and Plasma Monitor

S/C: Spacecraft

SDO: Solar Dynamics Observatory

SECCHI: Sun Earth Connection Coronal and Heliospheric Investigation

SEL: Single Event Latchup

SEP: Solar Energetic Particle

SEPS: Solar Energetic Particle Sensor

SEU: Single Event Upset

SOHO: Solar and Heliospheric Observatory

SS: Star Sensor

STEREO: Solar-Terrestrial Relations Observatory

STS: Structure Subsystem

SuperDARN: Super Dual Auroral Radar Network

SVM: Service Module

SWAP: Sun Watcher using APs detectors and image processing

SWASE: Solar Wind and Aurora Storm Explorer

SWEA: Solar Wind Electron Analyzer

SWIP : Solar Wind Instrument Package

SWISE: Solar Wind and Interplanetary Storm Explorer (now SWASE)

SwRI: Southwest Research Institute

TBB: Tri-Band Beacon

TBC : To Be Confirmed

TBD: To Be Decided

TCS: Thermal Control System

TEC: Total Electron Content

THEMIS: Thermal Emission Imaging System

TRACE: Transition Region And Coronal Explorer

TT&CS: TT&C Subsystem

UARS: Upper Atmospheric Research Satellite

UHF: Ultra High Frequency

ULF: Ultra Low Frequency

UVCS: Ultraviolet Coronagraph Spectrometer (on SOHO)

UVI : Ultraviolet Auroral Imager (on Polar)

VHF: Very High Frequency

VIS: Visible Imaging System (on Polar)

VUV: Vacuum Ultraviolet

WFAI: Wide Field Aurora Imager